ON THE STABILITY OF MAGNETOHYDRODYNAMIC SHEAR FLOWS: CHARACTERIZATION OF CRITICAL PRESSURE-VELOCITY-MAGNETIC-FIELD INTERACTIONS

A Dissertation

by

DIVYA SRI PRATURI

Submitted to the Office of Graduate and Professional Studies of
Texas A&M University
in partial fulfillment of the requirements for the degree of

DOCTOR OF PHILOSOPHY

Chair of Committee,	Sharath S. Girimaji
Committee Members,	Diego Donzis
	Adonios Karpetis
	Jean-Luc Guermond
Head of Department,	Rodney Bowersox

December 2018

Major Subject: Aerospace Engineering

ABSTRACT

Plasma shear flows are abundant in nature and frequently encountered in engineering applications. The stability characteristics of plasma shear flows are of much fundamental interest. Shear flows are susceptible to various algebraic and modal instabilities, i.e., velocity perturbations grow as a polynomial or an exponential function of time. It is well known in literature that background magnetic field applied along the flow direction and compressibility have a stabilizing influence on these shear instabilities. In this dissertation, a systematic investigation of the stabilization mechanisms is performed. This dissertation consists of three studies, each addressing a different type of free shear layer: *Study 1* - homogeneously sheared flows in the incompressible regime; *Study 2* - inhomogeneously sheared mixing layers in the incompressible regime; *Study 3* - inhomogeneously sheared planar jets in the compressible regime. The common theme of all the studies investigate the nature of pressure-velocity-magnetic-field interactions that influence stabilizing mechanisms.

For the case of homogeneous shear investigated in the first study, velocity perturbations in the absence of the magnetic field are susceptible to algebraic instability, i.e., kinetic energy contained in the perturbations (k) grows as, $k \sim \mathcal{O}(t^n)$. The stabilizing influence of magnetic field strength and perturbation orientation (β) on the instability is characterized using linear analysis and direct numerical simulations. Linear analysis indicates that the perturbation growth is dependent on the parameter, $R_A \equiv V_A\kappa/S$, where, V_A, κ and S are the Alfvén wave speed, initial wavenumber and mean flow shear, respectively. Analytical solutions for various perturbation energies at extreme R_A regimes – $R_A \gg 1$ and $R_A \ll 1$ – are derived and compared to numerical simulations. The behavior of perturbations at different R_A regimes and β values is also explicated using numerical simulations.

In the second study, a tangent hyperbolic profile is chosen for the mean velocity field. Owing to the presence of an inflection point in the profile, the flow field is subjected to Kelvin-Helmholtz (KH) instability leading to exponential growth of perturbations, i.e., $k \sim \mathcal{O}(e^t)$. In the absence of any magnetic field (hydrodynamic limit), the precursor vortices form and roll up into a primary

vortex. The primary vortex further entrains fluid leading to the onset of nonlinear asymptotic stage and formation of secondary vortex bands. We investigate the linear and nonlinear effects of magnetic field on this three-stage evolution of KH instability. Flow field features such as circulation, gauge pressure and perturbation energies are utilized to delineate the parameter space into strong, weak and intermediate magnetic-field stabilization regimes. The mechanisms of magnetic field stabilization in each of the three regimes is investigated using direct numerical simulations.

In the third study, the evolution of pressure-, kinetic- and magnetic-perturbation energies for the case of compressible magnetohydrodynamic (MHD) planar jets is investigated. A streamwise background magnetic field is again applied. The change in the nature of interactions between velocity and magnetic fields due to compressibility is established using linear analysis. Numerical simulations of single mode and random, isotropic initial perturbations are performed to examine these new agencies of exchange and their subsequent effect on the overall stability of the flow field.

The findings of this dissertation are expected to further our understanding of various compressible and magnetic field mechanisms and their roles in perturbation evolution. This will aid in the development of closure models for MHD shear flows which could be used for designing efficient plasma propulsion engines and flow control devices.

DEDICATION

To my mother, father and little brother.

ACKNOWLEDGMENTS

Firstly, I would like to thank my advisor, Dr. Sharath Girimaji, for believing in me and taking me on as a graduate student in his lab. I am extremely grateful for his guidance and financial support throughout, and the opportunities he provided that enabled my professional growth. I also would like to thank my committee members, Drs. Diego Donzis, Adonios Karpetis and Jean-Luc Guermond for their help and support. The graduate classes I took under them have helped me develop the tools that made this research possible. I am also immensely thankful to Dr. K. R. Sreenivasan for providing me with HIAS fellowship and for always taking out time to meet with me during his visits to A&M.

I would like to thank my labmates Ankita, Rishita, Steven, Mona, Chetna, Bajrang, Massey, Pedram, Filipe and Zach for making my time at grad school fun and memorable. A special thank you to Ankita and Sualeh for being my go-to people who have always had my back.

None of this would have been possible without the caring love and support of my family. Words can't express my gratitude towards my parents, Sarma and Neeraja, for being supportive of my aspirations in life. They have always prioritized my needs over theirs and sacrificed so much in order to provide me with a better life. I would like to thank my brother, Deepu, for being the caring, sensitive and selfless little brother that he is. Lastly, I would like to thank my husband/best-friend, Krishna, for always being there for me. I feel fortunate to have found a person who brings out the best in me and is extremely supportive of my career choices, even if it meant spending six years apart.

CONTRIBUTORS AND FUNDING SOURCES

Contributors

This work was supported by a dissertation committee consisting of Professors Sharath Girimaji, Diego Donzis and Adonios Karpetis of the Department of Aerospace Engineering and Professor Jean-Luc Guermond of the Department of Mathematics.

All work conducted for the dissertation was completed by the student independently.

Funding Sources

Graduate study was supported by the Teaching assistantships from Aerospace engineering at Texas A&M University, Research assistanships with funds from Airforce, HEEP fellowship from Hagler Institute for advanced studies and Amelia Earhart fellowship.

The numerical simulations in this dissertation were performed making use of high performance computing resources at Texas A&M University and UT Austin.

TABLE OF CONTENTS

Page

LIST OF FIGURES

FIGURE Page

LIST OF TABLES

TABLE Page

1. INTRODUCTION

1.1 Motivation

Plasma shear flows are abundant in nature and engineering applications as plasmas constitute 99% of the baryonic matter in the universe (Chen, 1994). The inherent electric and magnetic fields present in plasma shear flows make their behavior markedly different as opposed to a hydrodynamic shear flow. Such a change in behavior is evident in the collimated evolution of astrophysical jets over thousands of light years, for example plasma jet emanating from the active galaxy, Messier 87, remains collimated for 4900 light years or 1.5 kilo-parsec (Doeleman *et al.*, 2012). As these jets propagate at hypersonic/relativistic speeds, compressibility also alters their evolution, in addition to modifications by electric and magnetic fields. The effects of compressibility and magnetic fields resulting in collimation of these jets/outflows has been a subject of intense research in the astrophysics community (Blandford & Payne, 1982).

Understanding the processes that govern plasma shear flows is important as they have applications in other naturally-occurring and engineering flows. For example, plasma shear flows play a crucial role in the generation mechanism of a solar cycle (Zaqarashvili, 1997), entry of solar wind into Earth's magnetosphere (Nykyri & Otto, 2001), magnetorotational dynamo action (Herault *et al.*, 2011), neutron star mergers (Price & Rosswog, 2006; Obergaulinger *et al.*, 2010) and magnetic reconnection (Faganello *et al.*, 2008; Belle-Hamer *et al.*, 1994), to name a few. In aerospace engineering, shear flows and large scale instabilities arising out of separated flow over an aircraft are controlled by means of magnetic fields and plasma actuators (Roth *et al.*, 1998; Shatrov & Gerbeth, 2007; Thomas *et al.*, 2008; Corke *et al.*, 2010). Such control strategies could result in reduced noise and drag caused by the non-aerodynamic components in the airframe. In space propulsion applications, plasma jets generate thrust via Lorentz force as in a magnetoplasmadynamic (MPD) thruster (Mikellides *et al.*, 2000) or via a magnetic nozzle as in a variable specific impulse magnetoplasma rocket (VASIMR) (Diaz, 2000). The motivation for this dissertation stems from the need to

understand the mechanisms of stabilization of compressibility and magnetic field on plasma shear flows in order to develop physics-based closure models that could be used in complex engineering flows.

1.2 Background

While investigating the evolution of plasma jets/shear flows, many studies in literature adopt a single fluid approximation, known as magnetohydrodynamics (MHD). A single fluid approximation can be justified despite the presence of multiply charged ions and electrons for a quasi-neutral, fully ionized plasma (Kulsrud, 2005; Goossens, 2012). As we also adopt MHD paradigm in this dissertation, we present a background of MHD shear flow literature in which the effects of compressibility and magnetic fields are studied.

Stability of hydrodynamic shear flows have been studied for over a century. The linear stability works of Kelvin and Helmholtz underlined the instability of an incompressible hydrodynamic vortex sheet, i.e., a discontinuous mixing layer (Helmholtz, 1868; Thomson, 1871). The stability of vortex sheet in the context of MHD with magnetic field applied was first investigated by Chandrasekhar (1961). He identified the magnetic field applied along the flow, i.e., along the streamwise direction, to be stabilizing. Other orientations of magnetic field do not have any effect on the instability of the vortex sheet. This stabilizing action of magnetic field is also seen in the case of continuous mixing layers, for example, tangent hyperbolic mixing layers (Ong & Roderick, 1972). Compressibility has also been shown to have a similar stabilizing effect on the growth rate of a hydrodynamic mixing layer (Blumen *et al.*, 1975). Where as in a MHD vortex sheet, compressibility can be stabilizing or destabilizing depending upon the ratio of velocity jump and magneto-acoustic speeds (Sen, 1964).

The nonlinear stability of incompressible and compressible MHD shear flows has also been addressed in numerous works by means of numerical simulations (Malagoli *et al.*, 1996; Frank *et al.*, 1996; Baty & Keppens, 2006; Palotti *et al.*, 2008). These studies identified the nonlinear stabilizing action of magnetic field at late times, even for field strengths where linear stabilization can't be seen. The nonlinear stabilization at late times is due to the onset of 'resistive' instability.

Since understanding the mechanisms of collimation/ astrophysical phenomena motivated many of these studies, the effects of both compressibility and magnetic field have been incorporated. Such an approach renders the isolation of individual processes pertaining to compressibility and magnetic field difficult. Our goal is to examine the effects of compressibility and magnetic fields individually and then in combination. This allows for identification of specific mechanisms leading to possible closure modeling.

1.3 Thesis research

Objective Statement: **(i) To advance the fundamental understanding of flow mechanisms in compressible MHD shear flows by examining the effects of magnetic field and compressibility in isolation and in combination. (ii) To understand the stability characteristics of MHD shear flows at various speed regimes.**

1.3.1 Research tasks

To achieve the above objectives, we examine the evolution of incompressible and compressible shear MHD flows using linear analysis and numerical simulations. The stability of any shear flow is dictated by the interactions between pressure and velocity fields. Such interactions are profoundly modified by compressibility and background magnetic fields. Therefore, to determine the stability of an MHD shear flow, it is imperative to evaluate and characterize pressure-velocity-magnetic field interactions. Investigation of these interactions for shear flows at various degrees of compressibility and magnetic field strength forms the central theme of this work.

The flowchart in figure 1.1 depicts the approach that needs to be followed to understand the stability of MHD shear flows. The tasks already performed in literature are indicated in light gray boxes, i.e., pressure-velocity interactions in compressible shear flows. A comprehensive investigation of the effect of compressibility on turbulent shear flows has been preformed previously in the research group (Kumar *et al.*, 2014; Karimi & Girimaji, 2016; Xie *et al.*, 2017). Dark gray boxes indicate the novel tasks performed in this dissertation. Pressure-velocity-magnetic field interactions in the incompressible limit are evaluated first. This results in the isolation of stabilization

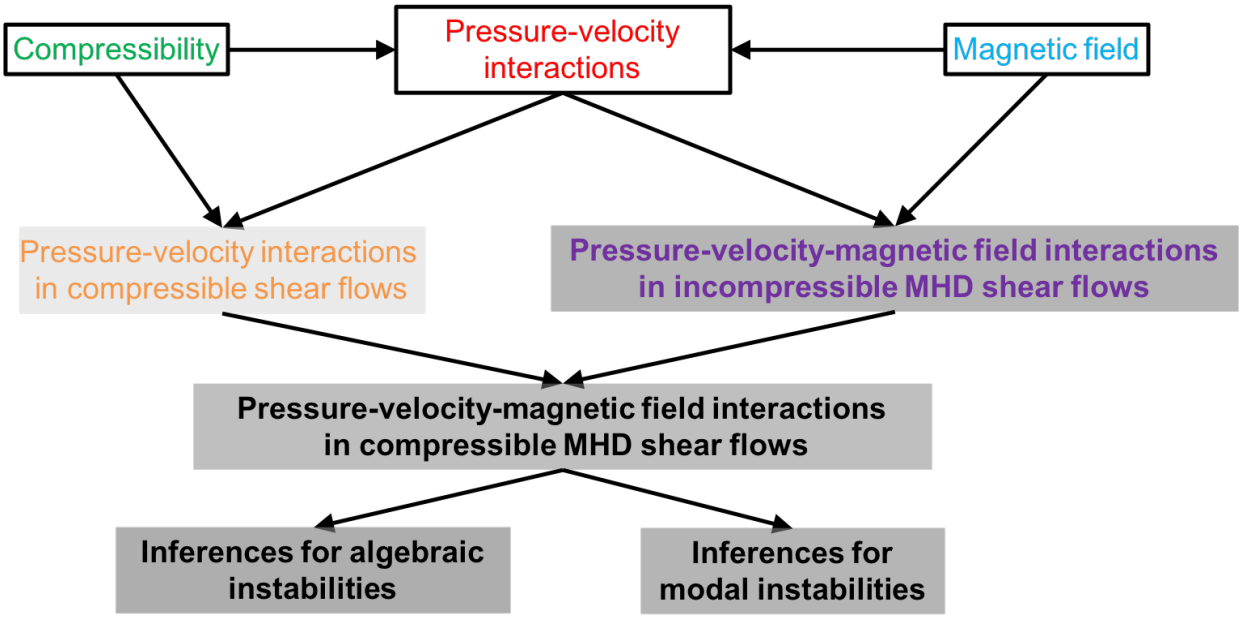

Figure 1.1: Flowchart identifying the specific objectives of this study. The ones examined in detail in literature are indicated in light gray boxes, where as, the novel studies of this dissertation are in dark gray boxes.

processes pertaining to magnetic field. Then, the inferences from hydrodynamic compressible studies and incompressible MHD flows are extended for compressible MHD shear flows.

1.3.1.1 Incompressible MHD shear flows

Two studies are performed in this dissertation to understand pressure-velocity-magnetic-field interactions in incompressible MHD shear flows:

1. Study 1 – homogeneously sheared MHD flows.

2. Study 2 – MHD mixing layers.

Homogeneously sheared flows are subjected to algebraic instability, i.e., the growth rate of perturbations is lower compared to modal instabilities seen in mixing layers (Landahl, 1980). Homogeneous shear flows are amenable to analytical treatments such as rapid distortion theory (RDT) (Pope, 2001). Due to these reasons, a comprehensive understanding of pressure-velocity-magnetic-field interactions can be made possible in the case of homogeneous shear. These inferences are then

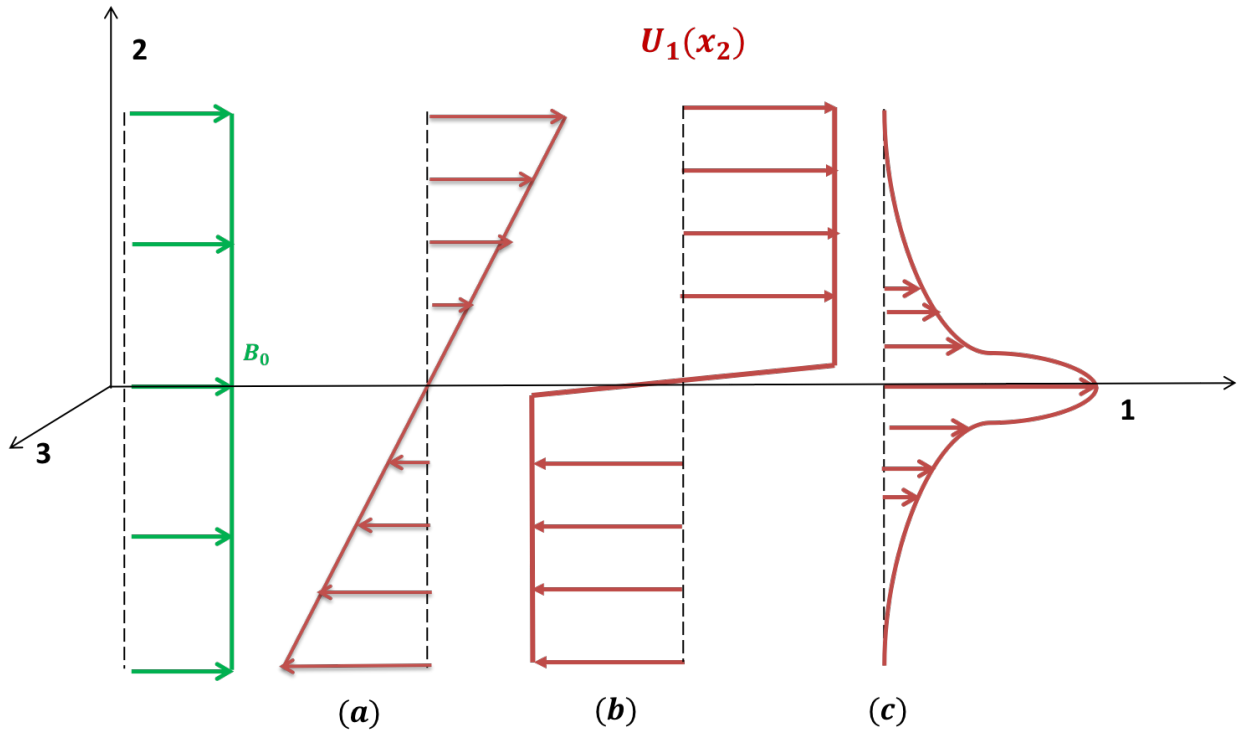

Figure 1.2: A sketch of the various shear flows studied in this dissertation. (a) Homogeneous shear, (b) mixing layer and (c) planar jets. Magnetic field is applied in the streamwise direction, as shown, in all the studies.

extended to MHD mixing layers, in which shear is inhomogeneous in nature. The presence of an inflection point also results in modal instability, due to which perturbations grow exponentially (Rayleigh, 1879). In both of the flow configurations, magnetic field is applied along the streamwise direction, which was identified by the work of Chandrasekhar (1961) to be stabilizing to flow instabilities. The schematics depicting mean velocity and magnetic fields for homogeneous shear and mixing layer are shown in figures 1.2 (a) and (b).

1.3.1.2 Compressible MHD shear flows

To understand pressure-velocity-magnetic-field interactions in the case of compressible MHD shear flows in the third study, we investigate:

1. Compressible MHD homogeneous shear

2. MHD planar jets.

As discussed previously, homogeneous shear due to its amenability to analysis leads to a better understanding of the interactions in acoustic and magnetic timescales. MHD planar jets are more complex than mixing layers due to the presence of two inflection points. The flow is susceptible to multiple modal instabilities. A schematic of planar jet mean velocity profile is shown in figure 1.2 (c).

We now present a survey of literature specific to each of the studies.

1.4 Study 1 - Incompressible MHD homogeneous shear[1]

Evolution of velocity and magnetic perturbations in the presence of uniform mean flow shear and a parallel background magnetic field is the canonical problem examined in this study. This problem is of broad interest and it is widely studied in the context of elemental shear dynamo (McWilliams, 2012) and Magnetorotational instability (Herault *et al.*, 2011; Kirillov *et al.*, 2014). This study examines such homogeneously sheared MHD flows to establish the fundamental nature of velocity-magnetic field interactions and their dependence on background magnetic field

[1]Reprinted with permission from Divya Sri Praturi, Diane Collard and Sharath S. Girimaji. The effect of magnetic field on perturbation evolution in homogeneously sheared flows. Journal of Fluid Mechanics (in production). Copyright [2018] by Cambridge University Press.

strength. Shear flows with uniform mean velocity experience a transient algebraic growth of perturbations (Landahl, 1980). Normal mode analysis is inapplicable as the flow does not permit exponentially growing perturbations. Nonmodal analysis needs to be performed in order to understand the algebraically growing transient dynamics (Trefethen *et al.*, 1993).

Homogeneously sheared MHD flows in the incompressible limit with a constant magnetic field have been studied using nonmodal analysis (Lerner & Knobloch, 1985; Chagelishvili *et al.*, 1993; Zaqarashvili, 1997; Dimitrov *et al.*, 2011). Lerner & Knobloch (1985) performed nonmodal analysis and identified solutions to the asymptotic behavior of magnetic field as a function of viscosity and resistivity. They also performed energy analysis that indicates resistivity and viscosity to have a stabilizing influence on the growth of perturbations. Their analysis is restricted to investigating the asymptotic behavior of magnetic field perturbations. Chagelishvili *et al.* (1993) identified a new transient amplification mechanism of two-dimensional magnetoacoustic waves under the influence of low streamwise magnetic field. Dimitrov *et al.* (2011) derived analytical solutions for the perturbation velocity and magnetic fields in terms of Confluent Heun functions. The authors also characterized the asymptotic amplification coefficient of slow magnetosonic waves for long wavelengths. The studies of Chagelishvili *et al.* (1993) and Dimitrov *et al.* (2011) restricted the physical analyses to inviscid, low magnetic field regime.

Background magnetic fields in nature and engineering vary by many orders of magnitude from an astrophysical flow ($\approx 10^{-6}$ Tesla) to a plasma propulsion jet (≈ 2 Tesla) (Olsen *et al.*, 2013). In addition, applications such as flow control necessitate a thorough understanding of transient and asymptotic behavior of both velocity and magnetic field perturbations at different magnetic field strengths. As a result, there is a need to further the analyses in literature and characterize the behavior of individual perturbation modes at different field strengths. Furthermore, the behavior of perturbation wavevectors that are not aligned with the mean flow or applied magnetic field must be characterized. It is also important to note that previous studies are restricted to linear analyses and the results have not been confirmed against full numerical simulations.

The objective of this study is to identify fundamental stabilization mechanisms in MHD shear

flows and characterize their behavior as a function of magnetic field strength and wavevector orientation. Toward that end, the linear analyses of Lerner & Knobloch (1985); Chagelishvili *et al.* (1993); Dimitrov *et al.* (2011) is furthered to study the small perturbation evolution in MHD shear flows. The aim is to:

1) Establish the behavior of perturbation fields at different parameter regimes (magnetic field strength - B_0 and perturbation wavevector orientation - β) using linear analysis of the initial value problem. The notation and approach followed is that of rapid distortion theory (Pope, 2001) for homogeneously sheared flows.

2) Perform direct numerical simulations (DNS) to closely examine processes such as pressure redistribution, kinetic energy production, kinetic-magnetic energy exchange and magnetic stretching.

3) Develop general inferences on the stabilizing effect of magnetic field on MHD shear flows.

1.5 Study 2 - Incompressible mixing layers

Imposed magnetic field is known to exert two distinct influences on the stability of mixing layers in conducting fluids: (i) linear effect – strong magnetic field prevents the onset of Kelvin-Helmholtz (KH) instability; and, (ii) nonlinear effect – weak magnetic field permits the inception of KH instability, but disrupts its later development. The goal of this study is to characterize the spatio-temporal evolution of perturbations in magnetohydrodynamic (MHD) mixing layers at different magnetic field strengths and contrast them against the hydrodynamic KH instability onset and development.

Chandrasekhar (1961) was the first to perform modal linear stability analysis of MHD equations for the case of infinitesimally-thin mixing layer. The stability of mixing layers is characterized in terms of Alfvén Mach number, M_A, defined as:

$$M_A \equiv \frac{V_A}{\Delta U/2}, \tag{1.1}$$

where, V_A is the Alfvén wave velocity and ΔU is the differential velocity between the two streams constituting the mixing layer. The author demonstrates that when the magnetic field is strong enough that $M_A \geq 1$, the flow is linearly stable. In other words, when the magnetic field is strong, the onset of KH instability is entirely eliminated leading to a complete stabilization of the flow. Lau & Liu (1980) then extended the analysis and finding to a finite-thickness mixing layer. These findings have been verified by many simulations, but the precise stabilization mechanism has not been clearly explicated.

If the magnetic field is weak, i.e., $M_A < 0.2$, the linear stabilizing influence is too weak to prevent the onset of KH instability. Then, a different mechanism - called resistive "tearing" instability - curtails the perturbation growth in the nonlinear regime. Many numerical studies have been performed to understand resitive instability and ensuing stabilization (Malagoli *et al.*, 1996; Frank *et al.*, 1996; Palotti *et al.*, 2008; Obergaulinger *et al.*, 2010; Mak *et al.*, 2017). Frank *et al.* (1996) also examine intermediate magnetic fields ($M_A = 0.4, 0.8$). Most of these numerical studies focus on compressible mixing layers of unit Mach number. Compressibility in itself is known to stabilize mixing layers (Karimi & Girimaji, 2016, 2017). This renders the demarcation of compressibility effect and magnetic field influence difficult. The only incompressible KH instability study was performed by Mak *et al.* (2017) to quantify the level of disruption in the weak magnetic field regime, $M_A < 0.1$. No numerical study thus far has addressed the entire magnetic field regime in the incompressible limit.

We aim to delineate the physical features at different stages of incompressible MHD mixing-layer spatio-temporal development that lead to perturbation stabilization or amplification. Toward that end, linear analysis and numerical simulations of full nonlinear incompressible MHD equations is performed to:

1. Examine the relevant dimensionless parameters that describe the evolution of incompressible MHD mixing layers at different (streamwise) magnetic field strengths.

2. Investigate and explicate the velocity-pressure-magnetic field interaction mechanisms that lead to KH stabilization in the linear regime and curtailed amplification in nonlinear regime.

3. Characterize the evolution of circulation, suction pressure and key instability measures as a function of magnetic field strength. Of particular interest is the degree of amplification of various perturbations at different magnetic field strengths.

1.6 Study 3 - Compressible planar jets

As mentioned in the previous section, many studies in literature examined the behavior of MHD shear layers in the presence of background magnetic field and compressibility. When acting alone, compressibility and magnetic field are stabilizing. However, when acting together, Sen (1964) identified the effect of compressibility to be stabilizing or destabilizing depending upon the ratio of streaming and magneto-acoustic speeds. When the streaming speed is greater than the magneto-acoustic speed, compressibility is stabilizing and vice-versa. As mentioned in the previous section, nonlinear evolution of MHD mixing layers at sonic Mach number and low magnetic fields has been extensively studied. Many planar jet studies have also been restricted to a similar regime (Min, 1997; Keppens & Tóth, 1999; Baty & Keppens, 2002, 2006). As this is the regime of relevance for astrophysical plasmas, nonlinear studies of jets focussed at understanding the morphology of compressible jets as they go through shocks.

As a result, similar to previous studies, there is a need to investigate the behavior of a wide range of magnetic field strengths and Mach numbers to comprehensively understand the effects of compressibility and magnetic field. Further, the explicit roles played by magnetic pressure and tension at different levels of compressibility need to be investigated. Toward that end, the aim of this study is to:

1. Perform linear analysis to understand the nature of pressure-velocity-magnetic-field interactions at different Mach numbers and magnetic field strengths. Specifically, the effect of compressibility on the agencies of interaction caused by magnetic pressure and magnetic tension are examined.

2. Perform numerical simulations of full compressible, resistive MHD planar jets perturbed by a single streamwise mode to examine exchanges between kinetic, magnetic and internal

energies.

3. Perform numerical simulations of random, isotropic initial modes to bring together the knowledge base on the effects of compressibility and magnetic fields on single modes of various orientations.

1.7 Dissertation outline

The following is the outline for this dissertation. Chapter II performs the linear and energy analyses of incompressible and compressible MHD equations for all the free shear flows. Chapter III presents the description of the numerical methods used for the sake of performing direct numerical simulations of MHD shear flows. The results of simulations and comparisons with analysis for the case of homogeneous shear flows are presented in Chapter IV. Chapter V presents the evolution of incompressible mixing layers in the presence of streamwise applied magnetic field of various strengths. Chapter VI presents the evolution of pressure, kinetic and magnetic energies for the case of compressible MHD planar jets subjected to a streamwise applied magnetic field. The inferences from all the above studies regarding the nature of pressure-velocity-magnetic field interactions are made in Chapter VII.

2. GOVERNING EQUATIONS

The goal of this thesis is to investigate pressure-velocity-magnetic field interactions in sheared plasma flows at various speed regimes. Plasma flows comprise of ions of multiple charges, electrons and neutral atoms. As mentioned in the introduction, despite the presence of multiple species, a single-fluid MHD approximation holds true for long wavelength, low frequency plasmas. The implications of single fluid assumption for a plasma are presented in detail here (Chen, 1994; Kulsrud, 2005):

1. The long wavelength assumption implies that we consider length scales that are larger than the electron/ion gyroradius and Debye length.

2. Plasma is considered to be of low frequency when we investigate the dynamics on time scales longer compared to electron/ion cyclotron times.

3. The plasma is quasi-neutral.

4. A single-fluid assumption also implies identical electron and ion temperatures. This can be achieved when the species collision frequencies are high.

We consider three-dimensional compressible, viscous, resistive MHD equations for analysis and numerical simulations in this study.

The conservation of mass for a fluid of density, ρ and velocity, $\vec{V}$, is given by:

$$\frac{\partial \rho}{\partial t} + \vec{\nabla} \cdot (\rho \vec{V}) = 0. \tag{2.1}$$

The momentum balance equation of the fluid subject to pressure, viscous and Lorentz forces is given by:

$$\rho \left(\frac{\partial \vec{V}}{\partial t} + (\vec{V} \cdot \vec{\nabla}) \vec{V} \right) = -\vec{\nabla} p + \vec{J} \times \vec{B} + \vec{\nabla} \cdot \vec{\vec{\tau}}, \tag{2.2}$$

where, $p, \vec{J}$ and $\vec{B}$ are the fluid pressure, current density and magnetic field, respectively of the MHD fluid. $\vec{\vec{\tau}}$ is the viscous stress tensor given by:

$$\vec{\vec{\tau}} = \mu \left(\vec{\nabla}\vec{V} + (\vec{\nabla}\vec{V})^T \right) + \lambda \vec{\nabla} \cdot \vec{V} \vec{\vec{I}}, \tag{2.3}$$

where, μ and $\lambda = -2\mu/3$ are the dynamic viscosity and bulk viscosity coefficient. Magnetic field evolution is given by Ohm's law:

$$\frac{\partial \vec{B}}{\partial t} = \vec{\nabla} \times \vec{V} \times \vec{B} + D_\eta \nabla^2 \vec{B}; \qquad D_\eta = \frac{\eta}{\mu_0}, \tag{2.4}$$

where, D_η, the magnetic diffusivity can be expressed in terms of the resistivity of MHD fluid, η, and the permeability of free space, μ_0, as $D_\eta = \eta/\mu_0$. In addition, magnetic field should satisfy divergence-free condition at all times, i.e.,

$$\vec{\nabla} \cdot \vec{B} = 0. \tag{2.5}$$

Current density, $\vec{j}$, in the MHD fluid can be expressed in terms of magnetic field, $\vec{B}$, and electric field, $\vec{E}$, using Ampère-Maxwell equation:

$$\vec{\nabla} \times \vec{B} = \mu_0 \vec{j} + \mu_0 \epsilon_0 \frac{\partial \vec{E}}{\partial t}, \tag{2.6}$$

where, ϵ_0 and μ_0 are the vacuum permittivity and permeability, respectively. The temporal variation of electric field term on the right hand side of equation (2.6) can be neglected for the cases where flow velocity is insignificant compared to the speed of light, i.e., $|\vec{U}| \ll c$. The governing equation for the evolution of the sum of internal, kinetic and magnetic energies is given by:

$$\frac{\partial E_{tot}}{\partial t} + \vec{\nabla} \cdot \left(\vec{V}(E_h + p) - \kappa \vec{\nabla} T - \vec{V} \cdot \vec{\vec{\tau}} + \frac{\vec{E} \times \vec{B}}{\mu_0} \right) = 0, \tag{2.7}$$

$$E_{tot} = \frac{\rho\vec{V}\cdot\vec{V}}{2} + \frac{p}{\gamma-1} + \frac{\vec{B}\cdot\vec{B}}{2\mu_0}; \qquad E_h = \frac{\rho\vec{V}\cdot\vec{V}}{2} + \frac{p}{\gamma-1}, \tag{2.8}$$

where, κ is the thermal conductivity of the MHD fluid.

2.1 Incompressible limit

We now consider the three-dimensional viscous, resistive MHD equations in the incompressible limit Davidson (2002):

$$\rho\left(\frac{\partial\vec{U}}{\partial t} + (\vec{U}\cdot\vec{\nabla})\vec{U}\right) = -\vec{\nabla}p + \vec{j}\times\vec{B} + \vec{\nabla}\cdot\bar{\bar{\tau}}, \tag{2.9}$$

$$\vec{\nabla}\cdot\vec{U} = 0. \tag{2.10}$$

$$\frac{\partial\vec{B}}{\partial t} = \vec{\nabla}\times(\vec{U}\times\vec{B}) + D_\eta\nabla^2\vec{B}, \tag{2.11}$$

$$\vec{\nabla}\cdot\vec{B} = 0. \tag{2.12}$$

Using equation (2.6), the Lorentz force term on the right hand side of the momentum equation (2.9) can be written in terms of magnetic pressure and magnetic tension terms:

$$\begin{aligned}\vec{j}\times\vec{B} = -\vec{\nabla}\left(\frac{\vec{B}\cdot\vec{B}}{2\mu_0}\right) + \frac{1}{\mu_0}(\vec{B}\cdot\vec{\nabla})\vec{B} = -\vec{\nabla}\left(p_m\right) \\ + \frac{1}{\mu_0}(\vec{B}\cdot\vec{\nabla})\vec{B}.\end{aligned} \tag{2.13}$$

The magnetic pressure (p_m) supplements the fluid pressure (p_f), where as, magnetic tension gives rise to Alfvén waves. The Poisson equation for total pressure ($p_t = p_f + p_m$) can be obtained by taking the divergence of the momentum equation (2.9) (assuming ρ is homogeneous):

$$\nabla^2 p_t = \nabla^2 p_m + \nabla^2 p_f = -\rho(\vec{\nabla}\vec{U} : \vec{\nabla}\vec{U}) + \frac{1}{\mu_0}(\vec{\nabla}\vec{B} : \vec{\nabla}\vec{B}). \tag{2.14}$$

It is evident that the magnetic tension contributes to the total pressure in the flow field. The evolution of magnetic field, $\vec{B}$, is given by Ohm's law:

Vorticity evolution equation is derived by taking the curl of the momentum equation (2.9):

$$\frac{\partial \vec{\omega}}{\partial t} + \left(\vec{U}\cdot\vec{\nabla}\right)\vec{\omega} = \left(\vec{\omega}\cdot\vec{\nabla}\right)\vec{U} - \left(\vec{j}\cdot\vec{\nabla}\right)\vec{B} + \left(\vec{B}\cdot\vec{\nabla}\right)\vec{j}. \tag{2.15}$$

For the purpose of analysis, the velocity, pressure and magnetic fields are decomposed into mean (ensemble) and perturbation fields:

$$u_i = \overline{u}_i + u_i^{'}; \qquad p = \overline{p} + p^{'}; \qquad B_i = \overline{B}_i + B_i^{'} \tag{2.16}$$

The mean can represent ensemble, time or space average as appropriate to the specific flow under consideration. The equations are derived for the most general ensemble average first. The governing equations for the mean field are given by:

$$\frac{\partial \overline{u}_i}{\partial x_i} = 0; \qquad \frac{\partial \overline{B}_i}{\partial x_i} = 0 \tag{2.17}$$

$$\begin{aligned}\frac{\partial \overline{u}_i}{\partial t} + \overline{u}_j\frac{\partial \overline{u}_i}{\partial x_j} = -\frac{1}{\rho}\frac{\partial \overline{p}}{\partial x_i} - \frac{\overline{\partial u_i^{'}u_j^{'}}}{\partial x_j} - \frac{1}{2\mu_0\rho}\frac{\partial}{\partial x_i}(\overline{B}_j\overline{B}_j) - \frac{1}{2\mu_0\rho}\frac{\overline{\partial B_j^{'}B_j^{'}}}{\partial x_i} \\ + \frac{\overline{B}_j}{\mu_0\rho}\frac{\partial \overline{B}_i}{\partial x_j} + \frac{1}{\rho\mu_0}\frac{\overline{\partial B_i^{'}B_j^{'}}}{\partial x_j} + \nu\frac{\partial^2 \overline{u}_i}{\partial x_j^2}\end{aligned} \tag{2.18}$$

$$\frac{\partial \overline{B}_i}{\partial t} + \overline{u}_j\frac{\partial \overline{B}_i}{\partial x_j} = \overline{B}_j\frac{\partial \overline{u}_i}{\partial x_j} + \overline{\frac{\partial}{\partial x_j}\left(u_i^{'}B_j^{'} - u_j^{'}B_i^{'}\right)} + \eta\frac{\partial^2 \overline{B}_i}{\partial x_j \partial x_j} \tag{2.19}$$

$$\frac{\partial \overline{\omega_i}}{\partial t} + \overline{u}_k\frac{\partial \overline{\omega}_i}{\partial x_k} = \overline{\omega}_k\frac{\partial \overline{u}_i}{\partial x_k} - \overline{j}_k\frac{\partial \overline{B}_i}{\partial x_k} + \overline{B}_k\frac{\partial \overline{j}_i}{\partial x_k} - \overline{u_k^{'}\frac{\partial \omega_i^{'}}{\partial x_k}} + \overline{\omega_k^{'}\frac{\partial u_i^{'}}{\partial x_k}} - \overline{j_k^{'}\frac{\partial B_i^{'}}{\partial x_k}} + \overline{B_k^{'}\frac{\partial j_i^{'}}{\partial x_k}}, \tag{2.20}$$

where, i, j, k take values $1, 2, 3$ and Einstein summation convention is used. Einstein summation convention is used. Overbar indicates ensemble averaging. For the case of homogeneous shear flows, ensemble average is equivalent to spatial average on the streamwise-spanwise plane.

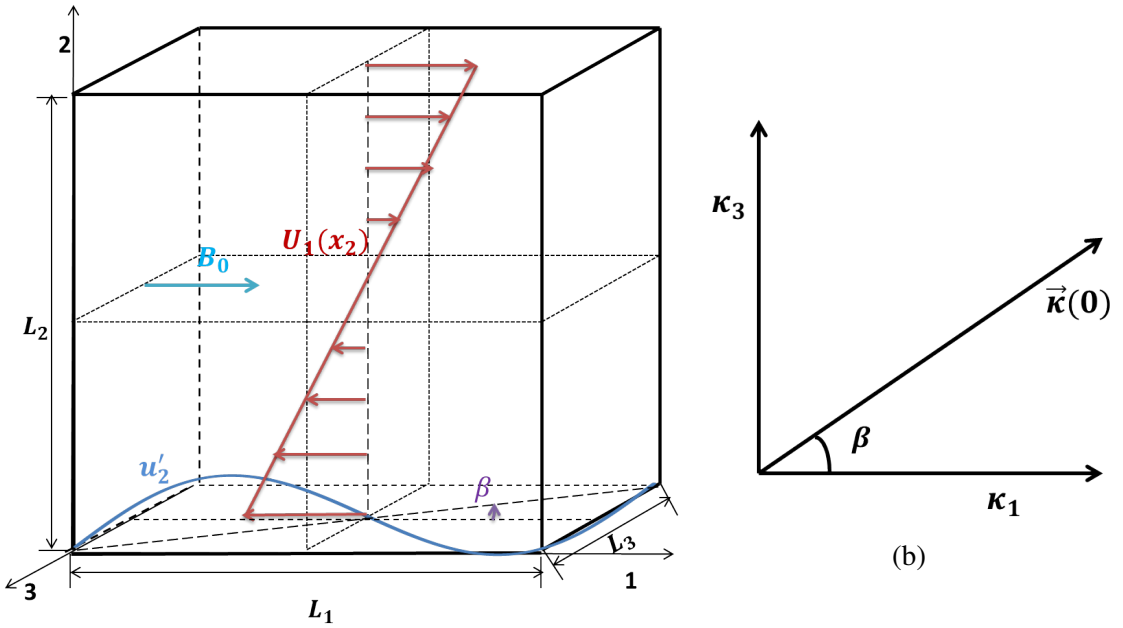

(a) (b)

Figure 2.1: (a) Problem setup (b) wavevector orientation with respect to streamwise direction. Reprinted with permission from Praturi *et al.* (in production).

2.1.1 Linear analysis for homogeneous shear flows[1]

The setup for linear analysis and numerical simulations is shown in figure 2.1a. The mean velocity is oriented along 1-direction and it varies along the 2-direction. The magnetic field is applied in the 1-direction. The co-linear alignment of velocity and magnetic fields is seen in plasma propulsion jets such as Variable specific impulse magnetoplasma rocket (VASIMR) engine (Diaz, 2000). Other magnetic field orientations will be considered in the future. In subsequent discussions, 1, 2 and 3 directions will be referred as streamwise, normal and spanwise directions. For this study we consider,

$$\bar{\boldsymbol{u}} \equiv (U_1(x_2), 0, 0); \qquad \bar{\boldsymbol{B}} \equiv (B_0, 0, 0) \tag{2.21}$$

[1]Reprinted with permission from Divya Sri Praturi, Diane Collard and Sharath S. Girimaji. The effect of magnetic field on perturbation evolution in homogeneously sheared flows. Journal of Fluid Mechanics (in production). Copyright [2018] by Cambridge University Press.

Mean density is taken to be uniform. For linear analysis, we consider an ideal MHD fluid. In direct numerical simulations (DNS), the full nonlinear and viscous/resistive effects are included. Under the assumptions of idealized MHD linear analysis, mean pressure is uniform throughout the flow field:

$$\frac{\partial \overline{p}}{\partial x_i} = 0 \tag{2.22}$$

The evolution of fluctuating fields is isolated by subtracting the mean field evolution terms from the total field evolution equations upon neglecting nonlinear terms. The resulting equations are (Chagelishvili *et al.*, 1993):

$$\frac{\partial u_i^{'}}{\partial x_i} = 0; \qquad \frac{\partial B_i^{'}}{\partial x_i} = 0 \tag{2.23}$$

$$\frac{\overline{D} u_i^{'}}{\overline{D} t} \equiv \frac{\partial u_i^{'}}{\partial t} + U_1(x_2)\frac{\partial u_i^{'}}{\partial x_1} = -u_2^{'} S \delta_{i1} - \frac{1}{\rho}\frac{\partial}{\partial x_i}\left(p^{'} + \frac{B_0 B_1^{'}}{\mu_0}\right) + \frac{B_0}{\rho \mu_0}\frac{\partial B_i^{'}}{\partial x_1} \tag{2.24}$$

$$\frac{\overline{D} B_i^{'}}{\overline{D} t} \equiv \frac{\partial B_i^{'}}{\partial t} + U_1(x_2)\frac{\partial B_i^{'}}{\partial x_1} = B_2^{'} S \delta_{i1} + B_0 \frac{\partial u_i^{'}}{\partial x_1} \tag{2.25}$$

where, the uniform flow shear is given by:

$$S \equiv \frac{dU_1}{dx_2} \tag{2.26}$$

A coordinate frame ($\boldsymbol{X}$) that convects and deforms with the mean flow is utilized to examine the flow evolution (Rogallo, 1981):

$$X_1 = x_1 - \int_0^t U_1(x_2) d\xi; \qquad X_2 = x_2; \qquad X_3 = x_3; \qquad t = t \tag{2.27}$$

Equations in the convective coordinate frame ($\boldsymbol{X}$) then become:

$$\frac{\partial u_i^{'}}{\partial X_i} - St\frac{\partial u_2^{'}}{\partial X_1} = 0 \tag{2.28}$$

$$\frac{\partial B_i^{'}}{\partial X_i} - St\frac{\partial B_2^{'}}{\partial X_1} = 0 \tag{2.29}$$

$$\frac{\partial u_i^{'}}{\partial t} = -u_2^{'} S\delta_{i1} - \frac{1}{\rho}\frac{\partial p^{'}}{\partial X_i} - \frac{B_0}{\rho\mu_0}\frac{\partial B_1^{'}}{\partial X_i} + \frac{St}{\rho}\frac{\partial p^{'}}{\partial X_1}\delta_{i2} + \frac{StB_0}{\rho\mu_0}\frac{\partial B_1^{'}}{\partial X_1}\delta_{i2} + \frac{B_0}{\rho\mu_0}\frac{\partial B_i^{'}}{\partial X_1} \tag{2.30}$$

$$\frac{\partial B_i^{'}}{\partial t} = B_0\frac{\partial u_i^{'}}{\partial X_1} + B_2^{'} S\delta_{i1} \tag{2.31}$$

Following rapid distortion theory (RDT) methodology (Taylor & Batchelor, 1949; Batchelor & Proudman, 1954; Pope, 2001; Cambon *et al.*, 1993), we now consider perturbations that are periodic in all X_i directions:

$$q^{'}(\vec{X}, t) = \hat{q}(t)e^{i\vec{\kappa}(0)\cdot\vec{X}} = \hat{q}(t)e^{i\vec{\kappa}(t)\cdot\vec{x}} \tag{2.32}$$

Due to the coordinate transformation, the wavenumbers evolve as (Pope, 2001):

$$\frac{d\kappa_i}{dt} = -\kappa_j\frac{\partial U_j}{\partial x_i} \tag{2.33}$$

For the mean velocity profile ($U_1(x_2)$) considered in this study, the above equation reduces to:

$$\frac{d\kappa_1}{dt} = 0; \qquad \frac{d\kappa_2}{dt} = -\kappa_1 S; \qquad \frac{d\kappa_3}{dt} = 0, \tag{2.34a}$$

leading to

$$\kappa_1(t) = \kappa_1(0); \qquad \kappa_2(t) = \kappa_2(0) - St\kappa_1(0); \qquad \kappa_3(t) = \kappa_3(0). \tag{2.34b}$$

The implication is that the wavevector magnitude and direction in the streamwise-spanwise plane remain constant, and the wavenumber in the normal direction grows linearly. The perturbation amplitudes evolve as (using equation (2.34b)):

$$\frac{d\hat{u}_i}{dt} = -\hat{u}_2 S\delta_{i1} - i\kappa_i\left(\frac{\hat{p}}{\rho} + \frac{B_0}{\rho\mu_0}\hat{B}_1\right) + \frac{B_0}{\rho\mu_0}i\kappa_1\hat{B}_i \tag{2.35}$$

$$\frac{d\hat{B}_i}{dt} = \hat{B}_2 S\delta_{i1} + i\kappa_1 B_0\hat{u}_i \tag{2.36}$$

subject to the divergence-free constraints,

$$i\kappa_i \hat{u}_i = 0; \qquad i\kappa_i \hat{B}_i = 0 \tag{2.37}$$

It is evident from the above equations that the stability characteristics of the linear system are contingent on the initial wavenumber of the perturbations. The equations demonstrate that κ_2 plays a critical role in the perturbation evolution as it is the only wavenumber component that changes with time. We consider two distinct classes of initial conditions: $\kappa_2 \neq 0$; and $\kappa_2 = 0$.

Initial perturbations with $\boldsymbol{\kappa_2(0) \neq 0}$. In the early stages, the initial value of κ_2 plays a critical role in determining the evolution of the perturbations. This transient stage can have interesting implications on perturbation growth. Chagelishvili *et al.* (1993) have investigated the early time energy interactions for two-dimensional perturbations on the streamwise-normal ($\kappa_1 - \kappa_2$) plane. Further analytical examination of this parameter regime will be performed in future works.

Initial perturbations with $\boldsymbol{\kappa_2(0) = 0}$. In this study, we focus on perturbations which are initially located on the $\kappa_1 - \kappa_3$ plane for several reasons. First and foremost, these perturbations provide crucial insight into the long-term stability characteristics of general shear flow instabilities subject to streamwise magnetic field. Secondly, due to the nature of κ_2 growth, the asymptotic stability of the linear equations can be completely captured by this initial condition. Finally, this system is amenable to rigorous mathematical analysis which leads to profound insight into the stabilizing influence of magnetic field. We express these initial wavevectors in terms of their magnitude κ_0 and orientation β with respect to the streamwise direction (see figure 2.1b). The wavenumber equation (2.34b) can be written as:

$$\kappa_1(t) = \kappa_0 \cos\beta; \qquad \kappa_2(t) = -\kappa_0 St \cos\beta; \qquad \kappa_3(t) = \kappa_0 \sin\beta \tag{2.38}$$

Poisson equation for total pressure amplitude, $(\hat{p} + B_0 \hat{B}_1/\mu_0)$, can be obtained using equa-

tions (2.34b), (2.35) and (2.37):

$$\frac{\hat{p}}{\rho} + \frac{B_0}{\rho\mu_0}\hat{B}_1 = \frac{2i\kappa_1}{\kappa^2}\hat{u}_2 S \tag{2.39}$$

Equation (2.35) then becomes,

$$\frac{d\hat{u}_i}{dt} = \hat{u}_2 S\left(-\delta_{i1} + \frac{2\kappa_1\kappa_i}{\kappa^2}\right) + i\frac{B_0}{\rho\mu_0}\kappa_1\hat{B}_i \tag{2.40}$$

The perturbation equations (2.36), and (2.40) are non-dimensionalized using Alfvén wave speed (V_A), mean flow shear, initial wavenumber and imposed magnetic field:

$$u_i^* = u_i/V_A; \qquad V_A = \frac{B_0}{\sqrt{\rho\mu_0}}; \qquad \tau = St; \qquad \kappa_i^* = \kappa_i/\kappa_0; \qquad B_i^* = B_i/B_0 \tag{2.41}$$

Finally, the governing dimensionless equations are:

$$\frac{d\hat{u}_i^*}{d\tau} = \hat{u}_2^*\left(-\delta_{i1} + \frac{2\cos(\beta)\kappa_i^*}{1+\cos^2(\beta)\tau^2}\right) + iR_A\cos(\beta)\hat{B}_i^* \tag{2.42}$$

$$\frac{d\hat{B}_i^*}{d\tau} = \hat{B}_2^*\delta_{i1} + iR_A\cos(\beta)\hat{u}_i^* \tag{2.43}$$

$$\text{where,} \qquad R_A \equiv \frac{\kappa_0 V_A}{S} = \frac{\text{shear timescale}}{\text{magnetic timescale}} \tag{2.44}$$

From the above equations, it can be seen that the flow behavior can be completely characterized in terms of the parameters, R_A and β. The role of R_A has been recognized to some extent in the other studies (Chagelishvili *et al.*, 1993). The influence of β is examined in detail for the first time in this study. Equations (2.42), (2.43) clearly indicate the velocity and magnetic field perturbations are coupled via the last terms on their right hand sides. $R_A\cos(\beta)$ is the coupling parameter in the problem. Therefore for a given value of R_A, streamwise perturbations experience the highest degree of coupling. The coupling becomes weaker with increasing β. For spanwise orientations, velocity and magnetic field perturbations are decoupled.

We now investigate the evolution of the magnitudes of velocity and magnetic perturbation

amplitudes. For the ease of notation, we denote the dimensionless variables, q^* as q. In order to obtain the evolution equation for perturbation kinetic energy, we multiply equation (2.42) with $\bar{\hat{u}}_i$, the complex conjugate of $\hat{u}_i$.

$$\bar{\hat{u}}_i \frac{d\hat{u}_i}{d\tau} = \bar{\hat{u}}_i \hat{u}_2 \left(-\delta_{i1} + \frac{2\cos(\beta)\kappa_i}{1 + \cos^2(\beta)\tau^2} \right) + iR_A \cos(\beta) \hat{B}_i \bar{\hat{u}}_i \tag{2.45}$$

Utilizing the complex conjugate of the continuity equation (equation 2.37), the above kinetic energy equation (2.45) reduces to:

$$\bar{\hat{u}}_i \frac{d\hat{u}_i}{d\tau} = -\bar{\hat{u}}_i \hat{u}_2 \delta_{i1} + iR_A \cos(\beta) \hat{B}_i \bar{\hat{u}}_i \tag{2.46}$$

Similarly, equation (2.43) is multiplied by $\bar{\hat{B}}_i$ (the complex conjugate of $\hat{B}_i$) to obtain the magnetic energy equation:

$$\bar{\hat{B}}_i \frac{d\hat{B}_i}{d\tau} = \bar{\hat{B}}_i \hat{B}_2 \delta_{i1} + iR_A \cos(\beta) \bar{\hat{B}}_i \hat{u}_i \tag{2.47}$$

Summing equations (2.46), (2.47) with their complex conjugate counterparts yields:

$$\frac{1}{2} \frac{d\hat{u}_i \bar{\hat{u}}_i}{d\tau} = -Re(\bar{\hat{u}}_i \hat{u}_2)\delta_{i1} - R_A \cos(\beta) Im(\hat{B}_i \bar{\hat{u}}_i) \tag{2.48}$$

$$\frac{1}{2} \frac{d\hat{B}_i \bar{\hat{B}}_i}{d\tau} = Re(\hat{B}_2 \bar{\hat{B}}_i)\delta_{i1} + R_A \cos(\beta) Im(\hat{B}_i \bar{\hat{u}}_i) \tag{2.49}$$

where, $Re(q), Im(q)$ indicate the real and imaginary parts of a complex quantity, q. The first term on the right hand side of equation (2.48) represents production, the process in which perturbation kinetic energy is transferred from the mean flow. Similarly, the first term on the right hand side of equation (2.49) represents magnetic stretching, the process in which perturbation magnetic energy is produced by the stretching action of the mean flow. Production and magnetic stretching occur at shear (S) timescale. It can be seen that the last terms on the right hand side of equations (2.48), (2.49) are identical, but with opposite signs. This implies that they result in a harmonic exchange between magnetic and kinetic energies. The harmonic exchange process

takes place at the timescale, $V_A\kappa_0\cos(\beta)$. Therefore, $R_A\cos\beta$ determines the relative timescales of production and exchange processes.

We next investigate the energy transfer among individual components of kinetic and magnetic energies. We utilize the following notation for various energies for the sake of simplicity:

$$k \equiv \hat{u}_i\bar{\hat{u}}_i; \qquad k_1 \equiv \hat{u}_1\bar{\hat{u}}_1; \qquad k_2 \equiv \hat{u}_2\bar{\hat{u}}_2; \qquad k_3 \equiv \hat{u}_3\bar{\hat{u}}_3 \tag{2.50a}$$

$$b \equiv \hat{B}_i\bar{\hat{B}}_i; \qquad b_1 \equiv \hat{B}_1\bar{\hat{B}}_1; \qquad b_2 \equiv \hat{B}_2\bar{\hat{B}}_2; \qquad b_3 \equiv \hat{B}_3\bar{\hat{B}}_3 \tag{2.50b}$$

The governing equations for the energies in velocity components are:

$$\frac{dk_1}{d\tau} \equiv \frac{d(\hat{u}_1\bar{\hat{u}}_1)}{d\tau} = 2Re(\hat{u}_2\bar{\hat{u}}_1)\frac{2\cos^2(\beta)}{1+\cos^2(\beta)\tau^2} - 2Re(\hat{u}_2\bar{\hat{u}}_1) - 2R_A\cos(\beta)Im(\hat{B}_1\bar{\hat{u}}_1) \tag{2.51a}$$

$$\frac{dk_2}{d\tau} \equiv \frac{d(\hat{u}_2\bar{\hat{u}}_2)}{d\tau} = -2Re(\hat{u}_2\bar{\hat{u}}_2)\frac{2\cos^2(\beta)\tau}{1+\cos^2(\beta)\tau^2} - 2R_A\cos(\beta)Im(\hat{B}_2\bar{\hat{u}}_2) \tag{2.51b}$$

$$\frac{dk_3}{d\tau} \equiv \frac{d(\hat{u}_3\bar{\hat{u}}_3)}{d\tau} = 2Re(\hat{u}_2\bar{\hat{u}}_3)\frac{2\cos(\beta)\sin(\beta)}{1+\cos^2(\beta)\tau^2} - 2R_A\cos(\beta)Im(\hat{B}_3\bar{\hat{u}}_3) \tag{2.51c}$$

The first terms in equations (2.51) denote pressure redistribution. This is a consequence of the action of pressure in reorienting $\hat{u}_i$ in equation (2.42) to impose divergence-free constraint. Total pressure redistributes the energy amongst different velocity components in order to satisfy continuity. Production and pressure redistribution in equation (2.51a) have opposing effects as can be seen from the coefficients of $\hat{u}_2\bar{\hat{u}}_1$. The coefficient of production is always negative (-1), where as, the coefficient of pressure redistribution is always positive. The nature of the term $\bar{\hat{u}}_1\hat{u}_2$ can be deduced using the continuity equation:

$$\hat{u}_1\kappa_1 + \hat{u}_2\kappa_2 + \hat{u}_3\kappa_3 = 0 \tag{2.52}$$

Substituting for the values of κ_i using equation (2.38):

$$\hat{u}_1 \cos\beta - \tau\hat{u}_2 \cos\beta + \hat{u}_3 \sin\beta = 0 \tag{2.53}$$

Multiplying the above equation with the complex conjugate of $\hat{u}_1$:

$$\cos\beta|\hat{u}_1|^2 + \bar{\hat{u}}_1\hat{u}_3 \sin\beta = \tau\bar{\hat{u}}_1\hat{u}_2 \cos\beta \tag{2.54}$$

Therefore, the term $\bar{\hat{u}}_1\hat{u}_2$ can be written as:

$$\bar{\hat{u}}_1\hat{u}_2 = \frac{1}{\tau}\left(|\hat{u}_1|^2 + \bar{\hat{u}}_1\hat{u}_3 \tan\beta\right) \tag{2.55}$$

For $\beta = 0°$, continuity equation stipulates $\bar{\hat{u}}_1\hat{u}_2$ to be always positive. For other orientations, $\bar{\hat{u}}_1\hat{u}_2$ could be positive or negative depending upon the initial conditions. However, the value of $\bar{\hat{u}}_1\hat{u}_2$ for all orientations decreases with time as τ^{-1}.

The evolution equations for energies in the magnetic field components are given by:

$$\frac{db_1}{d\tau} \equiv \frac{d(\hat{B}_1\bar{\hat{B}}_1)}{d\tau} = 2Re(\hat{B}_2\bar{\hat{B}}_1) + 2R_A \cos(\beta) Im(\hat{B}_1\bar{\hat{u}}_1) \tag{2.56a}$$

$$\frac{db_2}{d\tau} \equiv \frac{d(\hat{B}_2\bar{\hat{B}}_2)}{d\tau} = 2R_A \cos(\beta) Im(\hat{B}_2\bar{\hat{u}}_2) \tag{2.56b}$$

$$\frac{db_3}{d\tau} \equiv \frac{d(\hat{B}_3\bar{\hat{B}}_3)}{d\tau} = 2R_A \cos(\beta) Im(\hat{B}_3\bar{\hat{u}}_3) \tag{2.56c}$$

Unlike velocity field, there is no mechanism to redistribute the energy amongst different magnetic field components. Similar conclusions to $\hat{u}_2\bar{\hat{u}}_1$ can be drawn regarding the magnetic stretching production term $\hat{B}_2\bar{\hat{B}}_1$.

$$\bar{\hat{B}}_1\hat{B}_2 = \frac{1}{\tau}\left(|\hat{B}_1|^2 + \bar{\hat{B}}_1\hat{B}_3 \tan\beta\right) \tag{2.57}$$

Overall, the energy interactions involve four important processes: production, magnetic stretching, pressure redistribution and harmonic kinetic-magnetic exchange. It can be observed that pro-

duction and magnetic stretching depend on the behavior of normal components of velocity and magnetic fields, $u_2^{'}, B_2^{'}$. Therefore, it is crucial to examine the evolution of $u_2^{'}, B_2^{'}$ at different R_A, β.

We examine the evolution of spanwise perturbations ($\beta = 90°$) first, followed by an investigation of other orientations ($\beta \in [0°, 90°)$).

2.1.1.1 Spanwise Perturbations, $\beta = 90°$

As seen in previous sections, this represents a special limit since the velocity and magnetic fields are decoupled. The wavevectors remain at their initial state:

$$\kappa_1(t) = 0; \qquad \kappa_2(t) = 0; \qquad \kappa_3(t) = \kappa_3(0) \tag{2.58}$$

Total pressure Poisson equation becomes:

$$\frac{1}{\rho}\hat{p} + \frac{B_0}{\mu_0 \rho}\hat{B}_1 = 0 \tag{2.59}$$

The individual velocity components evolve as:

$$\frac{d\hat{u}_1}{d\tau} = -\hat{u}_2; \qquad \frac{d\hat{u}_2}{d\tau} = 0; \qquad \frac{d\hat{u}_3}{d\tau} = 0 \tag{2.60}$$

The velocity equations are unaffected by pressure similar to spanwise perturbations in hydrodynamic homogeneous shear flow (Kumar *et al.*, 2014). This is called pressure-released behavior (Simone *et al.*, 1997). Integrating the above equations,

$$\hat{u}_1(\tau) = -\hat{u}_2(0)\tau + \hat{u}_1(0); \qquad \hat{u}_2(\tau) = \hat{u}_2(0); \qquad \hat{u}_3(\tau) = \hat{u}_3(0) \tag{2.61}$$

If $\hat{u}_1, \hat{u}_3$ are zero initially, the kinetic energy (k) in the flow will evolve with respect to the initial kinetic energy (k_0) as (Simone *et al.*, 1997):

$$\frac{k}{k_0} = 1 + \tau^2 \tag{2.62}$$

The individual magnetic components evolve as:

$$\frac{d\hat{B}_1}{d\tau} = \hat{B}_2; \qquad \frac{d\hat{B}_2}{d\tau} = 0; \qquad \frac{d\hat{B}_3}{d\tau} = 0 \tag{2.63}$$

This implies,

$$\hat{B}_1(\tau) = \hat{B}_2(0)\tau + \hat{B}_1(0); \qquad \hat{B}_2(\tau) = \hat{B}_2(0); \qquad \hat{B}_3(\tau) = \hat{B}_3(0) \tag{2.64}$$

Magnetic perturbations remain unchanged when the initial magnetic energy is zero.

2.1.1.2 Perturbation orientations with $\beta \in [0°, 90°)$

Recall that the evolution of kinetic and magnetic energies critically depends on the behavior of $u_2^{'}$ and $B_2^{'}$. In order to eliminate the explicit dependence of β on $\hat{u}_2, \hat{B}_2$, we define a new timescale (τ^*), similar to the transformation performed by Dimitrov *et al.* (2011).

$$\tau^* = \tau \cos\beta \tag{2.65}$$

The resultant equations are given by:

$$\frac{d\hat{u}_2}{d\tau^*} = -\frac{2\tau^*\hat{u}_2}{1+\tau^{*2}} + iR_A\hat{B}_2 \tag{2.66a}$$

$$\frac{d\hat{B}_2}{d\tau^*} = iR_A\hat{u}_2 \tag{2.66b}$$

This is a coupled system of homogeneous linear ordinary differential equations with R_A as the coupling parameter. In order to isolate the evolution of each field, a second derivative with respect

to τ^* is calculated. The resulting equations are:

$$\frac{d^2\hat{u}_2}{d\tau^{*2}} = -\frac{2\tau^*}{1+\tau^{*2}}\frac{d\hat{u}_2}{d\tau^*} - 2\hat{u}_2\frac{1-\tau^{*2}}{(1+\tau^{*2})^2} + iR_A\frac{d\hat{B}_2}{d\tau^*} \tag{2.67a}$$

$$\frac{d^2\hat{B}_2}{d\tau^{*2}} = iR_A\frac{d\hat{u}_2}{d\tau^*} \tag{2.67b}$$

Using equations (2.66a), (2.66b), the decoupled equations for $\hat{u}_2$, and $\hat{B}_2$ are given by:

$$\frac{d^2\hat{u}_2}{d\tau^{*2}} + \frac{2\tau^*}{1+\tau^{*2}}\frac{d\hat{u}_2}{d\tau^*} + 2\hat{u}_2\frac{1-\tau^{*2}}{(1+\tau^{*2})^2} + R_A^2\hat{u}_2 = 0 \tag{2.68a}$$

$$\frac{d^2\hat{B}_2}{d\tau^{*2}} + \frac{2\tau^*}{1+\tau^{*2}}\frac{d\hat{B}_2}{d\tau^*} + R_A^2\hat{B}_2 = 0 \tag{2.68b}$$

To facilitate an analytical solution, the following transformation of variables is performed (Lerner & Knobloch, 1985)

$$\hat{u}_2 = g(\tau^*)\exp\left(-\int\frac{\tau^* d\tau^*}{1+\tau^{*2}}\right) = \frac{g(\tau^*)}{\sqrt{1+\tau^{*2}}} \tag{2.69a}$$

$$\hat{B}_2 = h(\tau^*)\exp\left(-\int\frac{\tau^* d\tau^*}{1+\tau^{*2}}\right) = \frac{h(\tau^*)}{\sqrt{1+\tau^{*2}}} \tag{2.69b}$$

The new variables g and h represent scaled values of velocity and magnetic field perturbation amplitudes. The resulting equations for the evolution of $g(\tau^*), h(\tau^*)$ are:

$$\frac{d^2g}{d\tau^{*2}} = -\left(\frac{1-2\tau^{*2}}{(1+\tau^{*2})^2} + R_A^2\right)g \tag{2.70a}$$

$$\frac{d^2h}{d\tau^{*2}} = -\left(-\frac{1}{(1+\tau^{*2})^2} + R_A^2\right)h \tag{2.70b}$$

A similar magnetic field evolution equation (2.70b) was derived by Dimitrov *et al.* (2011). Those authors note that equation (2.70b) resembles the effective Schrödinger equation, and derived an analytical solution in terms of Confluent Heun functions. The solution is not amenable to simple physical analysis. In this study, we further the work of Dimitrov *et al.* (2011) to identify different parameter regimes of self-similar behavior and characterize the precise nature of energy exchange

between velocity and magnetic fields. Following the analysis, we perform DNS to verify the analytical findings.

It is evident from equations (2.70a), (2.70b) that, for a given R_A, the $u_2^{'}$ and $B_2^{'}$ perturbations are self-similar in scaled time τ^* for all β. The value of β merely determines the timescale of evolution.

The first term on the right hand side of equation (2.70a) represents the pressure reorientation mechanism which manifests as pressure redistribution process in the energy equation discussed previously. Similarly, the first term on the right hand side of equation (2.70b) represents a higher order implication of the effect of total pressure on $B_2^{'}$. For any τ^*, the maximum values of the coefficients of these terms are of the order unity. The last terms on the right hand sides of equations (2.70a), (2.70b) represent the effect of harmonic exchange on the evolution of $\hat{u}_2$ and $\hat{B}_2$. If the value of R_A under consideration is larger than unity, the second terms influence the physical processes from the beginning. Taking these considerations into account, we examine different regimes of R_A to identify dominant behavior: $R_A \ll 1$ and $R_A \gg 1$.

2.1.1.2.1 $R_A \gg 1$ or High magnetic field limit

In this limit, equations (2.70a), (2.70b) simplify to:

$$\frac{d^2 g}{d\tau^{*2}} \approx -R_A^2 g \tag{2.71a}$$

$$\frac{d^2 h}{d\tau^{*2}} \approx -R_A^2 h \tag{2.71b}$$

The solutions to these equations are:

$$g(\tau^*) \approx A_1 \exp(iR_A\tau^*) + A_2 \exp(-iR_A\tau^*) \tag{2.72a}$$

$$h(\tau^*) \approx B_1 \exp(iR_A\tau^*) + B_2 \exp(-iR_A\tau^*) \tag{2.72b}$$

where, the values of A_1, A_2, B_1 and B_2 can be obtained from appropriate initial conditions. The solution for the amplitudes of $u_2^{'}$, $B_2^{'}$ can then be written as:

$$\begin{aligned}\hat{u}_2(\tau^*) &\approx A_1\frac{\exp\left(iR_A\tau^*\right)}{\sqrt{1+\tau^{*2}}} + A_2\frac{\exp\left(-iR_A\tau^*\right)}{\sqrt{1+\tau^{*2}}} \\ \hat{B}_2(\tau^*) &\approx B_1\frac{\exp\left(iR_A\tau^*\right)}{\sqrt{1+\tau^{*2}}} + B_2\frac{\exp\left(-iR_A\tau^*\right)}{\sqrt{1+\tau^{*2}}}\end{aligned} \tag{2.73}$$

The behavior of $u_2^{'}$, $B_2^{'}$ is oscillatory, as a result of the dominating influence of harmonic exchange. Due to pressure reorientation, the magnitude of $u_2^{'}$ and consequently $B_2^{'}$ decrease. Therefore, using Parseval's theorem, the evolution of normal kinetic energy (k_2) in physical space is given by:

$$k_2 = \frac{\cos^2(R_A\tau^*)}{1+\tau^{*2}} \tag{2.74}$$

For the case of no initial magnetic field perturbations, the evolution of normal magnetic energy (b_2) is given by:

$$b_2 = \frac{\sin^2(R_A\tau^*)}{1+\tau^{*2}} \tag{2.75}$$

A solution to equation (2.70b), similar to equation (2.75) was derived by Lau & Liu (1980). In this limit, $u_2^{'}$ and $B_2^{'}$ are oscillatory with a phase difference of $\pi/2$ and a time period of $T = 2\pi/R_A$. This oscillatory evolution results in negligible production and magnetic stretching when averaged over a full cycle. This implies that harmonic exchange between magnetic and kinetic energy dominates at all times. As a result, equipartition of energy between perturbation velocity and magnetic fields is indicated.

2.1.1.2.2 $R_A \ll 1$ or Low magnetic field limit

We first consider the evolution of the coefficients of the first terms on the right hand sides of equations (2.70a), (2.70b). At initial times,

$$\frac{1-2\tau^{*2}}{(1+\tau^{*2})^2} \sim \mathcal{O}(1) \tag{2.76}$$

and asymptotes to zero at late times. Similarly, at early times,

$$\frac{1}{(1+\tau^{*2})^2} \sim \mathcal{O}(1) \tag{2.77}$$

and asymptotes to zero at subsequent times. Thus, the first terms dominate during the early time in the low R_A regime. At late times, however, the first terms have negligible contributions and the last terms dominate, i.e., harmonic exchange prevails. We now investigate the behavior at early times.

Early time behavior. In this limit, the last terms in equation (2.70a), (2.70b) can be omitted. This implies that exchange is negligible and pressure reorientation is the crucial process at this stage. As a result, the evolution equations for g, h can be written as follows:

$$\frac{d^2g}{d\tau^{*2}} \approx -\frac{1-2\tau^{*2}}{(1+\tau^{*2})^2}g \tag{2.78a}$$

$$\frac{d^2h}{d\tau^{*2}} \approx \frac{1}{(1+\tau^{*2})^2}h \tag{2.78b}$$

The g equation (2.78a) is identical to pure hydrodynamic case implying that the magnetic field does not affect initial behavior. The solution for such flows is given by:

$$g(\tau^*) = \frac{c_1}{\sqrt{1+\tau^{*2}}} \tag{2.79}$$

The evolution of k_2 is given by:

$$k_2 = \frac{1}{(1+\tau^{*2})^2} \tag{2.80}$$

The following is the analytical solution for $h, \hat{B}_2$:

$$h = \sqrt{1+\tau^{*2}}(c_1 + c_2 \arctan(\tau^*)) \Rightarrow \hat{B}_2 = c_1 + c_2 \arctan(\tau^*). \tag{2.81}$$

If there is no initial magnetic field perturbation then, $c_1 = 0$. c_2 can be determined from equa-

tion (2.66b). Thus, the final solution for b_2 at early times is:

$$b_2 = R_A^2 \arctan^2(\tau^*). \tag{2.82}$$

Late time behavior. For late times, harmonic exchange dominates as seen from the order of magnitude analysis performed above. As a result, the evolution of $\hat{u}_2$ and $\hat{B}_2$ become oscillatory, similar to the behavior of cases with $R_A \gg 1$.

Therefore, $u_2^{'}$ and $B_2^{'}$ for flows with $R_A \ll 1$ experience a three-stage evolution: At early times, pressure reorientation determines the dynamics. However, for later stages, harmonic exchange is the dominant mechanism. At late times, the equipartition between magnetic and kinetic energies is indicated once again. The behavior at intermediate times where pressure reorientation and exchange are equally dominant will be deduced from numerical simulations.

2.1.1.3 Inferences from linear inviscid analysis of homogeneous shear

The following inferences can be made from inviscid linear analysis:

1) For spanwise wavevector orientations, the velocity and magnetic field equations are decoupled leading to pressure-released behavior. As a result, $u_1^{'}$ grows linearly and $u_2^{'}, u_3^{'}$ remain unchanged. Consequently, kinetic energy grows quadratically. Since the exchange terms are zero, all the magnetic field components remain zero if not initialized.

2) The behavior of $u_2^{'}$ and $B_2^{'}$ is critical for other orientations, $\beta \in [0°, 90°)$, as they determine the production and magnetic stretching processes, respectively.

3) For the case of perturbations with $R_A \ll 1$, $u_2^{'}$ and $B_2^{'}$ exhibit a three-stage behavior. At early times, the evolution resembles that of incompressible hydrodynamic flows. Subsequently, the kinetic-magnetic harmonic exchange dominates. This results in oscillatory evolution of $u_2^{'}$ and $B_2^{'}$ at late times.

4) For perturbations with $R_A \gg 1$, harmonic kinetic-magnetic exchange dominates and the evolution is oscillatory from the beginning.

5) At late times, irrespective of R_A, harmonic exchange between kinetic and magnetic energies dominate leading to equipartition of energy.

6) The effect of β is to merely influence the timescale of evolution. With increasing β, the kinetic-magnetic coupling becomes weaker and the evolution rate progressively slows down.

2.1.2 Linear analysis for inhomogeneously sheared mixing layers

Linear analyses of incompressible MHD equations for the case of zero thickness (Chandrasekhar, 1961) and finite thickness (Lau & Liu, 1980) mixing layers have been performed in literature. These studies perform modal stability analysis to assess asymptotic perturbation growth-rates. In contrast, in this study, we examine the initial value problem. Although an analytical solution is not possible, we aim to gain valuable insight into the spatio-temporal aspects of onset and development of KH instability.

Velocity, pressure, vorticity and magnetic fields can be decomposed into background and perturbation components:

$$\begin{aligned} u_i = \overline{u}_i + u_i^{'}; \qquad p = \overline{p} + p^{'}; \\ \omega_i = \overline{\omega}_i + \omega_i^{'}; \qquad B_i = \overline{B}_i + B_i^{'}. \end{aligned} \tag{2.83}$$

A schematic of the mixing layer problem studied here is shown in figure 2.2. Background velocity field and imposed magnetic field are given by:

$$\overline{\boldsymbol{u}} = (U_1(x_2), 0, 0); \qquad \overline{\boldsymbol{B}} = (B_0, 0, 0). \tag{2.84}$$

We refer to 1-, 2- and 3-directions as streamwise-, normal- and spanwise-directions, respectively. Under inviscid linear analysis assumptions, the background field equations simplify to (Drazin & Reid, 1981):

$$\frac{\partial \overline{p}}{\partial x_i} = 0, \tag{2.85}$$

with all the other equations identically satisfied. The fluctuating field can be extracted by subtract-

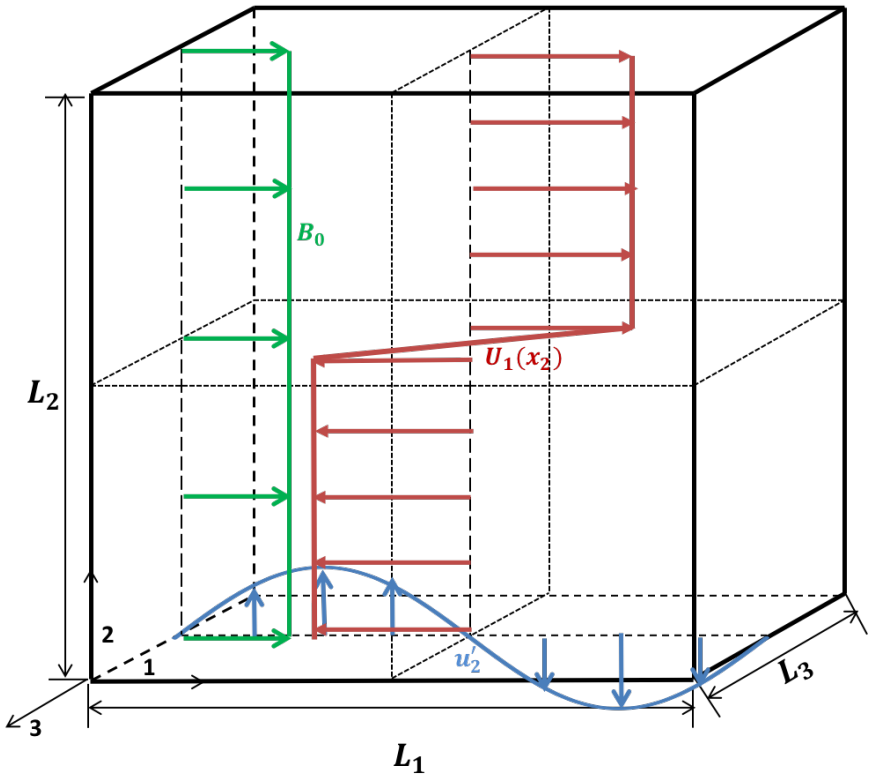

Figure 2.2: Schematic of mixing layer.

ing the equation for background flow (2.85) from the total field equations (2.9 to 2.15):

$$\frac{\partial u_i'}{\partial x_i} = 0; \qquad \frac{\partial B_i'}{\partial x_i} = 0, \tag{2.86}$$

$$\frac{\partial u_i'}{\partial t} + U_1(x_2)\frac{\partial u_i'}{\partial x_1} = -u_2' S(x_2)\delta_{i1} - \frac{1}{\rho}\frac{\partial p_t'}{\partial x_i} + \frac{B_0}{\rho\mu_0}\frac{\partial B_i'}{\partial x_1}, \quad \text{where, } S \equiv \frac{dU_1}{dx_2} \tag{2.87}$$

$$\frac{\partial B_i'}{\partial t} + U_1(x_2)\frac{\partial B_i'}{\partial x_1} = B_2' S(x_2)\delta_{i1} + B_0\frac{\partial u_i'}{\partial x_1}, \tag{2.88}$$

$$\frac{\partial \omega_3'}{\partial t} + U_1(x_2)\frac{\partial \omega_3'}{\partial x_1} = u_2'\frac{d^2U_1}{dx_2^2} + B_0\frac{\partial j_3'}{\partial x_1}, \quad \text{where, } j_3' = \frac{(\vec{\nabla}\times\vec{B'})_3}{\mu_0} \tag{2.89}$$

$$\frac{\partial^2 p_t^{'}}{\partial x_1^2} + \frac{\partial^2 p_t^{'}}{\partial x_2^2} + \frac{\partial^2 p_t^{'}}{\partial x_3^2} = -2S(x_2)\frac{\partial u_2^{'}}{\partial x_1}, \qquad \text{where, } p_t^{'} \equiv p^{'} + \frac{B_0 B_1^{'}}{\mu_0}. \tag{2.90}$$

$S(x_2)$ is the mean flow shear, $p_t^{'}$ is the total pressure perturbation and $j_3^{'}$ is the current density perturbation in the spanwise direction. As spanwise vorticity sufficiently captures the growth of KH instability, we restrict our considerations to this component.

Key interactions. From equations (2.87) and (2.89), it can be seen that the normal velocity, $u_2^{'}$, plays a critical role in the interactions as it appears in the source term of streamwise velocity and spanwise vorticity equations. Indeed, it is the sole source contributing to kinetic energy and vorticity production. Similarly, normal magnetic field, $B_2^{'}$, is important as it is the sole source contributing to magnetic stretching production in equation (2.88). Although production terms of kinetic and magnetic energies are resident in their streamwise components, $u_1^{'}, B_1^{'}$, the agency of production is resident in the normal components, $u_2^{'}, B_2^{'}$. The total pressure perturbation in equation (2.90) retains the same form as seen in the hydrodynamic limit.

We now transform the above fluctuating field equations to a coordinate system that convects with the mean flow (Kovasznay, 1953):

$$X_1 = x_1 - \int_0^t U_1(x_2) d\xi; \qquad X_2 = x_2; \qquad X_3 = x_3; \qquad t = t. \tag{2.91}$$

The equations in the new convecting coordinate frame are:

$$\frac{\partial u_i^{'}}{\partial X_i} - S^*(x_2)\frac{\partial u_2^{'}}{\partial X_1} = 0; \qquad \frac{\partial B_i^{'}}{\partial X_i} - S^*(x_2)\frac{\partial B_2^{'}}{\partial X_1} = 0, \tag{2.92}$$

$$\frac{\partial u_i^{'}}{\partial t} = -u_2^{'} S(x_2)\delta_{i1} - \frac{1}{\rho}\frac{\partial p_t^{'}}{\partial X_i} + \frac{S^*(x_2)\delta_{i2}}{\rho}\frac{\partial p_t^{'}}{\partial X_1} + \frac{B_0}{\rho\mu_0}\frac{\partial B_i^{'}}{\partial X_1}, \tag{2.93}$$

$$\frac{\partial B_i^{'}}{\partial t} = B_2^{'} S(x_2)\delta_{i1} + B_0 \frac{\partial u_i^{'}}{\partial X_1}, \tag{2.94}$$

$$\frac{\partial \omega_3^{'}}{\partial t} = u_2^{'} \frac{d^2 U_1}{dx_2^2} + B_0 \frac{\partial j_3^{'}}{\partial X_1}, \tag{2.95}$$

where, $S^*(x_2) = \int_0^t S(x_2) d\xi$ is the cumulative (dimensionless) deformation experienced by the fluid in the new coordinate system.

We restrict our analysis to initial perturbations with only a streamwise wavevector component as it is most responsible for KH instability (Chandrasekhar, 1961). The role of obliqueness, i.e., modes with both streamwise and spanwise components, is to only increase the timescale of coupling between velocity and magnetic fields (Section 2.1.1). We investigate modes of the type:

$$q^{'}(\vec{X}, t) = \hat{q}(X_2; t) \exp(i\kappa_0 X_1), \tag{2.96}$$

where, $q = \{u_i, B_i, p\}$ represents all the perturbation flow field variables. Equations (2.92) to (2.95) can now be written as:

$$i\kappa_0 \hat{u}_1 + \frac{\partial \hat{u}_2}{\partial X_2} - i\kappa_0 S^* \hat{u}_2 = 0; i\kappa_0 \hat{B}_1 + \frac{\partial \hat{B}_2}{\partial X_2} - i\kappa_0 S^* \hat{B}_2 = 0, \tag{2.97}$$

$$\frac{\partial \hat{u}_1}{\partial t} = -\hat{u}_2 S - \frac{i\kappa_0}{\rho} \hat{p}_t + \frac{i\kappa_0 B_0}{\rho \mu_0} \hat{B}_1, \tag{2.98}$$

$$\frac{\partial \hat{u}_2}{\partial t} = \frac{i\kappa_0 S^*}{\rho} \hat{p}_t - \frac{1}{\rho} \frac{\partial \hat{p}_t}{\partial X_2} + \frac{i\kappa_0 B_0}{\rho \mu_0} \hat{B}_2, \tag{2.99}$$

$$\frac{\partial \hat{B}_1}{\partial t} = \hat{B}_2 S + i\kappa_0 B_0 \hat{u}_1; \qquad \frac{\partial \hat{B}_2}{\partial t} = i\kappa_0 B_0 \hat{u}_2, \tag{2.100}$$

Perturbation velocity and magnetic fields in equations (2.98) - (2.100) are coupled via the last terms on their right hand sides. The degree of magnetic field influence on perturbation stability depends upon the relative importance of the coupling term over hydrodynamic processes. To quantify the relative importance of production and coupling, the perturbation equations must be suitably parameterized. The choice of normalization depends on the strength of magnetic field.

We consider two extreme cases: Strong magnetic field limit and near-hydrodynamic limit.

2.1.2.1 Strong magnetic field limit

In this regime, the magnetic processes are more rapid than fluid processes. We choose the following reference variables:

$$\begin{aligned} L_{ref} = \frac{1}{\kappa_0}; \qquad t_{ref} = \frac{1}{V_A \kappa_0}; \qquad u_{ref} = V_A; \\ B_{ref} = B_0; \qquad p_{ref} = \rho V_A^2. \end{aligned} \tag{2.101}$$

The new dimensionless perturbation equations ($q^*, q = \{u_i, p, B_i\}$) are given by:

$$\begin{aligned} \frac{\partial \hat{u}_1^*}{\partial \tau} &= -\hat{u}_2^* \frac{1}{R_A(x_2)} - i\hat{p}_t^* + i\hat{B}_1^*; \\ \frac{\partial \hat{u}_2^*}{\partial \tau} &= iS^* \hat{p}_t^* - \frac{\partial \hat{p}_t^*}{\partial X_2^*} + i\hat{B}_2^*, \end{aligned} \tag{2.102}$$

$$\frac{\partial \hat{B}_1^*}{\partial \tau} = \hat{B}_2^* \frac{1}{R_A(x_2)} + i\hat{u}_1^*; \qquad \frac{\partial \hat{B}_2^*}{\partial \tau} = i\hat{u}_2^* \tag{2.103}$$

where, the normalized time and shear-to-magnetic time scale ratio are:

$$\tau \equiv V_A \kappa_0 t; \qquad R_A(x_2) \equiv \frac{V_A \kappa_0}{S(x_2)}. \tag{2.104}$$

$R_A(x_2)$ quantifies the local dominance of magnetic field effects over that of shear. In a mixing layer, $R_A(x_2)$ is minimum at the center and increases towards the edges of the free stream. When magnetic field is very strong, it is reasonable to expect that the value of R_A at the centerline, $R_A(x_2 = 0) \sim \mathcal{O}(1)$. Then, $R_A(x_2) \gg 1$ at all other locations. Therefore, production and magnetic production terms in equations (2.102) and (2.103) are less important relative to coupling.

We now investigate kinetic and magnetic energy evolution in this limit. Neglecting the production terms, kinetic and magnetic energy equations are given by:

$$\frac{1}{2}\frac{d\hat{u}_i^* \bar{\hat{u}}_i^*}{d\tau} \approx -Im(\hat{u}_i^* \bar{\hat{B}}_i^*); \qquad \frac{1}{2}\frac{d\hat{B}_i^* \bar{\hat{B}}_i^*}{d\tau} \approx +Im(\hat{u}_i^* \bar{\hat{B}}_i^*), \tag{2.105}$$

where, $\bar{\hat{u}}_i^*, \bar{\hat{B}}_i^*$ are the complex conjugates of normalized velocity and magnetic field amplitudes. The terms on the right hand sides of the above equations are equal in magnitude and opposite in sign implying harmonic exchange between velocity and magnetic fields.

Based on the above analysis, the following inferences can be drawn about the flow field evolution in this regime:

1. Production of perturbation kinetic and magnetic energies is small in comparison to harmonic $\hat{u}_i^* - \hat{B}_i^*$ interactions.

2. The harmonic exchange gives rise to oscillatory, out-of-phase evolution of $\hat{u}_i^*$ and $\hat{B}_i^*$ about zero.

3. This oscillatory evolution of $\hat{u}_2^*$ and $\hat{B}_2^*$ about zero further diminishes the net production of kinetic and magnetic energies. This is due to the fact that production alternates between negative and positive values resulting in very little net growth.

4. Harmonic exchange in the absence of production results in equipartition of kinetic and magnetic energies.

5. The flow field is stable and KH instability is eliminated as the perturbations do not grow (Chandrasekhar, 1961; Lau & Liu, 1980).

To assess energy partition, we define Φ_b as:

$$\Phi_b \equiv \frac{b}{k+b}, \tag{2.106}$$

where, k, b are volume-averaged perturbation kinetic and magnetic energies. The behavior of Φ_b will be examined using numerical simulations.

2.1.2.2 *Near hydrodynamic limit*

In this limit, we choose hydrodynamic field values for normalization:

$$\begin{aligned} L_{ref} = \delta_\omega \equiv \frac{\Delta U}{S_0}; \qquad t_{ref} = \frac{1}{S_0}; \qquad u_{ref} = \frac{\Delta U}{2}; \\ B_{ref} = B_0; \qquad p_{ref} = \rho \Delta U^2, \end{aligned} \tag{2.107}$$

where, δ_ω is the vorticity thickness (Sandham & Reynolds, 1991) of a mixing layer and S_0 is the centerline mean flow shear. The dimensionless forms for the perturbation equations are:

$$\begin{aligned} \frac{\partial \hat{u}_1^*}{\partial \tau} &= -\hat{u}_2^* \frac{S}{S_0} - 2i\kappa_0 \delta_\omega \hat{p}_t^* + iR_{A0} M_A \hat{B}_1^*; \\ \frac{\partial \hat{u}_2^*}{\partial \tau} &= 2i\kappa_0 \delta_\omega S^* \hat{p}_t^* - 2\frac{\partial \hat{p}_t^*}{\partial X_2^*} + iR_{A0} M_A \hat{B}_2^*, \end{aligned} \tag{2.108}$$

$$\frac{\partial \hat{B}_1^*}{\partial \tau} = \hat{B}_2^* \frac{S}{S_0} + i\frac{R_{A0}}{M_A} \hat{u}_1^*; \qquad \frac{\partial \hat{B}_2^*}{\partial \tau} = i\frac{R_{A0}}{M_A} \hat{u}_2^* \tag{2.109}$$

$$\tau \equiv S_0 t; \qquad R_{A0} \equiv R_A(x_2 = 0); \quad M_A \equiv \frac{V_A}{\Delta U/2}, \tag{2.110}$$

where, τ is the new normalized time, R_{A0} is the ratio of centerline shear-to-magnetic time scales and M_A is the convective Alfvén Mach number. We now investigate the parameters that describe the development of perturbations in this regime:

1. *The ratio of mixing layer thickness to perturbation wavelength,* $\kappa_0 \delta_\omega$: This is the only stabilizing parameter of relevance in incompressible hydrodynamic mixing layers. It is shown in previous studies that flow is stable to KH instability for $\kappa_0 \delta_\omega > 1$, implying that it is a long wavelength instability Michalke (1964); Ong & Roderick (1972).

2. *Convective Alfvén Mach number,* M_A: This global parameter is the overall ratio of inertial forces to magnetic forces in the MHD flow field.

3. *Centerline shear-to-magnetic time scale ratio,* R_{A0}: R_{A0} describes the relative importance of hydrodynamic production over velocity-magnetic field interaction.

Of the above three parameters, only two are independent, i.e.,

$$R_{A0} = \frac{1}{2} M_A \kappa_0 \delta_\omega, \tag{2.111}$$

In this study, we examine the effect of R_{A0} for a given $\kappa_0 \delta_\omega \sim \mathcal{O}(10^{-1})$. This large wavelength ensures that the underlying hydrodynamic mixing layer is inherently unstable to KH perturbations.

Summary of linear analysis findings. The stability characteristics of MHD mixing layers depend upon the relative importance of hydrodynamic production over the velocity-magnetic field coupling. If hydrodynamic production dominates ($R_{A0} \ll 1$), one can expect behavior akin to the classical KH instability. On the other hand, when the interaction term is completely dominant ($M_A > 1; R_{A0} > 1$), the MHD mixing layer will be linearly stable as seen earlier. For other R_{A0} cases, the degree of stabilization will be dictated by the local prominence of the velocity-magnetic coupling effect. Examination of equations (2.102) and (2.104) reveals the following:

1. For a given R_{A0} or M_A, the magnetic field influence increases with increasing x_2. Thus, even if the centerline of a mixing layer is unstable, the magnetic field can have a stabilizing influence in the outer regions of the flow. The higher the R_{A0}, the smaller is the central region of instability.

2. At a given location x_2 in the mixing layer, the onset and timescale of velocity-magnetic field interaction decrease with increasing R_{A0}.

2.2 Analysis of compressible MHD equations

In this section, the agencies of energy interactions between velocity, magnetic and pressure fields are first presented. Then the equations are simplified in the linear limit to examine the linear agencies of exchange and their dependence on shear, magnetic and acoustic timescales.

2.2.1 Energy analysis

For the sake of assessing the energy exchanges between pressure, velocity and magnetic fields, we consider the individual evolution equations of internal, kinetic and magnetic energies. The

internal energy equation is given by:

$$\frac{\partial}{\partial t}\left(\frac{p}{\gamma-1}\right)+\frac{\partial}{\partial x_j}\left(\frac{pu_j}{\gamma-1}-\kappa\frac{\partial T}{\partial x_j}-u_i\tau_{ij}\right)=-p\frac{\partial u_i}{\partial x_i}-u_i\frac{\partial \tau_{ij}}{\partial x_j}+\frac{1}{\sigma}j^2. \tag{2.112}$$

Kinetic energy equation is given by:

$$\frac{\partial}{\partial t}\left(\frac{\rho u_i u_i}{2}\right)+\frac{\partial}{\partial x_j}\left(\left(\frac{\rho u_i u_i}{2}+p\right)u_j\right)=p\frac{\partial u_i}{\partial x_i}+u_i\frac{\partial \tau_{ij}}{\partial x_j}+u_i(\vec{j}\times\vec{B})_i. \tag{2.113}$$

Magnetic energy equation is given by:

$$\frac{\partial}{\partial t}\left(\frac{B_iB_i}{2\mu_0}\right)+\frac{\partial}{\partial x_j}\left(\frac{(\vec{E}\times\vec{B})_j}{\mu_0}\right)=-\frac{1}{\sigma}j^2-u_i(\vec{j}\times\vec{B})_i. \tag{2.114}$$

It can be seen that the right hand sides of the above equations sum to zero giving rise to the total energy equation (2.7). Figure 2.3 shows the interactions between internal, kinetic and magnetic energies. Unidirectional interactions are indicated in dashed lines and bi-directional exchanges are shown in solid lines.

Internal-kinetic energy exchange. Kinetic and internal energies exchange energy via the pressure dilatation term, $p\partial u_i/\partial x_i$. This term is non-zero only for compressible flows. There is also a irreversible energy transfer from kinetic to internal energy via viscous stresses, $\tau_{ij}\partial u_i/\partial x_j$. This term results in the viscous dissipation of velocity field in both incompressible and compressible regimes.

Kinetic-magnetic energy exchange. Velocity and magnetic fields exchange energy via Lorentz work given by $u_i(\vec{j}\times\vec{B})_i$, i.e., the work done by Lorentz force on velocity field. Lorentz work can be simplified as follows:

$$u_i(\vec{j}\times\vec{B})_i=-\frac{1}{\mu_0}\frac{\partial(B_jB_j)}{\partial x_i}u_i+\frac{1}{\mu_0}u_iB_j\frac{\partial B_i}{\partial x_j}=-\frac{1}{\mu_0}\frac{\partial(B_jB_ju_i)}{\partial x_i}+\frac{\partial u_i}{\partial x_i}\frac{B_jB_j}{\mu_0}+\frac{1}{\mu_0}u_iB_j\frac{\partial B_i}{\partial x_j}. \tag{2.115}$$

The above equation shows that Lorentz work comprises of the works done by magnetic pressure,

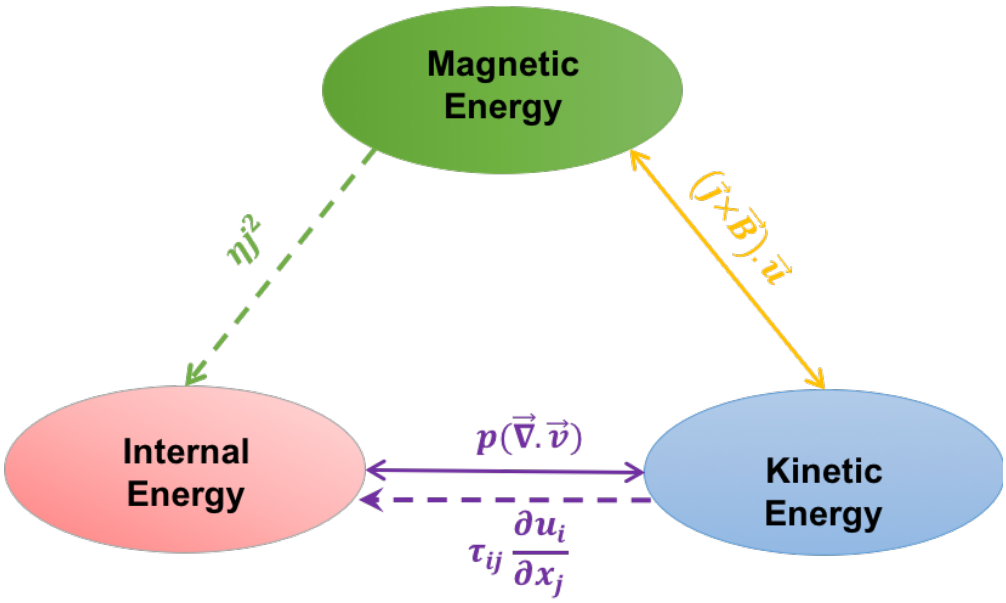

Figure 2.3: Kinetic, internal and magnetic energies in a compressible MHD flow and the agencies of exchange amongst them.

$\frac{\partial(B_jB_j)}{\partial x_i}u_i$, and magnetic tension, $u_iB_j\frac{\partial B_i}{\partial x_j}$. In the incompressible regime, when divergence of velocity is zero, magnetic pressure only acts as a flux term and as a result can only exchange energies at the boundaries. However, in the compressible regime, the magnetic pressure work acts similar to the pressure dilatation term. As a result, dilatational kinetic energy in the compressible regime is shared between internal and magnetic energies. The nature of work done by magnetic tension remains the same in both incompressible and compressible regimes.

Internal-magnetic energy exchange. The dissipative action of resistivity on magnetic field results in the decay of magnetic energy to heat via the Joule heating term given by, $-j^2/\sigma$. As j^2 is always positive, this transfer is unidirectional in all regimes.

2.2.2 Linear analysis of compressible MHD equations

The flow variables of density, velocity, pressure and magnetic field are decomposed into mean and perturbation quantities as follows:

$$q = \overline{q} + q'; \qquad q = \{\rho, \vec{u}, p, \vec{B}\}. \tag{2.116}$$

The governing equations for the mean fields can be written as:

$$\frac{\partial \overline{\rho}}{\partial t} + \overline{u}_i \frac{\partial \overline{\rho}}{\partial x_i} + \overline{\rho} \frac{\partial \overline{u}_i}{\partial x_i} + \frac{\partial}{\partial x_i}\left(\overline{\rho' u_i'}\right) = 0, \tag{2.117}$$

$$\begin{aligned} \frac{\partial \overline{u}_i}{\partial t} + \overline{u}_j \frac{\partial \overline{u}_i}{\partial x_j} + \overline{u_j' \frac{\partial u_i'}{\partial x_j}} = & -\frac{1}{\overline{\rho}} \frac{\partial \overline{p}}{\partial x_i} + \overline{\frac{\rho'}{\overline{\rho}^2} \frac{\partial p'}{\partial x_i}} - \frac{\overline{\rho'^2}}{\overline{\rho}^3} \frac{\partial \overline{p}}{\partial x_i} \\ & - \frac{\partial}{\partial x_i}\left(\frac{\overline{B}_j \overline{B}_j}{2\overline{\rho}\mu_0}\right) - \frac{\partial}{\partial x_i}\left(\frac{\overline{B_j' B_j'}}{2\overline{\rho}\mu_0}\right) \\ & + \frac{\partial}{\partial x_j}\left(\frac{\overline{B}_i \overline{B}_j}{\overline{\rho}\mu_0}\right) + \frac{\partial}{\partial x_j}\left(\frac{\overline{B_i' B_j'}}{\overline{\rho}\mu_0}\right) \end{aligned} \tag{2.118}$$

$$\frac{\partial \overline{p}}{\partial t} + \overline{u}_j \frac{\partial \overline{p}}{\partial x_j} + \overline{u_j' \frac{\partial p'}{\partial x_j}} = -\gamma \overline{p} \frac{\partial \overline{u}_j}{\partial x_j} - \gamma \overline{p' \frac{\partial u_j'}{\partial x_j}}, \tag{2.119}$$

$$\frac{\partial \overline{B}_i}{\partial t} + \overline{u}_j \frac{\partial \overline{B}_i}{\partial x_j} + \overline{u_j' \frac{\partial B_i'}{\partial x_j}} = \overline{B}_j \frac{\partial \overline{u}_i}{\partial x_j} + \overline{B_j' \frac{\partial u_i'}{\partial x_j}} - \overline{B}_i \frac{\partial \overline{u}_j}{\partial x_j} - \overline{B_i' \frac{\partial u_j'}{\partial x_j}}. \tag{2.120}$$

In the linear limit, the above equations can be simplified as:

$$\frac{\partial \overline{\rho}}{\partial t} + \overline{u}_i \frac{\partial \overline{\rho}}{\partial x_i} + \overline{\rho} \frac{\partial \overline{u}_i}{\partial x_i} = 0, \tag{2.121}$$

$$\frac{\partial \overline{u}_i}{\partial t} + \overline{u}_j \frac{\partial \overline{u}_i}{\partial x_j} = -\frac{1}{\overline{\rho}} \frac{\partial \overline{p}}{\partial x_i} - \frac{\partial}{\partial x_i}\left(\frac{\overline{B}_j \overline{B}_j}{2\mu_0}\right) + \frac{\partial}{\partial x_j}\left(\frac{\overline{B}_i \overline{B}_j}{\mu_0}\right) \tag{2.122}$$

$$\frac{\partial \overline{p}}{\partial t} + \overline{u}_j \frac{\partial \overline{p}}{\partial x_j} = -\gamma \overline{p} \frac{\partial \overline{u}_j}{\partial x_j}, \tag{2.123}$$

$$\frac{\partial \overline{B}_i}{\partial t} + \overline{u}_j \frac{\partial \overline{B}_i}{\partial x_j} = \overline{B}_j \frac{\partial \overline{u}_i}{\partial x_j} - \overline{B}_i \frac{\partial \overline{u}_j}{\partial x_j}. \tag{2.124}$$

Equations for perturbations in the linear limit can be obtained by subtracting the mean equations (2.121) - (2.124) from the total field equations (2.1) - (2.7) by neglecting terms of order higher than $\mathcal{O}(q')$. These equations take the form:

$$\frac{\partial \rho'}{\partial t} + \overline{u}_i \frac{\partial \rho'}{\partial x_i} + \overline{\rho} \frac{\partial u_i'}{\partial x_i} = 0, \tag{2.125}$$

$$\frac{\partial u_i'}{\partial t} + \overline{u}_j \frac{\partial u_i'}{\partial x_j} + u_j' \frac{\partial \overline{u}_i}{\partial x_j} = -\frac{1}{\overline{\rho}} \frac{\partial p'}{\partial x_i} + \frac{\rho'}{\overline{\rho}^2} \frac{\partial \overline{p}}{\partial x_i} - \frac{\partial}{\partial x_i} \left(\frac{\overline{B}_j B_j'}{\overline{\rho} \mu_0} \right) + \overline{B}_j \frac{\partial}{\partial x_j} \left(\frac{B_i'}{\overline{\rho} \mu_0} \right) + B_j' \frac{\partial}{\partial x_j} \left(\frac{\overline{B}_i}{\overline{\rho} \mu_0} \right) \tag{2.126}$$

$$\frac{\partial p'}{\partial t} + \overline{u}_j \frac{\partial p'}{\partial x_j} + u_j' \frac{\partial \overline{p}}{\partial x_j} = -\gamma \overline{p} \frac{\partial u_j'}{\partial x_j} - \gamma p' \frac{\partial \overline{u}_j}{\partial x_j} \tag{2.127}$$

$$\frac{\partial B_i'}{\partial t} + \overline{u}_j \frac{\partial B_i'}{\partial x_j} + u_j' \frac{\partial \overline{B}_i}{\partial x_j} = \overline{B}_j \frac{\partial u_i'}{\partial x_j} + B_j' \frac{\partial \overline{u}_i}{\partial x_j} - \overline{B}_i \frac{\partial u_j'}{\partial x_j} - B_i' \frac{\partial \overline{u}_j}{\partial x_j} \tag{2.128}$$

For the sake of analysis, initial density and pressure are considered to be uniform throughout the domain. The mean velocity field is taken to oriented along 1-direction with variation along 2-direction as shown in figure 1.2. The mean magnetic field is oriented along the 1-direction and is uniform throughout the domain.

$$\overline{u}_i = (U_1(x_2), 0, 0); \overline{B}_i = (B_0, 0, 0). \tag{2.129}$$

The mean field equations then reduce to:

$$\overline{\rho}(x_i, t) = \overline{\rho}(x_i, 0); \overline{p}(x_i, t) = \overline{p}(x_i, 0) \tag{2.130}$$

The perturbation equations simplify as follows:

$$\frac{\partial \rho'}{\partial t} + U_1(x_2) \frac{\partial \rho'}{\partial x_1} + \overline{\rho} \frac{\partial u_i'}{\partial x_i} = 0, \tag{2.131}$$

$$\frac{\partial u_i'}{\partial t} + U_1(x_2) \frac{\partial u_i'}{\partial x_1} + u_2' \frac{dU_1}{dx_2} \delta_{i1} = -\frac{1}{\overline{\rho}} \frac{\partial p'}{\partial x_i} - \frac{\partial}{\partial x_i} \left(\frac{B_0 B_1'}{\overline{\rho} \mu_0} \right) + B_0 \frac{\partial}{\partial x_1} \left(\frac{B_i'}{\overline{\rho} \mu_0} \right) \tag{2.132}$$

$$\frac{\partial p'}{\partial t} + U_1(x_2) \frac{\partial p'}{\partial x_1} = -\gamma \overline{p} \frac{\partial u_j'}{\partial x_j} \tag{2.133}$$

$$\frac{\partial B_i'}{\partial t} + U_1(x_2) \frac{\partial B_i'}{\partial x_1} = B_0 \frac{\partial u_i'}{\partial x_1} + B_2' \frac{dU_1}{dx_2} \delta_{i1} - B_0 \frac{\partial u_j'}{\partial x_j} \delta_{i1} \tag{2.134}$$

On the above perturbation equations, rapid distortion analysis can be performed, similar to section 2.1.1. The resulting equations for Fourier amplitudes for perturbations are given by:

$$\frac{d\hat{\rho}}{dt} + i\kappa_i \overline{\rho}\hat{u}_i = 0, \tag{2.135}$$

$$\frac{d\hat{u}_i}{dt} = -\hat{u}_2 S\delta_{i1} - \frac{i\kappa_i}{\overline{\rho}}\hat{p} - \frac{i\kappa_i B_0}{\overline{\rho}\mu_0}\hat{B}_1 + \frac{i\kappa_1 B_0}{\overline{\rho}\mu_0}\hat{B}_i, \tag{2.136}$$

$$\frac{d\hat{p}}{dt} = -i\gamma\kappa_i \overline{p}\hat{u}_i, \tag{2.137}$$

$$\frac{d\hat{B}_i}{dt} = \hat{B}_2 S\delta_{i1} + i\kappa_1 B_0 \hat{u}_i - i\kappa_j B_0 \hat{u}_j \delta_{i1}. \tag{2.138}$$

The above equations are only valid when the mean flow is homogeneously sheared and the wavenumbers are time-dependent (equation (2.38)). In the analysis of homogeneous shear, magnetic pressure is subsumed into total pressure as it does not actively contribute to any energetic exchange between velocity and magnetic fields. However, for compressible flows, magnetic pressure exchanges energy between velocity and magnetic field via magnetic-pressure-dilatation. Therefore, in the following analysis, the individual effects of fluid and magnetic pressures are investigated. Going forward, we will investigate the behavior of u_2' and magnetic and pressure fields that influence its evolution. The equation for u_2' is given by:

$$\frac{d\hat{u}_2}{dt} = -\frac{i\kappa_2}{\overline{\rho}}\hat{p} - \frac{i\kappa_2 B_0}{\overline{\rho}\mu_0}\hat{B}_1 + \frac{i\kappa_1 B_0}{\overline{\rho}\mu_0}\hat{B}_2. \tag{2.139}$$

u_2' is effected by p', B_2' and B_1'. Differentiating the above $\hat{u}_2$ equation with time,

$$\begin{aligned} \frac{d^2\hat{u}_2}{dt^2} &= -\kappa_2^2 a^2 \hat{u}_2 - \kappa_2^2 V_A^2 \hat{u}_i - \kappa_1^2 V_A^2 \hat{u}_2 + ... \\ &= -\kappa_0^2 S^2 t^2 a^2 \hat{u}_2 - \kappa_0^2 S^2 t^2 V_A^2 \hat{u}_2 - \kappa_1^2 V_A^2 \hat{u}_2 + ... \end{aligned} \tag{2.140}$$

In the above equation, only the wave terms depending on $\hat{u}_2$ are shown. Normalizing time with shear and velocity with maximum perturbation amplitude,

$$\frac{d^2\hat{u}_2}{d\tau^2} = -\frac{\tau^2\cos^2(\beta)}{M_g^2}\hat{u}_2 - R_A^2\tau^2\cos^2(\beta)\hat{u}_2 - R_A^2\cos^2(\beta)\hat{u}_2. \tag{2.141}$$

$$R_A \equiv \frac{V_A\kappa_0}{S}; \qquad M_g \equiv \frac{S}{\kappa_0 a}; \qquad a = \sqrt{\frac{\gamma\overline{p}}{\overline{\rho}}}; \qquad \tau = St. \tag{2.142}$$

M_g is the gradient Mach number introduced by Sarkar (1995). It has been established in the previous sections that wave nature of equations giving rise to oscillatory evolution of u_2' stabilizes the shear instabilities. The above wave equation for $\hat{u}_2$ shows that there are three wave-like interactions arising, due to B_1', B_2' and p'. The incompressible coupling term between u_2' and B_2' arising due to magnetic tension remains the same even in the compressible regime. This coupling arises due to the last term on the right hand side of equation (2.141) and the timescale of interaction is time-independent given by $R_A\cos\beta$. The first term on the right hand side of equation (2.141) results coupling between compressible pressure and u_2'. The timescale of interaction increases in time and is given by $\tau\cos(\beta)/M_g$. This has been established in the previous compressible homogeneous shear works of Bertsch *et al.* (2012); Kumar *et al.* (2014). The third wave-like interaction arises due to magnetic pressure and is given by the second term on the right hand side of equation (2.141). The timescale of interaction arising out of magnetic pressure also increases with time and is given by $\tau R_A\cos\beta$. Therefore, the physics in compressible MHD shear flows is not a mere superposition of incompressible MHD shear flows and compressible hydrodynamic shear flows. Additional agencies of interactions between velocity, magnetic and pressure fields is caused by magnetic pressure. These are identified in detail in the linearized energy analysis that follows.

It has been established in the previous section that for the case of incompressible mixing layer that magnetic field is least stabilizing at the location of maximum shear, as $R_A = V_A\kappa/S$. However, $M_g = S/\kappa a$ result in maximum stabilization due to compressibility at the location of maximum shear. Figure 2.4 summarizes the domains of stabilization of compressibility and magnetic field for the case of compressible mixing layer.

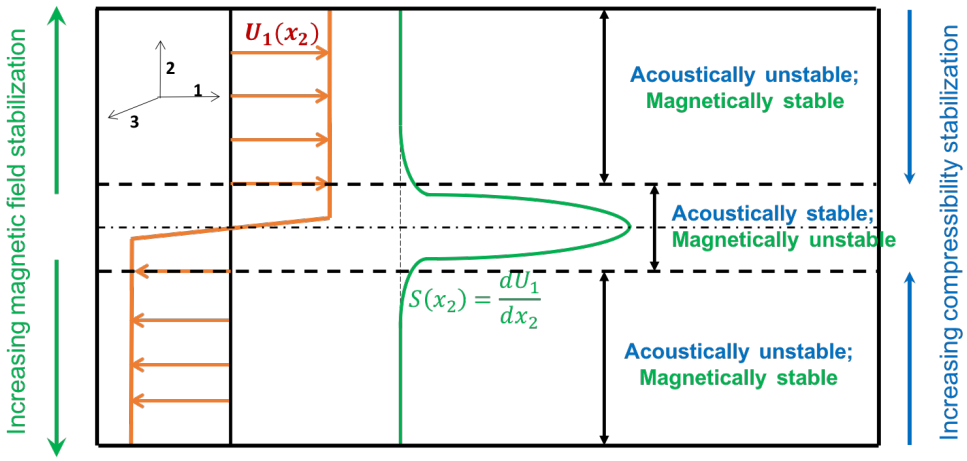

Figure 2.4: Domains of stabilization of compressibility and magnetic field in a mixing layer.

2.2.2.1 *Energy interactions in the linear limit*

The key energy interactions that dictate the stabilizing mechanisms in the linear limit are now investigated. When the streamlines are confined to streamwise-normal plane, the perturbation energy equations for u_2', B_1', B_2' components are given as follows:

$$\frac{\overline{D}\mathcal{K}_2}{\overline{D}t} = \frac{\partial}{\partial t}\left(\frac{\overline{\rho}}{2}\overline{u_2'u_2'}\right) + U_1(x_2)\frac{\partial}{\partial x_1}\left(\frac{\overline{\rho}}{2}\overline{u_2'u_2'}\right) = -\frac{\partial(\overline{p'u_2'})}{\partial x_2} + \overline{p'\frac{\partial u_2'}{\partial x_2}} + B_0\overline{\frac{u_2'}{\mu_0}\frac{\partial B_2'}{\partial x_1}} - B_0\overline{\frac{u_2'}{\mu_0}\frac{\partial B_1'}{\partial x_2}}, \tag{2.143}$$

$$\frac{\overline{D}\mathcal{B}_1}{\overline{D}t} = \frac{\partial}{\partial t}\left(\frac{\overline{B_1'B_1'}}{2\mu_0}\right) + U_1(x_2)\frac{\partial}{\partial x_1}\left(\frac{\overline{B_1'B_1'}}{2\mu_0}\right) = \frac{\overline{B_1'B_2'}}{\mu_0}S - \frac{B_0}{\mu_0}\frac{\partial(\overline{u_2'B_1'})}{\partial x_2} + \frac{B_0}{\mu_0}\overline{u_2'\frac{\partial B_1'}{\partial x_2}}, \tag{2.144}$$

$$\frac{\overline{D}\mathcal{B}_2}{\overline{D}t} = \frac{\partial}{\partial t}\left(\frac{\overline{B_2'B_2'}}{2\mu_0}\right) + U_1(x_2)\frac{\partial}{\partial x_1}\left(\frac{\overline{B_2'B_2'}}{2\mu_0}\right) = \frac{B_0}{\mu_0}\frac{\partial(\overline{u_2'B_2'})}{\partial x_1} - \frac{B_0}{\mu_0}\overline{u_2'\frac{\partial B_2'}{\partial x_1}}, \tag{2.145}$$

$$\frac{\overline{D}\mathcal{P}}{\overline{D}t} = \frac{\partial}{\partial t}\left(\frac{\overline{p'p'}}{2\gamma\overline{p}}\right) + U_1(x_2)\frac{\partial}{\partial x_1}\left(\frac{\overline{p'p'}}{2\gamma\overline{p}}\right) = -\overline{p'\frac{\partial u_k'}{\partial x_k}}. \tag{2.146}$$

Here, $\overline{D}/\overline{D}t$ is the total derivative of the fluid moving with respect to the mean flow. It has been noted in many previous works of homogeneously sheared compressible turbulence that normal

component of velocity fluctuation contributes the most to the dilatation (Bertsch *et al.*, 2012), i.e.,

$$\frac{\partial u_i'}{\partial x_i} \approx \frac{\partial u_2'}{\partial x_2} \Rightarrow \frac{\overline{D}\mathcal{P}}{\overline{D}t} \approx -p'\frac{\partial u_2'}{\partial x_2}. \tag{2.147}$$

Summing the equations for $\mathcal{B}_1$, $\mathcal{B}_2$ and $\mathcal{P}$, we obtain:

$$\begin{aligned}\frac{\overline{D}}{\overline{D}t}\left(\mathcal{B}_1+\mathcal{B}_2+\mathcal{P}\right) = \frac{\overline{B_1'B_2'}}{\mu_0}S - \frac{B_0}{\mu_0}\frac{\partial(\overline{u_2'B_1'})}{\partial x_2} + \frac{B_0}{\mu_0}\frac{\partial(\overline{u_2'B_2'})}{\partial x_1} \\ + \frac{B_0}{\mu_0}\overline{u_2'\frac{\partial B_1'}{\partial x_2}} - \frac{B_0}{\mu_0}\overline{u_2'\frac{\partial B_2'}{\partial x_1}} - \overline{p'\frac{\partial u_2'}{\partial x_2}}.\end{aligned} \tag{2.148}$$

It can be seen that the last three terms on the right hand sides of equations (2.143) and (2.148) are equal in magnitude and opposite in sign indicating harmonic interactions. This implies that in the absence of magnetic stretching production of $\mathcal{B}_1$ and negligible transport, $\mathcal{K}_2$ and $\mathcal{B}_1+\mathcal{B}_2+\mathcal{P}$ may experience equipartition of energy. The extent of energy interactions is examined at various flow and magnetic field regimes using numerical simulations in later chapters of this dissertation.

This chapter enlists the details of the numerical scheme utilized for the direct numerical simulations of magnetohydrodynamic free shear flows. Magneto-gas kinetic method (MGKM) solves the fluid part of the compressible MHD equations using gas kinetic method (GKM) and the magnetic contributions to fluid momentum and energy are added as source terms (Araya *et al.*, 2015). The magnetic field equation is evolved in MGKM using finite difference schemes. In the following sections, we first describe GKM and then present how magnetic field is evolved in MGKM.

3.1 Gas kinetic method

As GKM is a finite volume solver, its formulation can be given as follows:

$$\frac{\partial}{\partial t}\int_{\Omega} \boldsymbol{U} d\mathcal{V} + \int_{\partial\Omega} \boldsymbol{F}\cdot\boldsymbol{dS} = 0. \tag{3.1}$$

Here, $\boldsymbol{U}$ constitutes the conserved variables of mass, momentum and energy in the control volume, Ω, and $\boldsymbol{F}$ contains its fluxes at the boundary of the control volume $\partial\Omega$. The fluxes, $\boldsymbol{F}$ at the boundaries are computed by taking the moments of Boltzmann equation (Xu, 2001). This eliminates the need to specify explicit constitutive relationships for viscous and thermal transport. As a result, higher order Burnett and super Burnett effects are included in GKM (Liao *et al.*, 2008).

A concise methodology of GKM is given below. Boltzmann equation in one dimension, governing the evolution of a single particle distribution function, $f(x,u,t)$, is given by:

$$\frac{\partial f}{\partial t} + u\frac{\partial f}{\partial x} + a\frac{\partial f}{\partial u} = \left(\frac{\partial f}{\partial t}\right)_{collisions}. \tag{3.2}$$

Bhatnagar, Gross and Krook (BGK) developed the following model for the collision term on the right hand side of the above equation (Bhatnagar *et al.*, 1954):

$$\left(\frac{\partial f}{\partial t}\right)_{collisions} = \frac{g-f}{\tau}. \tag{3.3}$$

Here, g is the equilibrium distribution function and τ is the collisional relaxation time related to fluid viscosity. Assuming no body forces, the Boltzmann equation employing the BGK model (B-BGK) is given by:

$$\frac{\partial f}{\partial t} + u\frac{\partial f}{\partial x} = \frac{g - f}{\tau}. \tag{3.4}$$

The solution to the above equation at the cell interface, $x_{j+1/2}$, employing method-of-characteristics is given by (Prendergast & Xu, 1993):

$$f_{j+1/2}(t,u) \equiv f(x_{j+1/2},t,u,\xi) = \frac{1}{\tau}\int_0^t g(x',t',u,\xi)e^{\frac{t'-t}{\tau}}dt' + e^{-t/\tau}f_0(x_{j+1/2}-ut). \tag{3.5}$$

Here, ξ represents one of the internal degree of freedoms of the gas, x' is decided by the particle trajectory, $x_{j+1/2}-x' = u(t-t')$ and f_0 is the initial particle distribution function. However in GKM, $f_{j+1/2}$ is not computed explicitly. The fluxes are computed directly by integrating equation (3.5) in velocity space as follows:

$$\boldsymbol{F}_{j+1/2} = \int_{-\infty}^{\infty} u\boldsymbol{\Psi} f_{j+1/2}(t,u)dud\xi; \qquad \boldsymbol{\Psi} \equiv \left[1, u, \frac{1}{2}(u^2+\xi^2)\right]^T. \tag{3.6}$$

Evaluating $F_{j+1/2}$ would imply computing the moments of g and f_0 at the cell interface, $x_{j+1/2}$. In a finite volume formulation, the values of conserved variables are only known at the cell centers. A nonlinear interpolation such as weighted essentially non oscillatory (WENO) scheme must be utilized to compute the moments of g and f_0 at $x_{j+1/2}$. Similar procedure can be applied to obtain fluxes at the interface, $x_{j-1/2}$. Once the fluxes at $x_{j+1/2}$ and $x_{j-1/2}$ are known, the updated values for conserved variables can be given by:

$$\boldsymbol{U}_j^{n+1} = \boldsymbol{U}_j^n - \frac{\Delta t}{\Delta x}\left(\boldsymbol{F}_{j+1/2}^n - \boldsymbol{F}_{j-1/2}^n\right). \tag{3.7}$$

3.2 Magneto gas kinetic method

To the above finite volume formulation of GKM employing fluid equations in conservation form, the contributions of Lorentz force and Joule heating are added as source terms. The resulting formulation for mass, momentum and energy equations is as follows:

$$\frac{\partial \rho}{\partial t} + \vec{\nabla} \cdot (\rho \vec{V}) = 0, \tag{3.8}$$

$$\frac{\partial \rho \vec{V}}{\partial t} + \vec{\nabla} \cdot (\rho \vec{V}\vec{V} + p\vec{\vec{I}} + \vec{\vec{\tau}}) = \left(\frac{\vec{\nabla} \times \vec{B}}{\mu_0} \right) \times \vec{B}, \tag{3.9}$$

$$\frac{\partial E_h}{\partial t} + \vec{\nabla} \cdot \left((E_h + p)\vec{V} - \kappa \vec{\nabla} T + \vec{V} \cdot \vec{\vec{\tau}} \right) = \frac{\vec{\nabla} \times \vec{B}}{\mu_0} \cdot \left(\frac{\vec{\nabla} \times \vec{B}}{\mu_0 \sigma} - \vec{V} \times \vec{B} \right). \tag{3.10}$$

Magnetic field evolution equation, given by Ohm's law:

$$\frac{\partial \vec{B}}{\partial t} = \vec{\nabla} \times \left(\vec{V} \times \vec{B} - \frac{\vec{\nabla} \times \vec{B}}{\sigma \mu_0} \right), \tag{3.11}$$

is evolved using finite difference schemes. Finite differences are also used to compute the derivatives in the expressions for Lorentz force and Joule heating. In plasma propulsion applications, magnetic field is applied at all times in order to generate thrust. To incorporate this, the magnetic field in MGKM is decomposed into applied and induced components, i.e.,

$$\vec{B} = \vec{B}_A + \vec{B}_I. \tag{3.12}$$

The contributions of both $\vec{B}_A$ and $\vec{B}_I$ are considered in the right hand sides of equations (3.9) - (3.11). However, $\vec{B}_A$ does not change with time, only evolution of $\vec{B}_I$ is considered.

Validation: GKM has been validated for a variety of incompressible and compressible turbulent flows (Kerimo & Girimaji, 2007; Kumar *et al.*, 2013, 2014; Karimi & Girimaji, 2016). A validation study for MGKM is performed in Araya *et al.* (2015).

4. PERTURBATION EVOLUTION IN INCOMPRESSIBLE HOMOGENEOUSLY SHEARED MAGNETOHYDRODYNAMIC FLOWS[1]

The aim of this chapter is to confirm the findings of linear analysis performed in Section 2.1.1 and establish the dominant fluid and magnetic processes at different shear-to-magnetic timescales (R_A).

4.1 Numerical setup

The schematic of the background velocity and magnetic fields with perturbations is shown in figure 2.1a. Periodic boundary conditions are applied in streamwise and spanwise directions. For boundaries in normal direction, shear periodic boundary conditions are applied (Baron, 1982).

$$\phi(t, x + m_1 L_1, y + m_2 L_2, z + m_3 L_3) = \phi(t, x - S m_2 L_2 t, y, z) \tag{4.1}$$

where, L_2 is the length of the domain in the normal direction and m_1, m_2, m_3 are integers.

Simulations are performed for different shear-to-magnetic timescales (R_A). Table 4.1 lists the details of various simulations. As $u_2^{'}$ is most critical for the development of fluid instabilities, only these perturbations are considered in the initial conditions.

$$u_1^{'}(0) = 0; \qquad u_2^{'}(0) = \sin(\kappa_1 x_1 + \kappa_3 x_3); \qquad u_3^{'}(0) = 0 \tag{4.2a}$$

$$B_1^{'}(0) = 0; \qquad B_2^{'}(0) = 0; \qquad B_3^{'}(0) = 0 \tag{4.2b}$$

where, κ_1 and κ_3 are integers. κ_1 and κ_3 are modified such that the perturbation wavevector orientations vary from streamwise to spanwise directions, i.e., $\beta \in [0^\circ, 90^\circ]$. Reynolds numbers, fluid and magnetic ($Re = S/\nu\kappa^2, Re_m = S/\eta\kappa^2$) and β values considered in different simulations are shown in Table 4.1. Since, MGKM is a compressible flow solver, we choose low gradient

[1]Reprinted with permission from Divya Sri Praturi, Diane Collard and Sharath S. Girimaji. The effect of magnetic field on perturbation evolution in homogeneously sheared flows. Journal of Fluid Mechanics (in production). Copyright [2018] by Cambridge University Press.

β	M_g	R_A	Re	Re_m	Grid size
90°	0.005	0.17,1.7, 17	770	195	128^3
0°	0.005	0.39	100000	100000	$128^2 \times 4, 256^2 \times 4$
26°	0.02	0.39	100000	100000	$128^3, 256^3$
63°	0.03	0.39	100000	100000	$128^3, 256^2 \times 128$
0°	0.005	1.7	770	195	128^3
0°	0.005	17	770	195	128^3
$26^\circ, 63^\circ$	0.002	3.9, 39	154	39	128^3

Table 4.1: Incompressible homogeneous shear: Simulation parameters. Reprinted with permission from Praturi *et al.* (in production).

Mach numbers, $M_g \equiv S/\kappa a \leq 0.03$, to emulate incompressible limit. Grid sensitivity study is performed for the case of $\beta = 0^\circ$ in the low $R_A(= 0.39)$ limit. Figure 4.1 shows that $128 \times 128 \times 4$ and $256 \times 256 \times 4$ give nearly identical results except for a higher numerical dissipation in the low resolution simulation. As the evolution of long wavelength perturbations is of current interest, the grid resolution requirements are much less stringent than turbulent flows. The smallest energetic wavelength encountered at the end of the run is of the order of domain size. Thus, the grid resolution employed in the simulation is quite adequate. Nonlinear breakdown and transition to turbulence would require much finer grids and such investigation is currently underway. The analytical results derived in Section 2.1.1 would validate the implementation of shear periodic boundary conditions into MGKM for future nonlinear studies.

In addition to DNS, the RDT equations (2.42), (2.43) are evolved temporally using fourth order Runge-Kutta method. To contrast the MHD flow evolution against hydrodynamic flows, $R_A = 0$ cases are also considered. Analytical results and numerical solutions from RDT and DNS are compared in the next section.

4.2 Results

We now present simulation results for various cases of R_A and perturbation wavevector orientations. As shown in Table 4.1, for a given value of β different magnetic field strengths are considered to correspond to low, intermediate and high magnetic field effects. We use the notation

introduced in equation (2.50) to refer to different components of normalized kinetic and magnetic energies. Throughout MRDT refers to temporally evolved solution of equations (2.42) and (2.43), where as HRDT refers to the hydrodynamic effect alone. We now present the results of spanwise fluctuations and then for other orientations.

4.2.1 Spanwise perturbations – $\beta = 90°$

This perturbation orientation ($\cos\beta = 0$) represents a special limit as velocity and magnetic fields are decoupled. In addition, the velocity fields are impervious to pressure (equation (2.60)). The evolution of kinetic energy (k) at different magnetic fields is plotted in figure 4.2. It can be seen that k grows quadratically consistent with MRDT and HRDT analytical solution given in equation (2.62), regardless of the magnetic field strength. This confirms that the flow field behaves in accordance to the pressure-released hydrodynamic equations noted in Section 2.1.1.1. For the initial conditions considered, perturbation magnetic energy remains zero at all times, for all background magnetic field strengths.

4.2.2 Perturbations with $\beta \in [0°, 90°)$

The results for low, intermediate and high magnetic field cases are now presented for other wavevector orientations.

4.2.2.1 Low magnetic field regime, $R_A \ll 1$

Linear analysis in Section 2.1.1 suggests a three-stage behavior for $R_A \ll 1$ cases. The different stages are now examined.

Early hydrodynamic behavior ($\tau^* < 1$). Figure 4.3 presents the behavior of k_2 for the case of $R_A = 0.39$ and various β values. The analytical result (equation 2.80) is compared against numerical solutions of MRDT and DNS. The self-similarity of k_2 evolution is clearly evident. Since only k_2 is initialized in DNS and RDT, the dominant processes in this stage are pressure redistribution and production. For $\beta = 0°, 26°$, the action of pressure redistributes k_2 to k_1 and k_3 as seen from the increase in their values in figures 4.4, 4.5. This implies that production of k_1 is negative for $\beta = 0°, 26°$ in the first stage. For $\beta = 63°$, u_1' and u_2' are negatively correlated, as a

result, k_1 increases due to production and pressure redistributes energy from k_1 to k_2 and k_2 to k_3. The evolution of k in figure 4.6 also proves that production is negative for $\beta = 0^\circ, 26^\circ$ and positive for 63°. There is a small amount of energy transfer from velocity field to their respective magnetic field components as evident from b_1, b_2 and b_3 evolution in figures 4.7, 4.8 and 4.9. The linear-inviscid analytical solution for b_2 given in equation (2.82) is compared against DNS and MRDT in figure 4.8 and demonstrates good agreement. Figure 4.10a is a schematic that identifies the various energy exchanges dominant at the early stages. Clearly, the velocity field behavior in this regime is very similar to the hydrodynamic case as evidenced by the negligible transfer of energy to the magnetic field.

Intermediate stage onset of magnetic field effect. For $\tau^* \geq 1$, the magnetic field processes set in. The small amount of energy transfer to b_1 and b_2 in the first stage seeds the growth of perturbation magnetic energy (b) due to magnetic stretching. This growth can be seen from the significant increase of b_1 (figure 4.7) for the case of $\beta = 0^\circ$. The increase cannot solely be attributed to harmonic exchange with k_1, since k_1 values never exceed unity for this case proving that this is a consequence of magnetic stretching. From figure 4.3, k_2 goes to zero faster than the hydrodynamic case as a result of exchange with b_2. At $\tau^* \approx 2$, k_2 goes to zero. Subsequently, k_2 starts growing again due to harmonic exchange with b_2. Similarly, k_1 (figure 4.4) increases for $\beta = 0^\circ, 26^\circ$ and decreases for $\beta = 63^\circ$ due to harmonic exchange with b_1. Harmonic exchange is the only dominant process for the velocity and magnetic field perturbations in the spanwise direction, and the transfer is from k_3 to b_3. The growth of magnetic perturbations along the streamwise direction in this stage is the amplification identified in Chagelishvili *et al.* (1993) and Dimitrov *et al.* (2011). The exchange dynamics of this stage are summarized in figure 4.10b.

Late stage behavior. For times, $\tau^* > 4$, the only dominant linear process is the harmonic exchange between the corresponding velocity and magnetic field components. The oscillations of u_2' and B_2' about zero render the sum of kinetic energy production and magnetic energy stretching production to vanish when integrated over a cycle. The magnetic and kinetic fields harmonically exchange energies with a time period of π/R_A for the case of $\beta = 0^\circ, 26^\circ, 63^\circ$. Slight deviations

from the analytical MRDT solutions are attributed to the numerical dissipation and compressibility effects present in DNS. The presence of numerical dissipation is also evident in the grid independence study demonstrated in figure 4.1. The linear energy interaction processes in this stage of evolution are summarized in figure 4.10c.

Some important observations can be made about the evolution of magnetic energy (b) seen in figure 4.11. For a given R_A, b experiences a self-similar evolution (figure 4.11) in the linear stage at all β in spite of magnetic stretching occurring on the shear (S) timescale. This is due to the fact that b_2 is initially zero in both DNS and RDT. The b_2 responsible for magnetic stretching is generated due to exchange from k_2. Since the transfer from k_2 to b_2 occurs on magnetic ($V_A\kappa_0\cos\beta$) timescale, for a given R_A, b experiences a self-similar evolution for all β in scaled time $\tau^* = \tau\cos\beta$.

4.2.2.2 Intermediate magnetic field regime, $R_A \approx 1$

In this R_A regime, the magnetic field processes respond rapidly to the initial hydrodynamic processes. As a result, the first and second stages seen in $R_A \ll 1$ occur nearly simultaneously. The kinetic and magnetic energies for $R_A = 1.7, \beta = 0^\circ$ are presented in figures 4.12 and 4.13, respectively. During the course of evolution, the magnetic energy (b) exceeds the initial perturbation kinetic energy (k_0) due to magnetic stretching. k_2 is transferred to k_1 due to pressure redistribution. Even though the production of k_1 in this case is negative ($\beta = 0^\circ$), it has negligible influence on the evolution of k due to the oscillatory nature of $u_2^{'}$ seen from the beginning. The kinetic energy (k) becomes zero at $\tau \approx 0.75$ and then increases due to harmonic exchange. An overshoot is seen in k due to harmonic exchange, at the end of first cycle of exchange. After this time, harmonic exchange prevails and the sum of kinetic and magnetic energy production goes to zero.

4.2.2.3 High magnetic field regime, $R_A \gg 1$

In this regime, the magnetic field evolution is rapid enough that all the stages identified in $R_A \ll 1$ occur nearly simultaneously. As seen in Section 2.1.1.2, in the linear limit of this R_A

regime, the evolution of k_2 and b_2 are given by:

$$k_2 = \frac{\cos^2(R_A\tau^*)}{(1+\tau^{*2})} \tag{4.3a}$$

$$b_2 = \frac{\sin^2(R_A\tau^*)}{(1+\tau^{*2})} \tag{4.3b}$$

These equations can be rewritten as follows to obtain a self-similar result in this regime.

$$k_2(1+\tau^{*2}) = \cos^2(R_A\tau^*) = \cos^2(\tau^{**}) \tag{4.4a}$$

$$b_2(1+\tau^{*2}) = \sin^2(R_A\tau^*) = \sin^2(\tau^{**}) \tag{4.4b}$$

where, $\tau^{**} = R_A\tau^*$. Using the above equations, the computed k_2 and b_2 in all cases with $R_A > 2$ are plotted in the timescale τ^{**}. Figures 4.14, 4.15 demonstrate the excellent agreement of the DNS results with linear theory and confirm the self-similar state of k_2 and b_2 in this R_A regime.

Linear analysis also suggests equipartition between perturbation kinetic and magnetic energies in the high R_A limit. In order to understand how the perturbation energies are distributed between magnetic and kinetic components, we define the energy partition function (Φ_b) as follows:

$$\Phi_b = \frac{b}{k+b} \tag{4.5}$$

This definition is similar to that of Sarkar *et al.* (1991) for dilatational kinetic and potential energies. Equipartition would imply that the energy partition function (Φ_b) oscillates about 0.5. In order to verify this, we plot Φ_b from DNS of intermediate and high R_A cases (exchange dominates at all times) for all perturbation orientations, $\beta = 0°, 26°, 63°$. A timescale of $R_A\tau^*$ is chosen so as to demonstrate the self-similar behavior at different β, R_A values. Figure 4.16 verifies that Φ_b oscillates about 0.5 demonstrating equipartition of kinetic and magnetic energies. Another observation consistent with equipartition is that production and magnetic stretching are of comparable magnitudes and opposite in sign with a phase difference of $\pi/2$. This leads to zero net growth of

$k + b$ when integrated over a cycle.

As a result, pressure reorientation and exchange are the only significant processes in this regime. Investigating the sum of kinetic and magnetic energies, i.e., $(k + b)$, $(k_1 + b_1)$, $(k_2 + b_2)$ and $(k_3 + b_3)$, removes the effect of harmonic exchange and highlights the effect of pressure redistribution at different β:

$$\frac{d(k+b)}{d\tau} = -2Re(\hat{u}_2\bar{\hat{u}}_1) + 2Re(\hat{B}_2\bar{\hat{B}}_1) \tag{4.6a}$$

$$\frac{d(k_1+b_1)}{d\tau} = -2Re(\hat{u}_2\bar{\hat{u}}_1)\left(1 - \frac{2\cos^2(\beta)}{1+\cos^2(\beta)\tau^2}\right) + 2Re(\hat{B}_2\bar{\hat{B}}_1) \tag{4.6b}$$

$$\frac{d(k_2+b_2)}{d\tau} = -2Re(\hat{u}_2\bar{\hat{u}}_2)\frac{2\cos^2(\beta)\tau}{1+\cos^2(\beta)\tau^2} \tag{4.6c}$$

$$\frac{d(k_3+b_3)}{d\tau} = 2Re(\hat{u}_2\bar{\hat{u}}_3)\frac{2\cos(\beta)\sin(\beta)}{1+\cos^2(\beta)\tau^2} \tag{4.6d}$$

The case of $R_A = 17, \beta = 0^\circ$ is investigated first. It can be seen from figure 4.17 that the sum of kinetic and magnetic energies $(k + b)$ obtained from DNS remains nearly a constant. For $\beta = 0^\circ$, production is always negative (equation 2.55) and magnetic stretching is always positive (equation 2.57). This implies that the sum of production and stretching becomes negligible due to the rapid oscillatory nature of $u_2^{'}$ and $B_2^{'}$ with a phase difference of $\pi/2$. Overall, energy transfer occurs from $(k_2 + b_2)$ to $(k_1 + b_1)$ due to pressure redistribution. Slight decrease in the value of $(k + b)$ from unity is due to the viscous and resistive effects included in DNS.

We now investigate the evolution of magnetic and kinetic perturbations for the case of $\beta = 26^\circ, R_A = 3.9$. From figure 4.18, it can be seen that the sum of kinetic and magnetic energies decays a little faster than $\beta = 0^\circ, R_A = 17$ since the fluid and magnetic Reynolds numbers are lower. The frequency of oscillation of $u_2^{'}, B_2^{'}$ is lower than that of $\beta = 0^\circ$ case. As a result, the flow experiences longer periods of positive stretching and negative production. This results in larger amplitude oscillations as compared to $\beta = 0^\circ$ case. $(k_2 + b_2)$ loses energy to $(k_1 + b_1)$ and $(k_3 + b_3)$ due to pressure redistribution. $(k_1 + b_1)$ dominates at late times.

For $\beta = 63^\circ, R_A = 3.9$ shown in figure 4.19, the timescale ($\tau^* = \tau\cos(\beta)$) at which exchange between magnetic and kinetic energies occurs is slower than that of $\beta = 26^\circ$ case. This, in addition

to initial positive production and stretching, results in even larger amplitude oscillations in $(k+b)$ compared to $\beta = 0°, 26°$ cases. At late times, however, production becomes negative and stretching becomes positive. So, the sum of production and stretching becomes negligible when integrated over a cycle. At early times, $(k_2 + b_2)$ loses energy to $(k_3 + b_3)$ and gains energy from $(k_1 + b_1)$ due to redistribution. $(k_3 + b_3)$ dominates at late times.

4.2.2.4 Viscous vs. inviscid MRDT

We now compare the evolution of viscous MRDT with that of the inviscid limit. Figure 4.20 shows the evolution of kinetic energy (k) for viscous and inviscid MRDT for $\beta = 0°$ at low and moderate R_A values. Similar Re, Re_m values as the DNS calculations are chosen for viscous MRDT calculations. At low R_A, comparing the behavior of k in the viscous limit, where $Re = Re_m = 10^5$, to that of the inviscid solution, we observe that the two calculations agree well with one another. This implies that for the time ranges investigated in the low R_A regime, there is no considerable effect of viscous and resistive action on the perturbation evolution. For the moderate $R_A(= 1.7)$ case where, $Re = 770$ and $Re_m = 195$, the viscous solution experiences considerable amount of decay. However, for the times $\tau < 3$ presented in the DNS solution (figure 4.12), viscous and inviscid MRDT agree well with one another.

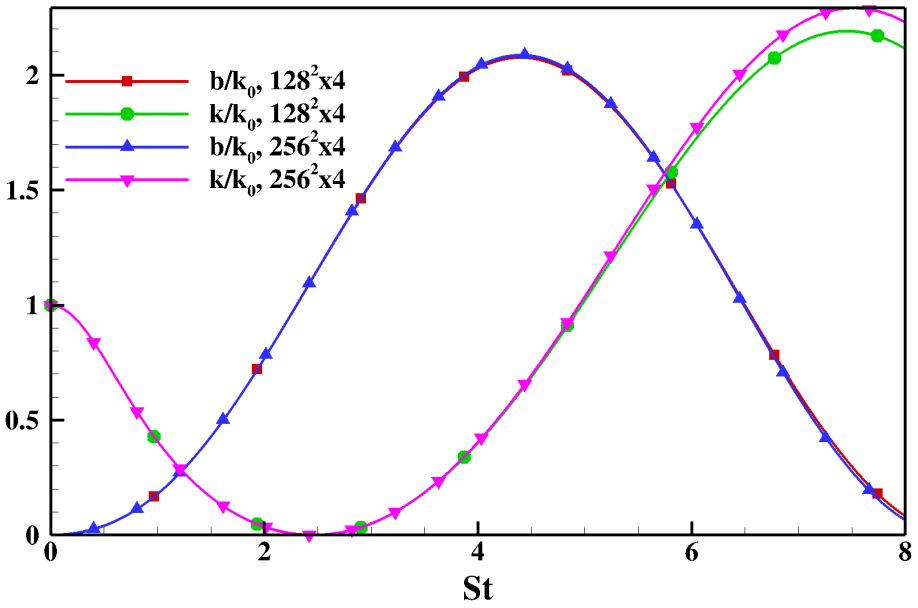

Figure 4.1: Grid independence is shown for $R_A = 0.39, \beta = 0°$. Reprinted with permission from Praturi *et al.* (in production).

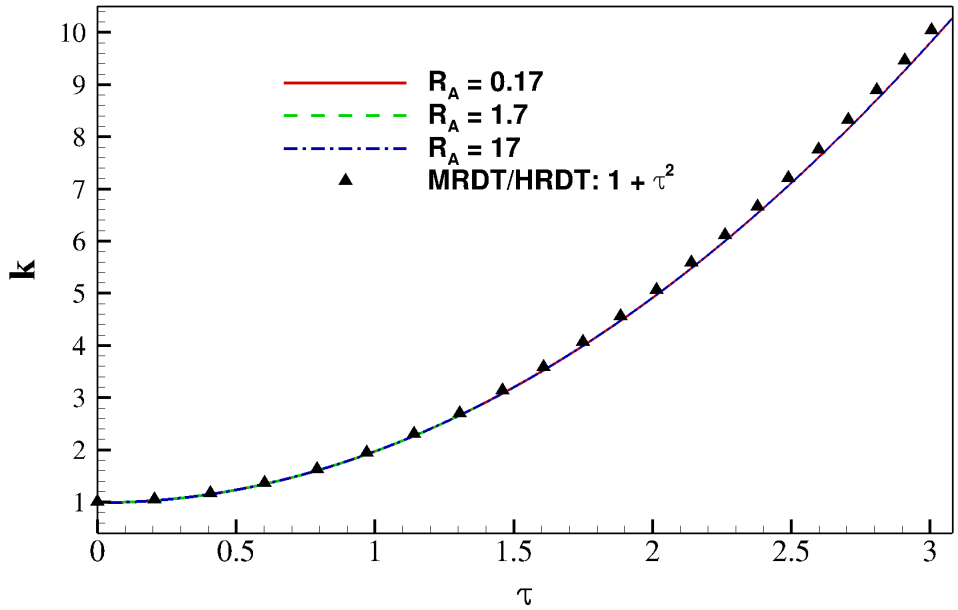

Figure 4.2: Spanwise perturbation: Evolution of kinetic energy, k, of $R_A = 0.17, 1.7, 17$ compared against pressure-released hydrodynamic solution of MRDT: $k = 1+\tau^2$. Reprinted with permission from Praturi *et al.* (in production).

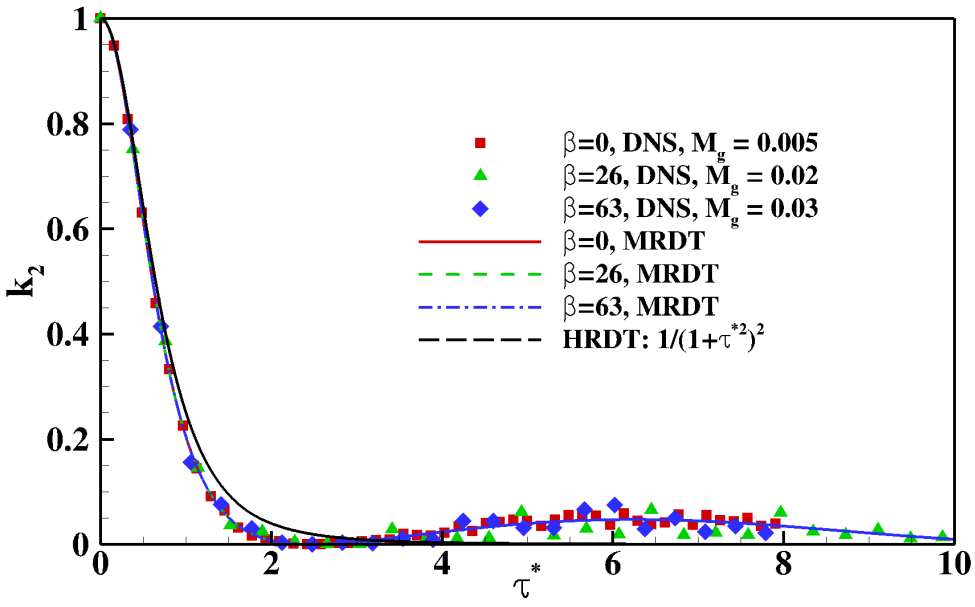

Figure 4.3: Low R_A regime ($R_A = 0.39$): Evolution of k_2 obtained using DNS and MRDT for $\beta = 0°, 26°, 63°$ compared against the analytical solution of HRDT: $k_2 = 1/(1+\tau^{*2})^2$. Reprinted with permission from Praturi *et al.* (in production).

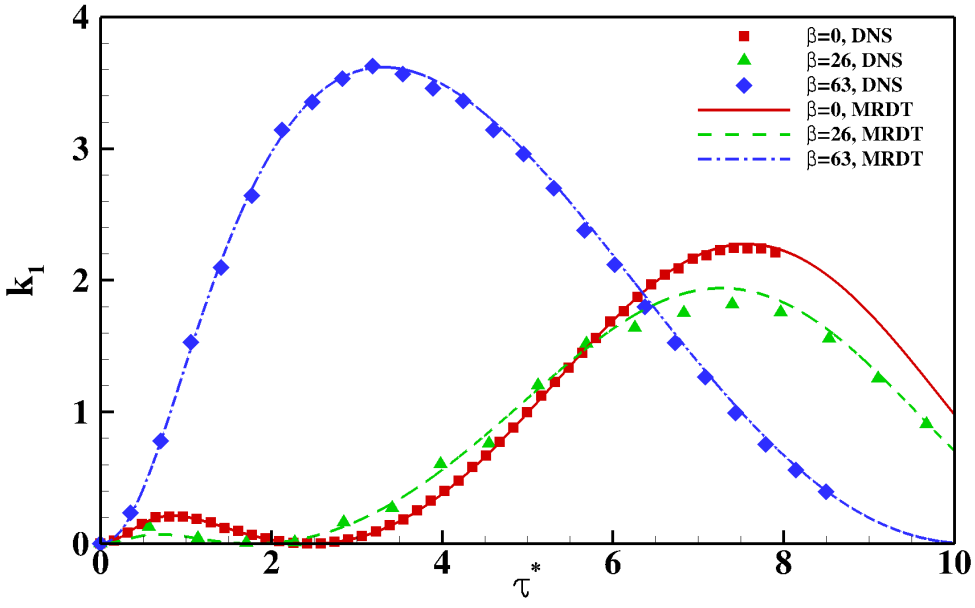

Figure 4.4: Low R_A regime ($R_A = 0.39$): Evolution of k_1 obtained using DNS and MRDT for $\beta = 0°, 26°, 63°$. Reprinted with permission from Praturi *et al.* (in production).

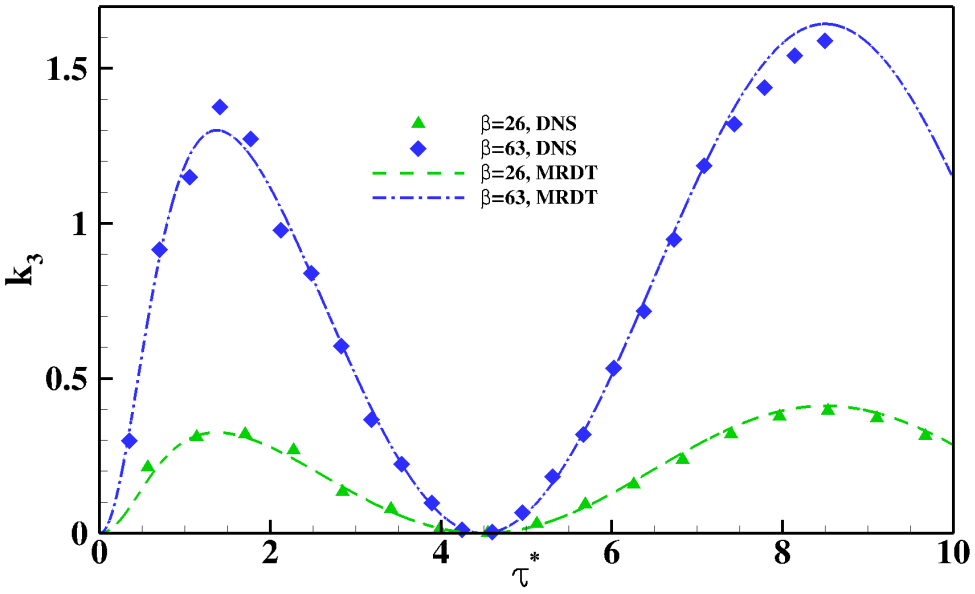

Figure 4.5: Low R_A regime ($R_A = 0.39$): Evolution of k_3 obtained using DNS and MRDT for $\beta = 26°, 63°$. For $\beta = 0°$, $k_3 = 0$ at all times. Reprinted with permission from Praturi *et al.* (in production).

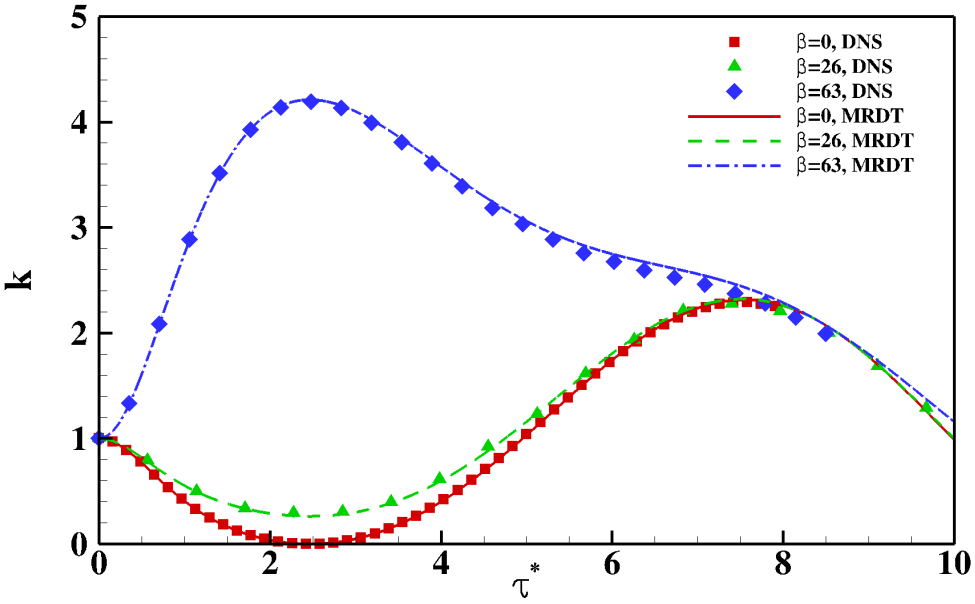

Figure 4.6: Low R_A regime ($R_A = 0.39$): Kinetic energy (k) evolution obtained using DNS and MRDT for $\beta = 0°, 26°, 63°$. Reprinted with permission from Praturi *et al.* (in production).

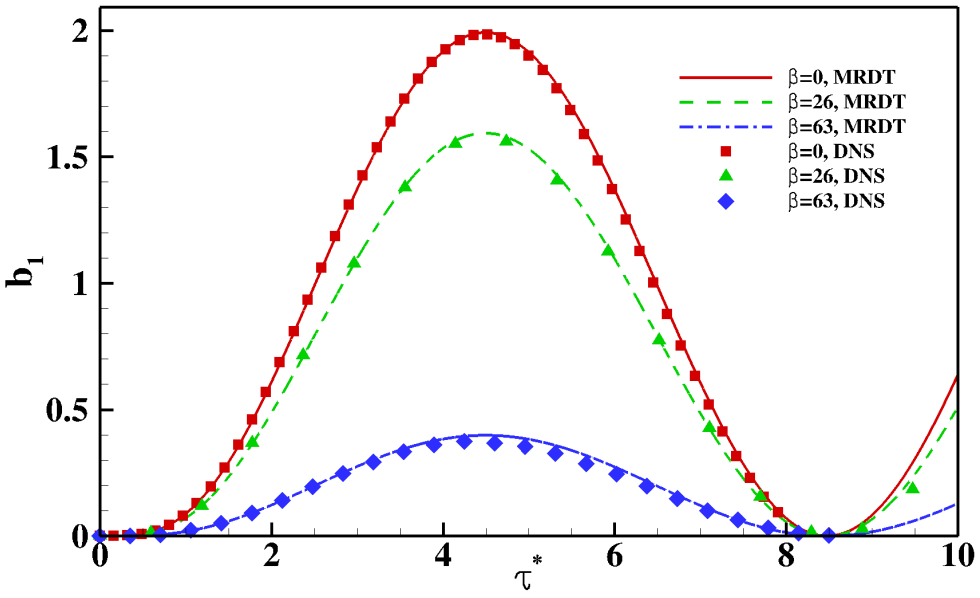

Figure 4.7: Low R_A regime ($R_A = 0.39$): Evolution of b_1 obtained using DNS and MRDT for $\beta = 0°, 26°, 63°$. Reprinted with permission from Praturi *et al.* (in production).

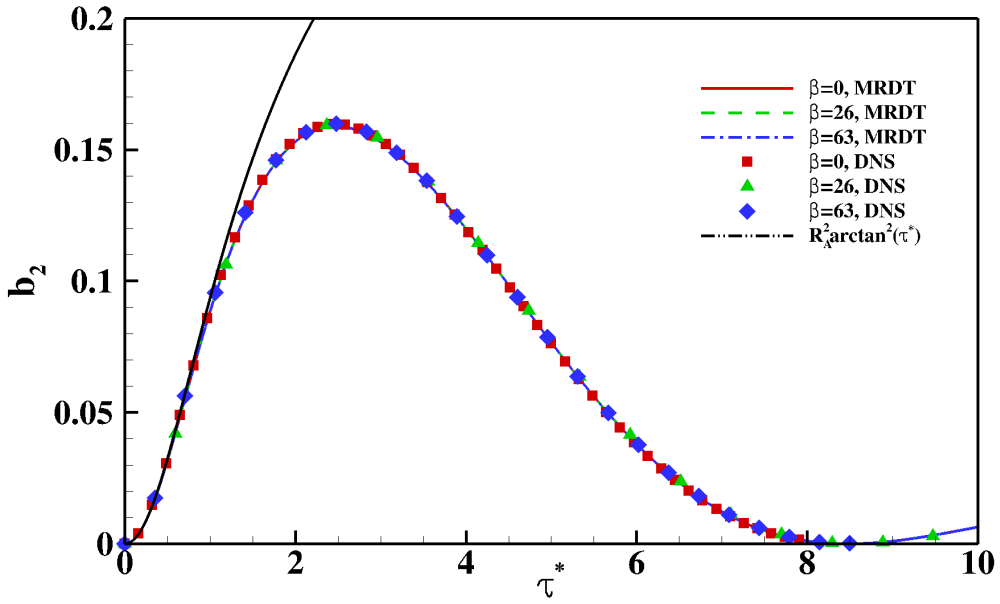

Figure 4.8: Low R_A regime ($R_A = 0.39$): Evolution of b_2 obtained using DNS and MRDT for $\beta = 0°, 26°, 63°$ compared against the analytical solution $b_2 = R_A^2 \arctan^2(\tau^*)$. Reprinted with permission from Praturi *et al.* (in production).

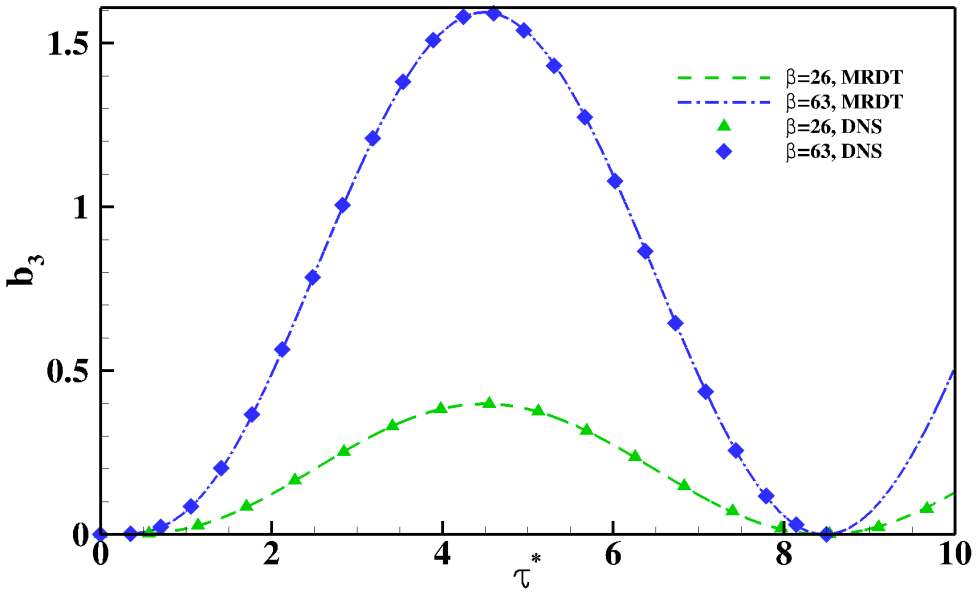

Figure 4.9: Low R_A regime ($R_A = 0.39$): Evolution of b_3 obtained using RDT and DNS for $\beta = 0°, 26°, 63°$. Reprinted with permission from Praturi *et al.* (in production).

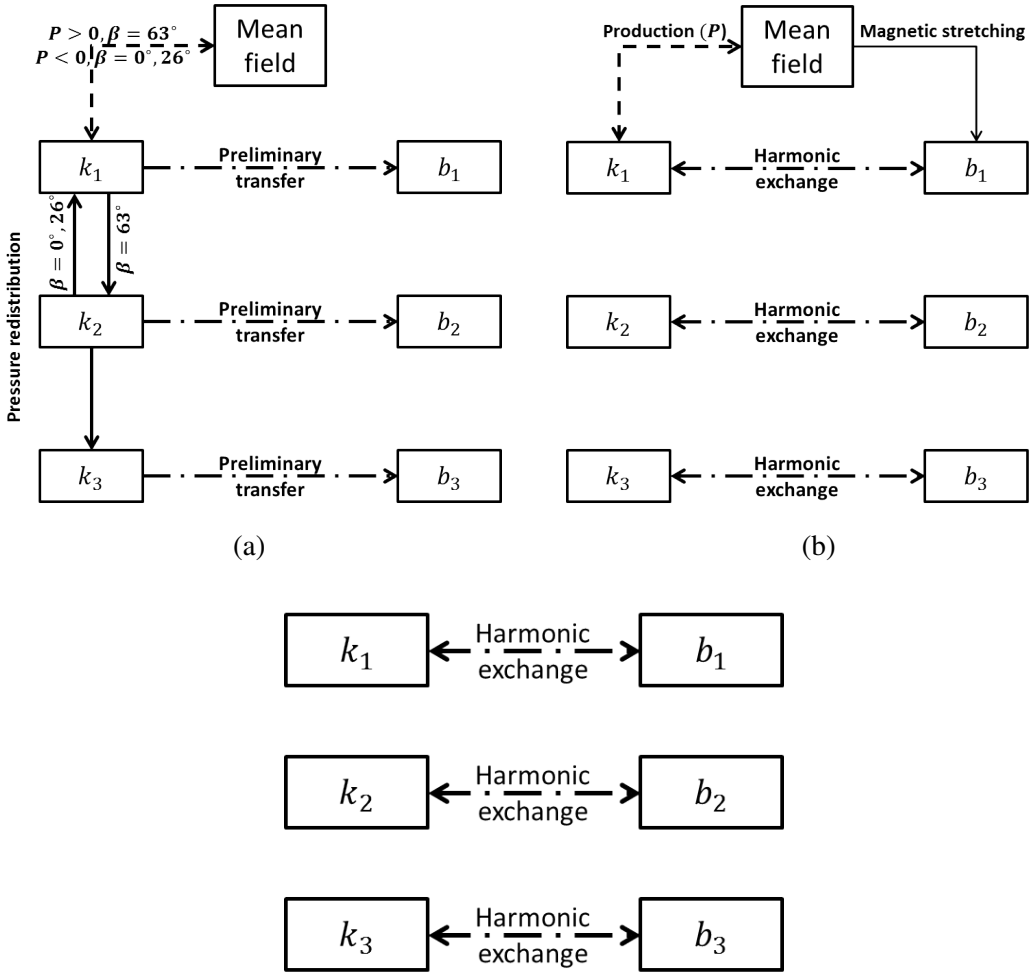

Figure 4.10: Dominant processes in low R_A regime: (a) Stage 1 – Pressure redistribution (solid) and production, P (dashed), (b) Stage 2 – Production, magnetic stretching and harmonic exchange and (c) Stage 3 – Harmonic exchange. Reprinted with permission from Praturi *et al.* (in production).

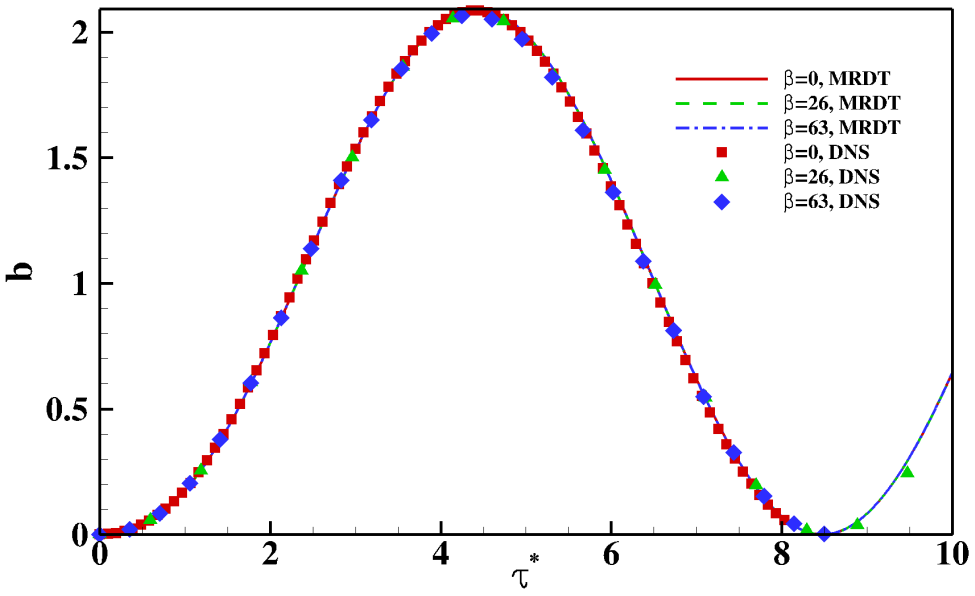

Figure 4.11: Low R_A regime ($R_A = 0.39$): Magnetic energy (b) evolution obtained using DNS and MRDT for $\beta = 0°, 26°, 63°$. Reprinted with permission from Praturi *et al.* (in production).

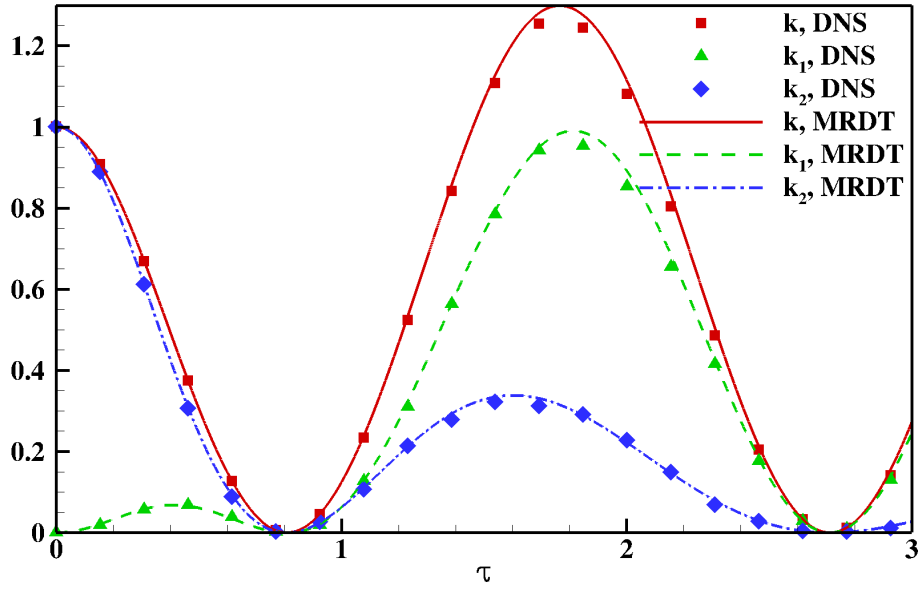

Figure 4.12: Intermediate R_A regime ($R_A = 1.7$): Evolution of kinetic energies (k, k_1, k_2) obtained using DNS and MRDT for $\beta = 0°$. Reprinted with permission from Praturi *et al.* (in production).

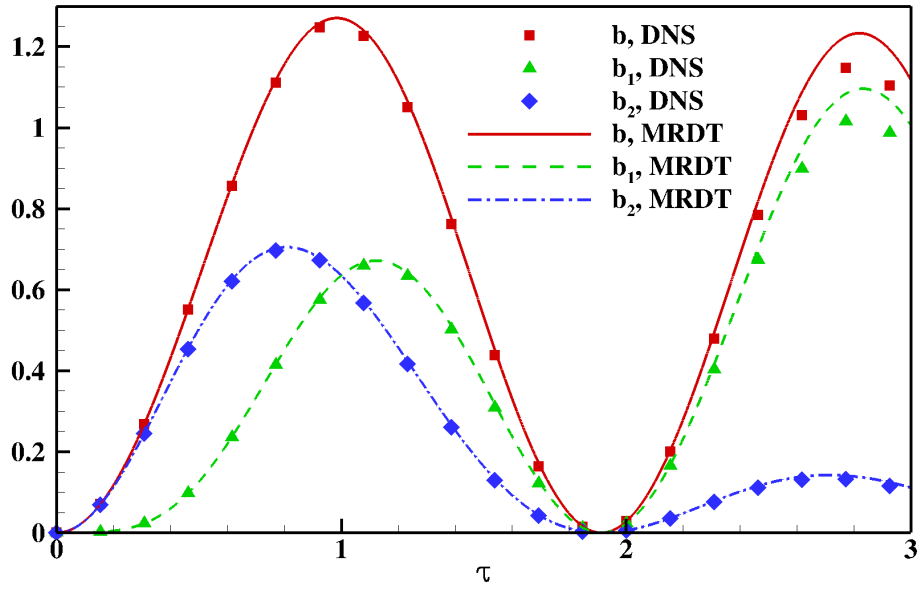

Figure 4.13: Intermediate R_A regime ($R_A = 1.7$): Evolution of magnetic energies (b, b_1, b_2) obtained using DNS and MRDT for $\beta = 0°$. Reprinted with permission from Praturi *et al.* (in production).

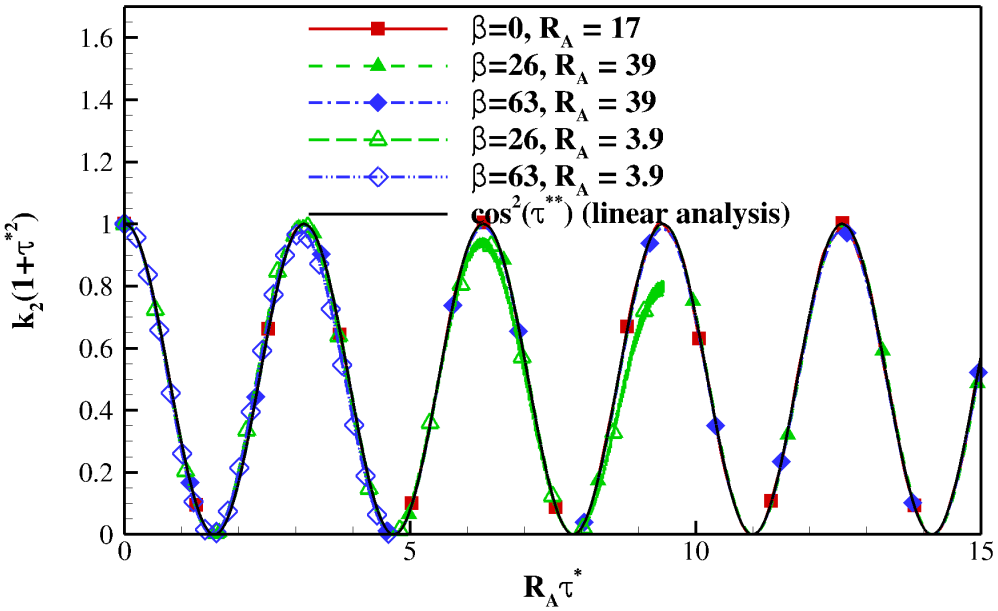

Figure 4.14: High R_A regime: Evolution of k_2 obtained using DNS for $R_A = 3.9, 17, 39; \beta = 0°, 26°, 63°$. The analytical solution of MRDT, $k_2(1+\tau^{*2}) = \cos^2(\tau^{**})$ is also presented. Reprinted with permission from Praturi *et al.* (in production).

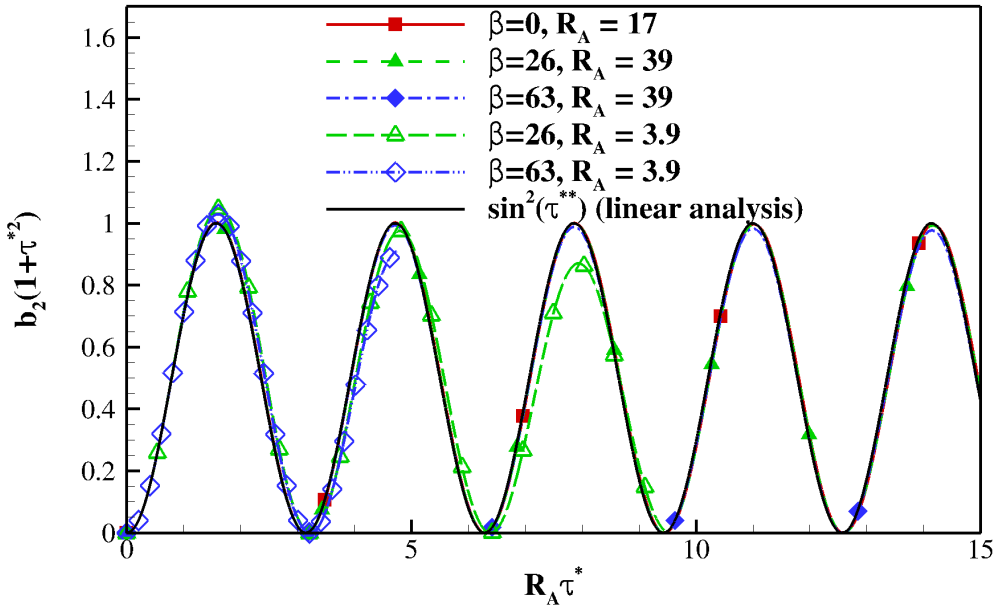

Figure 4.15: High R_A regime: Evolution of b_2 obtained using DNS for $R_A = 3.9, 17, 39; \beta = 0°, 26°, 63°$. The analytical solution of MRDT, $b_2(1+\tau^{*2}) = \sin^2(\tau^{**})$ is also presented. Reprinted with permission from Praturi *et al.* (in production).

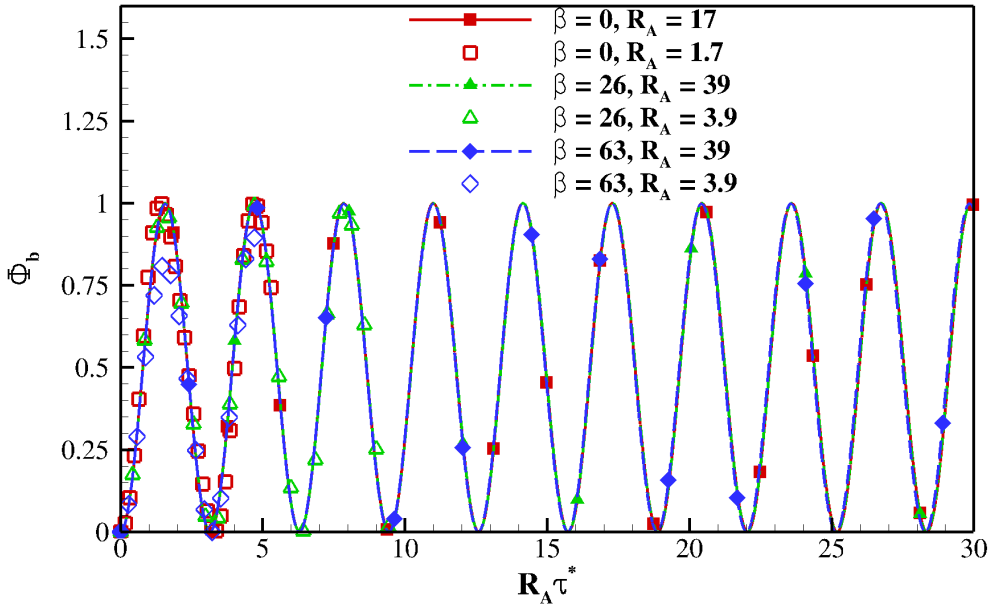

Figure 4.16: Energy partition function (Φ_b) obtained using DNS plotted for $R_A = 1.7, 3.9, 17, 39$; $\beta = 0°, 26°, 63°$. Reprinted with permission from Praturi *et al.* (in production).

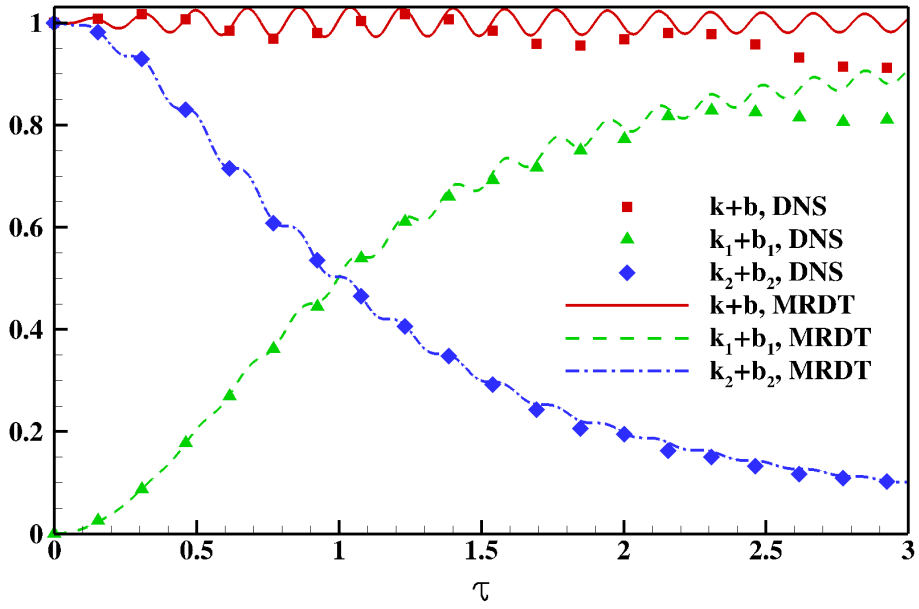

Figure 4.17: High R_A regime ($R_A = 17$): Evolution of the sum of kinetic and magnetic energies $(k + b, k_1 + b_1, k_2 + b_2)$ obtained using DNS and MRDT for $\beta = 0°$. $k_3 + b_3$ is zero at all times. Reprinted with permission from Praturi *et al.* (in production).

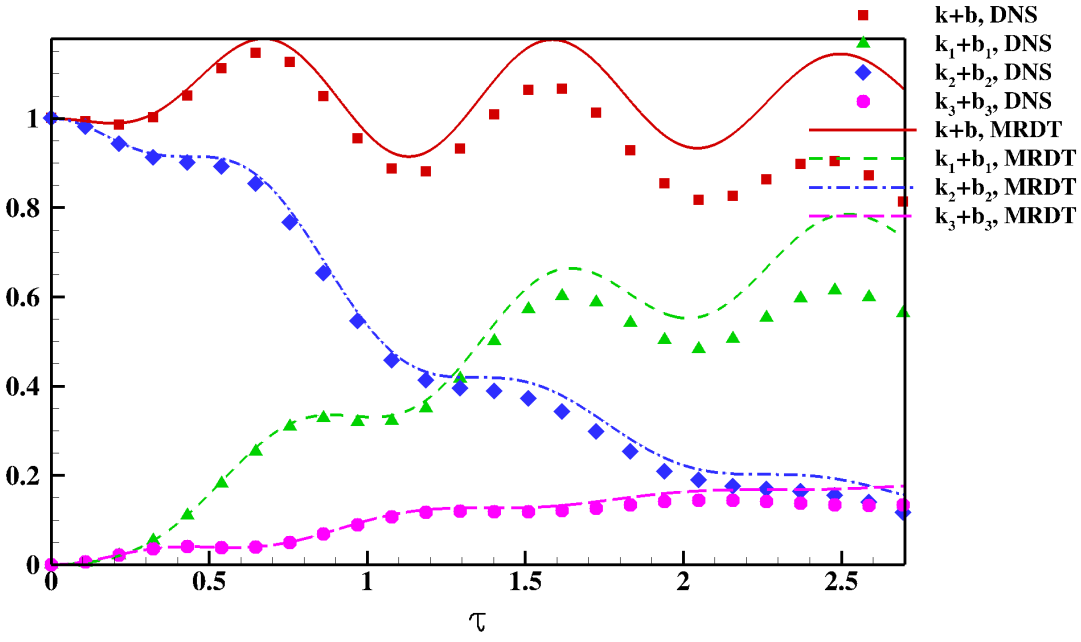

Figure 4.18: High R_A regime ($R_A = 3.9$): Evolution of the sum of kinetic and magnetic energies $(k + b, k_1 + b_1, k_2 + b_2, k_3 + b_3)$ obtained using DNS and MRDT for $\beta = 26°$. Reprinted with permission from Praturi *et al.* (in production).

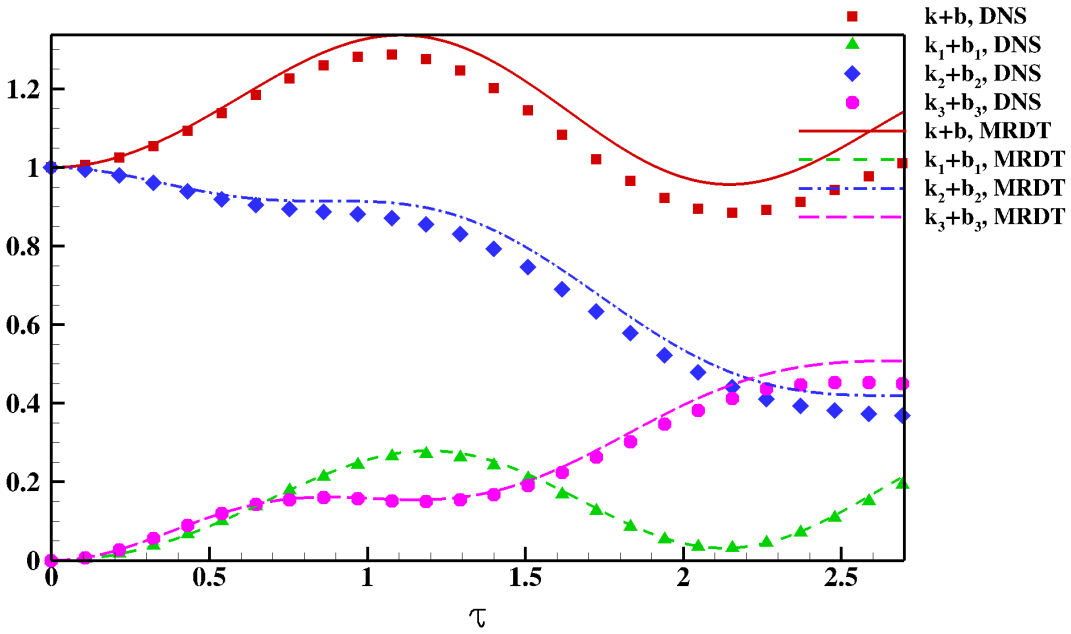

Figure 4.19: High R_A regime ($R_A = 3.9$): Evolution of the sum of kinetic and magnetic energies ($k + b, k_1 + b_1, k_2 + b_2, k_3 + b_3$) obtained using DNS and MRDT for $\beta = 63°$. Reprinted with permission from Praturi *et al.* (in production).

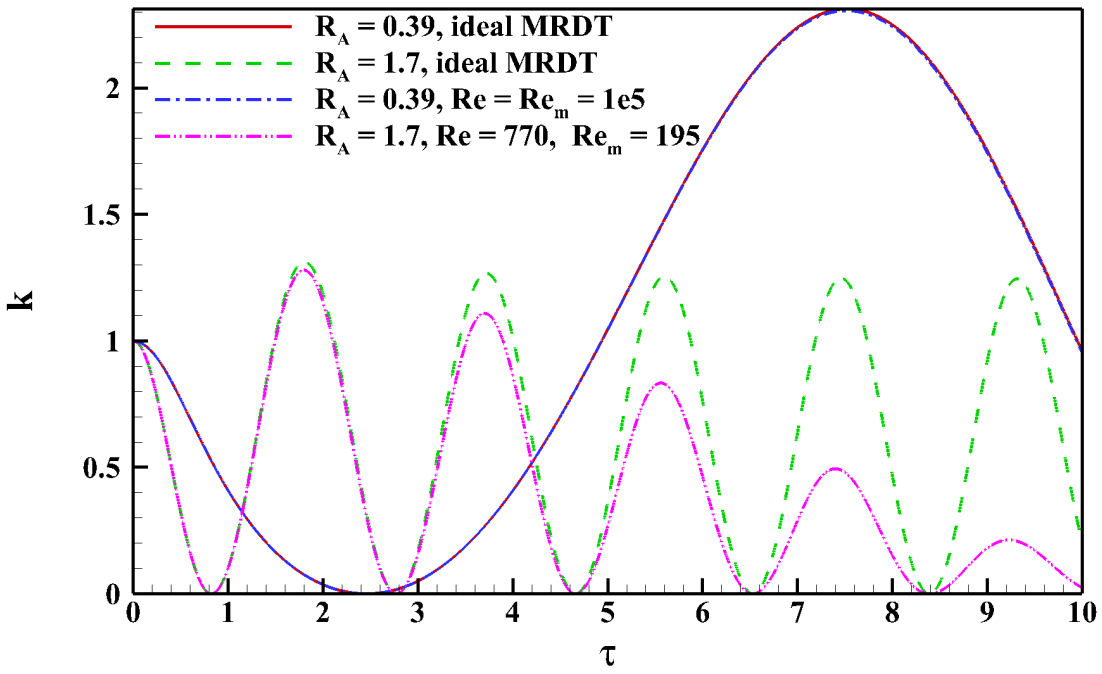

Figure 4.20: Viscous vs. inviscid MRDT ($\beta = 0°$): Kinetic energy (k) in the inviscid limit compared against viscous MRDT at low $R_A = 0.39, Re = Re_m = 10^5$ and moderate $R_A = 1.7, Re = 770, Re_m = 195$. Reprinted with permission from Praturi *et al.* (in production).

5. LINEAR AND NONLINEAR SUPPRESSION MECHANISM OF KELVIN-HELMHOLTZ INSTABILITY IN MAGNETOHYDRODYNAMIC FLOWS

In this chapter, we perform numerical simulations to investigate the linear and nonlinear evolution of KH instability when subjected to a streamwise applied magnetic field. The linear effect of magnetic field on KH instability has been presented in Section 2.1.2. As mentioned in the Introduction, the nonlinear stage of perturbation evolution is disrupted by resistive "tearing" instability when magnetic field is weak. We first present a brief discussion on resistive instability. Thereafter, numerical setup and results are presented.

5.1 Resistive "tearing" instability in nonlinear stage

In general, resistive instabilities act to release accumulated energy in regions of magnetic field inhomogeneity to move to a lower energy state (Goldston & Rutherford, 1995). These inhomogeneities in magnetic field are otherwise stable in ideal MHD fluids (zero resistivity). There are multiple types of manifestation of resistive instability (Furth *et al.*, 1963). In the current problem, the "tearing" mode of resistive instability gives rise to the disruption in the nonlinear regime (Frank *et al.*, 1996; Malagoli *et al.*, 1996; Palotti *et al.*, 2008; Mak *et al.*, 2017). Tearing mode of resistive instability is initiated at the inflection region in the magnetic field resulting in a wave-like breakdown of magnetic field (Goldston & Rutherford, 1995).

Work done by magnetic field on velocity via the Lorentz force is a precursor to resistive instability (Furth *et al.*, 1963). The expression for the work done by Lorentz force, W, can be obtained by taking the dot product of Lorentz force and velocity:

$$W \equiv (\vec{j} \times \vec{B}) \cdot \vec{U} = \frac{1}{\mu_0} \left(\vec{\nabla} \times \vec{B} \times \vec{B} \right) \cdot \vec{U}, \tag{5.1}$$

where, $\vec{U}, \vec{B}$ are total velocity and magnetic fields. If $W > 0$, energy is transferred from magnetic field to velocity and could result in the unbounded growth of kinetic energy. When $W < 0$, energy transfer from velocity field enables the growth of magnetic energy. Since, resistive "tearing"

instability is onset in the nonlinear stage of KH instability, it is not easily amenable to analytical investigation.

We now perform a series of numerical simulations to compare and contrast the sequence of flow and magnetic field events leading to linear stabilization or nonlinear disruption of perturbation evolution in MHD mixing layers.

5.2 Simulation setup

The setup for direct numerical simulations (DNS) is shown in figure 2.2. The simulations are quasi three-dimensional, i.e., we have a nominal number of grid points in the spanwise direction to be able to compute the derivatives. Since we are investigating temporal evolution of mixing layers, periodic boundary conditions are applied at streamwise boundaries. The flow field is also periodic in the spanwise direction. Zero gradient boundary conditions are applied at the normal boundaries.

Background velocity field is given by a hyperbolic tangent mixing layer profile:

$$U_1(x_2) = \frac{U_0}{2} \tanh\left(\frac{2x_2}{\delta_\omega}\right), \tag{5.2}$$

where, δ_ω is the vorticity thickness of the mixing layer. We introduce normal velocity perturbations ($u_2^{'}$) with the wavevector oriented along the streamwise direction (Kumar *et al.*, 2014):

$$u_2^{'}(x_1, x_2, x_3; t) = \{0.01, 0.03\} \times \frac{U_0}{2} \sin\left(\frac{2\pi x_1}{L_1}\right). \tag{5.3}$$

This corresponds to perturbations with amplitudes 1% and 3% of the maximum background velocity. An external magnetic field, B_0, is applied at all times in the streamwise direction as shown in figure 2.2. Tab. 5.1 shows B_0, M_A and R_{A0} values for all the simulations performed. $\kappa_0\delta_\omega$ is held constant at 0.2. Viscosity and resistivity for the flow are chosen such that the fluid and magnetic Reynolds numbers, given by $Re = U_0\delta_\omega/\nu$ and $Re_m = U_0\delta_\omega/D_\eta$ are 250 each.

B_0 (T)	$M = 2V_A/U_0$	$R_A(x_2 = 0)$	Grid resolution	$\%$ perturbation intensity
0	0	0	$(\{1, 4\} \times 256)^2 \times 4$	$1\%, 3\%$
0.001	0.018	2E-3	$1024^2 \times 4$	1%
0.003	0.055	5.9E-3	$(\{1, 2, 3, 4, 5\} \times 256)^2 \times 4$	$1\%, 3\%$
0.01	0.184	0.019	$(\{1, 4\} \times 256)^2 \times 4$	$1\%, 3\%$
0.02	0.368	0.039	$1024^2 \times 4$	$1\%, 3\%$
0.03	0.55	0.059	$1024^2 \times 4$	$1\%, 3\%$
0.035	0.645	0.070	$1024^2 \times 4$	$1\%, 3\%$
0.04	0.737	0.078	$1024^2 \times 4$	$1\%, 3\%$
0.055	1.01	0.11	$1024^2 \times 4$	1%
0.075	1.38	0.15	$1024^2 \times 4$	$1\%, 3\%$
0.1	1.84	0.2	$1024^2 \times 4$	1%
0.3	5.5	0.59	$1024^2 \times 4$	$1\%, 3\%$

Table 5.1: Incompressible MHD mixing layers: Simulation parameters.

5.2.1 KH schematic and instability metrics

The choice of perturbations in equation (5.3) makes the center of streamwise-normal plane a pivot point about which the KH vortex evolves (Karimi & Girimaji, 2016). A schematic of the streamwise-normal plane of the flow field is shown in figure 5.1, with the pivot point identified as P. There are two more stagnation points, S_1, S_2, on the centerline at the streamwise boundaries. In addition, the plane is divided into four quadrants, $Q1 - Q4$ about P. This nomenclature is similar to that of Karimi & Girimaji (2016) and will be used to examine the perturbation evolution at different R_{A0} through the remainder of the chapter.

We examine the following metrics for establishing the degree of perturbation instability: circulation in the flow domain, total pressure at the pivot point, P, and volume-averaged perturbation kinetic and magnetic energies. Circulation is an indicator of the degree of mixing and entrainment in the flow domain (Karimi & Girimaji, 2016) and is computed using the following expression:

$$\Gamma = \oint \vec{u'} \cdot \vec{dl}. \tag{5.4}$$

The line integral is computed around a square loop of side $L_1/2$ centered at P. Total pressure at

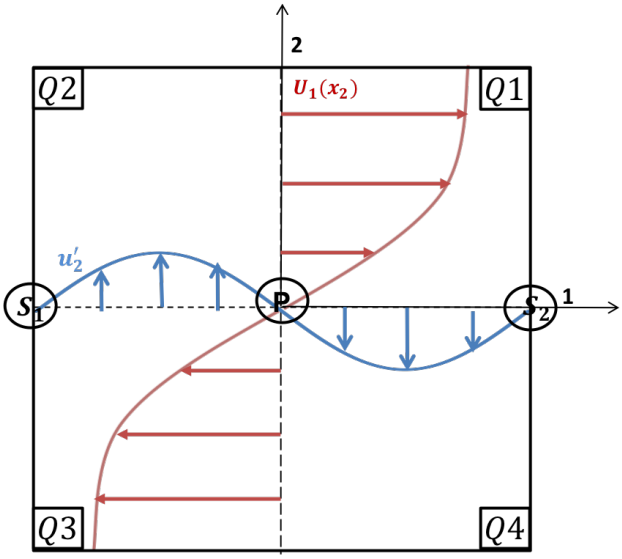

Figure 5.1: Schematic showing the pivot point.

the pivot point assesses the strength of rollup and vortical motion. The greater the level of suction at P, the stronger is the KH vortex.

5.2.2 Verification

Since MGKM is a compressible flow solver, an appropriately low convective Mach number needs to be chosen in order to capture incompressible behavior. We consider mixing layers at Mach numbers of 0.03 and 0.3 to compare their evolution. Figure 5.2 presents the development of circulation and perturbation kinetic energy for the above two Mach numbers. As their time evolution is almost identical, Mach number 0.3 is deemed appropriate for this study at the incompressible limit.

Grid convergence in the MHD limit. We perform grid sensitivity studies for the magnetic field case of $R_{A0} = 0.0059$ using grids of resolution $256^2 \times 4$, $512^2 \times 4$, $768^2 \times 4$, $1024^2 \times 4$ and $1280^2 \times 4$. To demonstrate grid convergence, we plot volume-averaged values of kinetic and magnetic energies in figures 5.3(a),(b), respectively. The above figures indicate that both these volume-averaged statistics converge beyond resolutions of $1024^2 \times 4$. We only present results for grids resolutions of $1024^2 \times 4$ or higher.

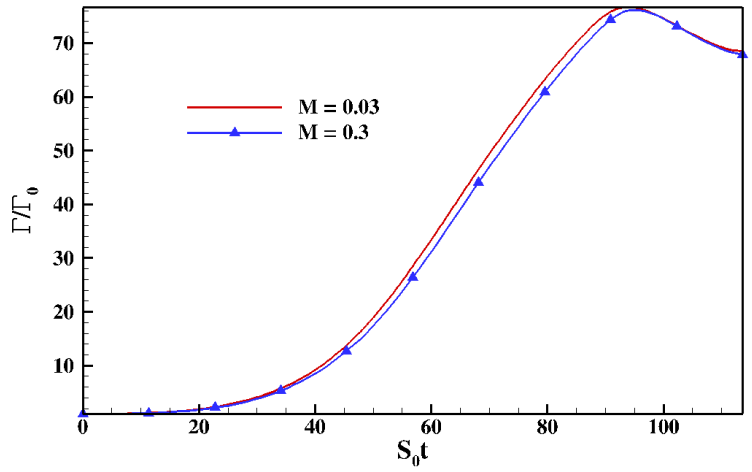

(a)

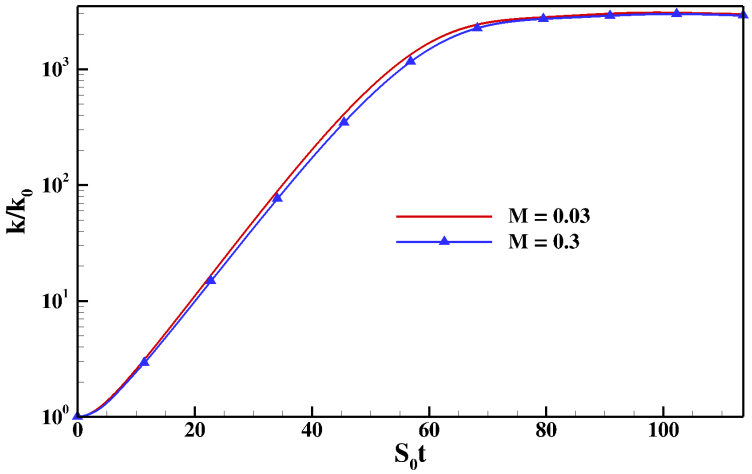

(b)

Figure 5.2: Normalized (a) circulation and (b) volume-averaged kinetic energy, k/k_0, for Mach numbers 0.03 and 0.3.

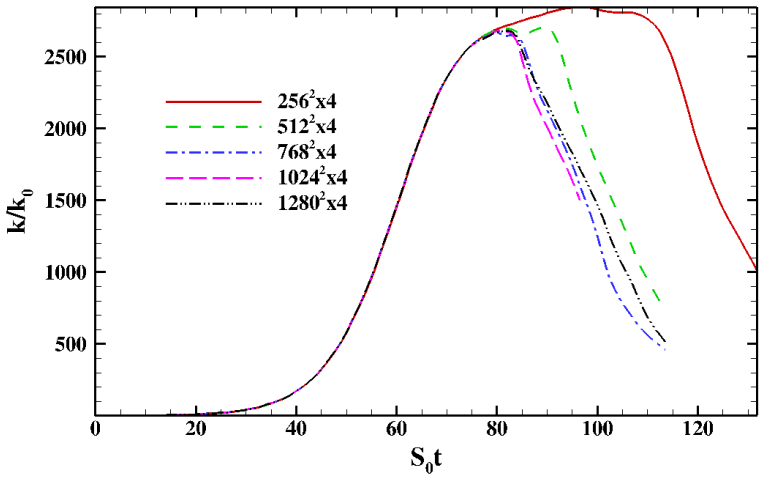

(a)

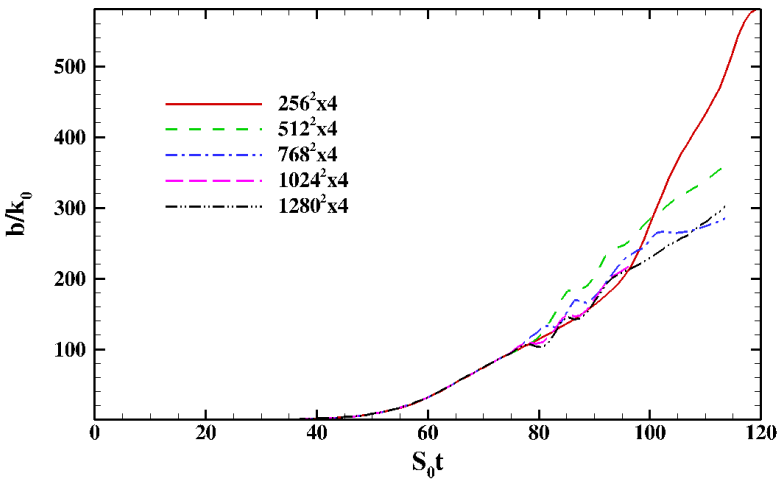

(b)

Figure 5.3: Volume-averaged (a) kinetic (k/k_0) and (b) magnetic (b/k_0) energies for $R_{A0} = 0.0059$ at different grid resolutions.

5.3 Results

We present results from MHD mixing layer simulations at different imposed magnetic field strengths and contrast them against the hydrodynamic limit. We will then investigate in detail the underlying flow and magnetic field mechanisms leading to stabilization or growth.

5.3.1 KH instability in hydrodynamic mixing layer

We now present the dynamics of KH instability in the hydrodynamic limit which will serve as the benchmark for comparison against MHD cases. We review the three-stage development of incompressible KH instability identified by Karimi & Girimaji (2016): linear, merger-rollup and nonlinear stages.

Linear growth stage. Figure 5.4(a) shows the spanwise perturbation vorticity contours in the first stage of evolution. We observe the development of positive anti-clockwise vorticity in Q1 and Q3 and negative clockwise vorticity in Q2 and Q4 near the pivot point, P. The formation of these *precursor vortices* can be explained examining the production term in spanwise vorticity equation (2.95): $u_2^{'} d^2U_1/dx_2^2$. The simulations are initialized such that $u_2^{'}$ is negative in Q1, Q4 and positive in Q2, Q3. However, d^2U_1/dx_2^2 is negative in Q1, Q2 and positive in Q3, Q4. This implies that negative or clockwise vorticity is generated in Q2, Q4 and positive or anticlockwise vorticity is generated in Q1 and Q3. Then the Poisson equation for pressure dictates that low and high pressures are generated at P and $S_1 \& S_2$, respectively (figure 5.5(a)).

Merger and rollup stage. The pressure-velocity coupling leads to positive feedback between negative pressure (p) and normal velocity ($u_2^{'}$) (Karimi & Girimaji, 2016). This coupling intensifies suction at P and $u_2^{'}$ magnitude with time resulting in sustained production of negative vorticity. Therefore due to low pressure at P, the two negative vortex regions in Q2 and Q4 merge leading to the formation of the *primary vortex* as seen in figure 5.4(b). Positive vorticity in Q1 and Q3 is eliminated. As evident from the monotonic increase of circulation in figure 5.6(a), the merged primary vortex rolls up, entraining more surrounding fluid. This stage is also characterized by the formation of an extreme low pressure region at P, as seen in figures. 5.5(b), 5.7(a).

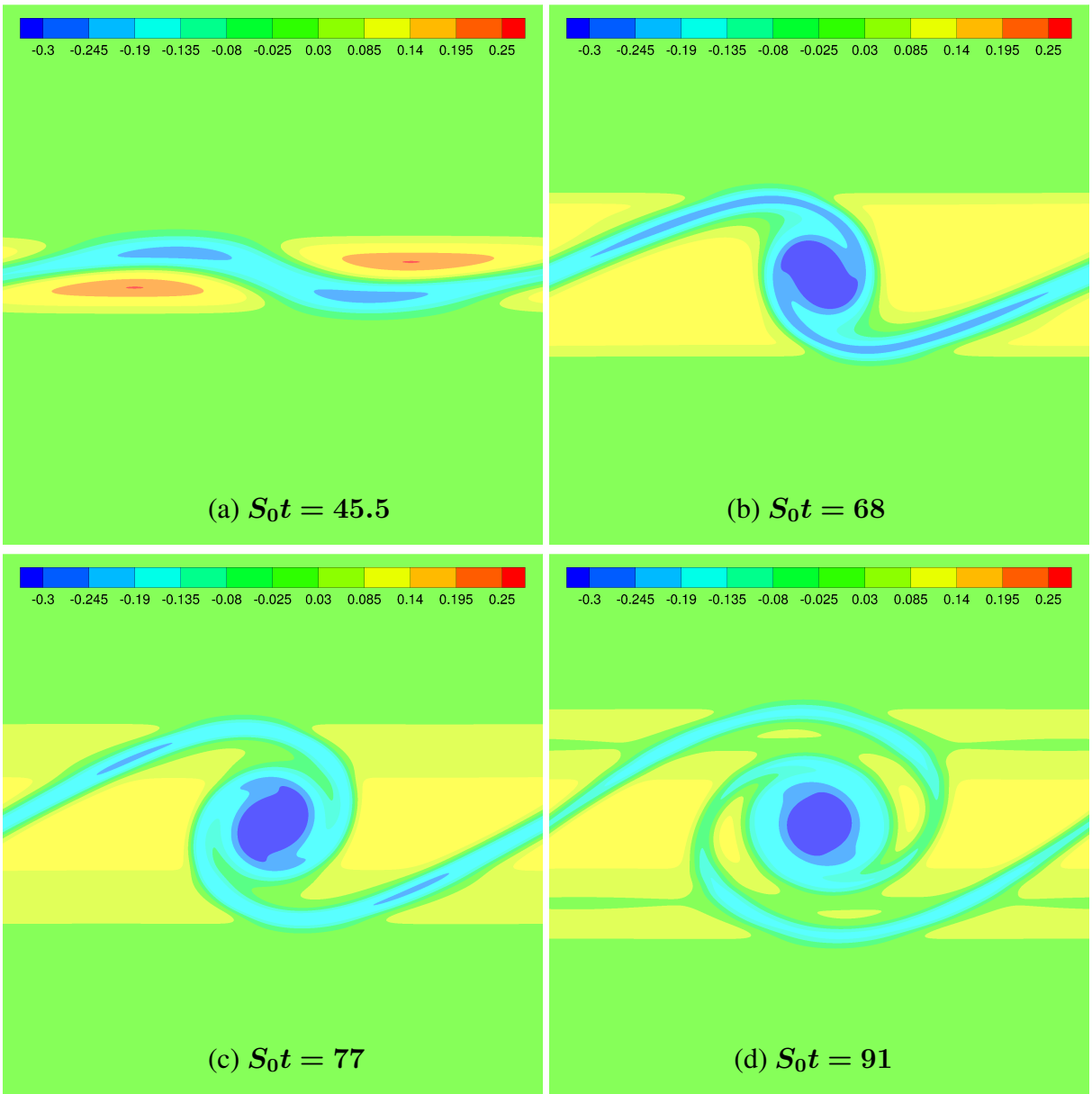

Figure 5.4: *Hydrodynamic KH instability*: Spanwise vorticity perturbation contours.

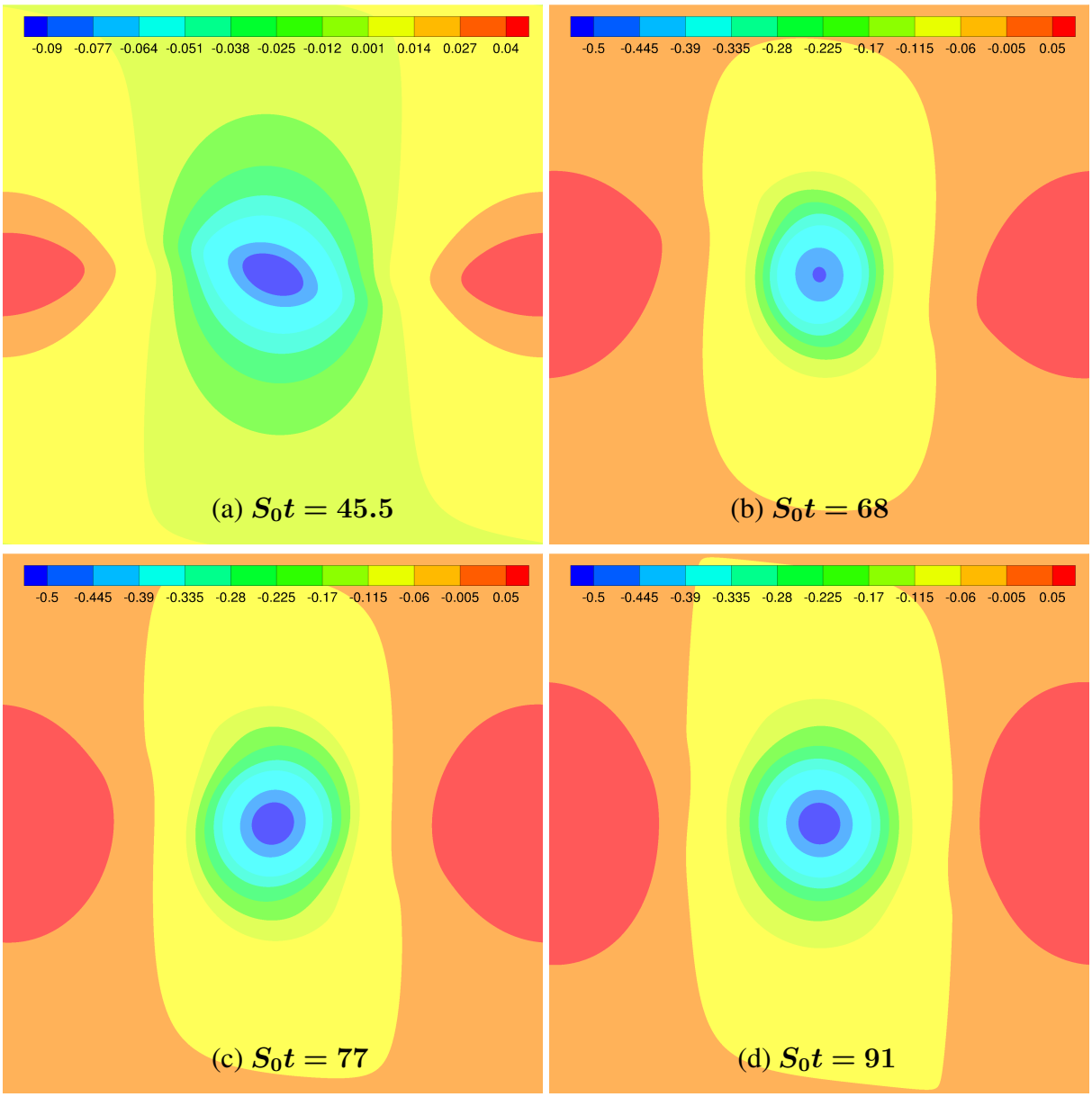

Figure 5.5: *Hydrodynamic KH instability*: Fluid gauge pressure contours.

Nonlinear stage. As the primary vortex rollup intensifies, *early nonlinear stage* culminates with wave-breaking as evidenced from figure 5.4(c). This is followed by *asymptotic nonlinear stage* characterized by the formation of *secondary vortex bands* (figure 5.5d). Figures 5.6(a) and 5.7(a) show that circulation and suction pressure at P saturate during this stage.

5.3.2 KH instability in MHD mixing layers

The nature of perturbation development in conducting fluids depends upon the strength of the imposed magnetic field. Figure 5.6 compares the circulation evolution of different MHD cases against the baseline hydrodynamic behavior. It can be seen that the circulation values decrease with increasing magnetic field strength. $R_{A0} < 0.019$ cases (figure 5.6a) exhibit similar behavior as the pure hydrodynamic case up to $S_0 t \approx 80$, i.e., until the *merger and rollup stage* of KH instability. After $S_0 t \approx 80$, circulation in these cases decreases. For the cases of $R_{A0} = (0.039 - 0.078)$ in figure 5.6(a), circulation begins to deviate from the hydrodynamic behavior at an earlier time of $S_0 t \approx 20$. Beyond $S_0 t \approx 20$, circulation in these cases is always lower than $R_{A0} \leq 0.019$ cases. For $R_{A0} \geq 0.11$ in figure 5.6(b), the circulation is always lower than its initial value and experiences an oscillatory evolution.

Figure 5.7 shows the evolution of gauge value of total pressure at the pivot point, P, i.e., total pressure relative to its value at the beginning of the simulation. Suction at P for $R_{A0} \leq 0.019$ is similar to the hydrodynamic case up to $S_0 t \approx 80$, but starts to change at later times. The amount of suction at the core decreases as magnetic field strength is increased as seen in figure 5.7(a) for $R_{A0} \geq 0.039$. For $R_{A0} \geq 0.11$ shown in figure 5.7(b), the suction pressure is considerably lower than the hydrodynamic cases and experiences an oscillatory evolution about zero.

The maximum values of circulation and suction pressure are strong indicators of degree of KH instability growth - the larger the values, the stronger is the instability. We now plot the maximum circulation and suction pressure computed at different magnetic field strengths and perturbation intensities in figure 5.8(a). As observed in figures 5.6, 5.7, the maximum values of circulation and suction pressure decrease with increasing magnetic field strength. Figure 5.8(b) depicts the values of volume-averaged perturbation kinetic and magnetic energies at the instant when maximum cir-

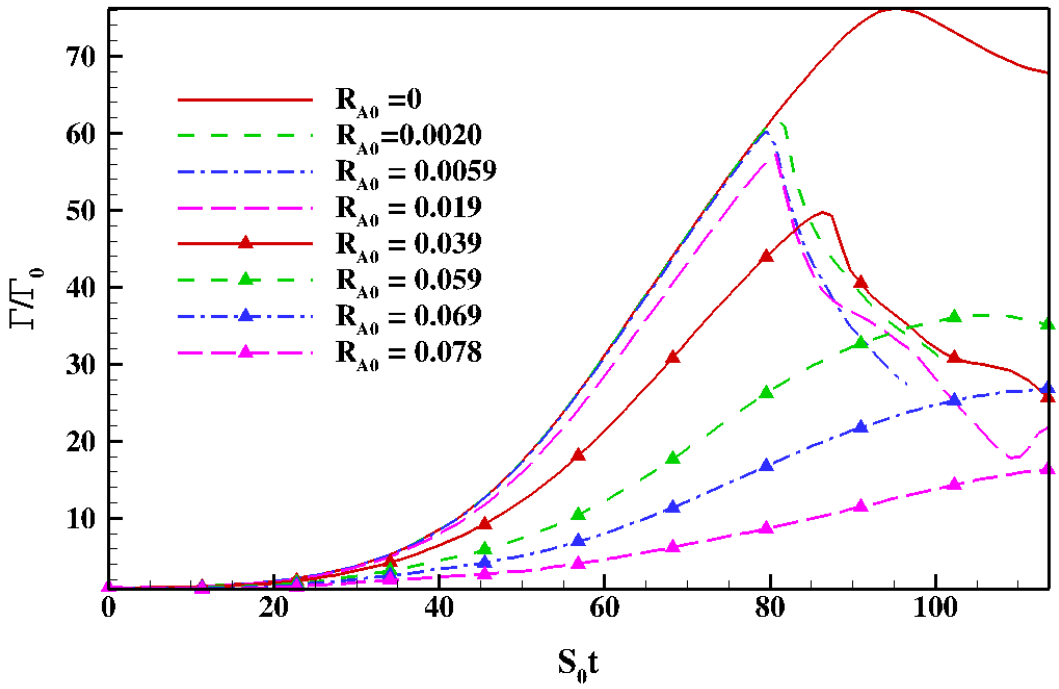

(a)

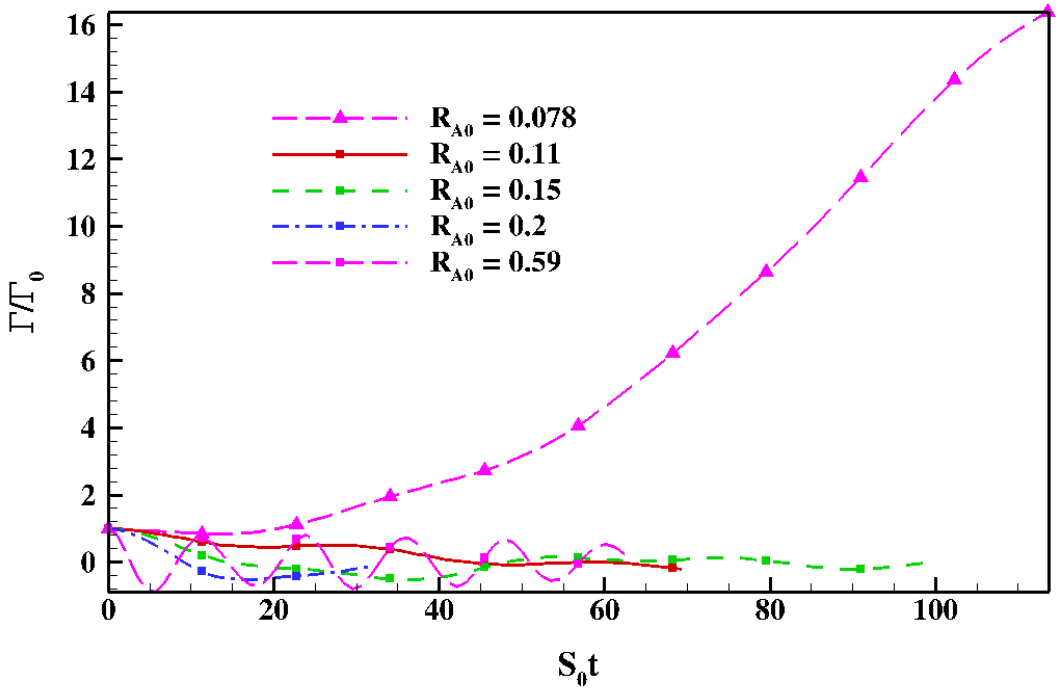

(b)

Figure 5.6: Circulation for (a) $R_{A0} \leq 0.078$, (b) $R_{A0} \geq 0.078$. Perturbations with 1% intensity are plotted here.

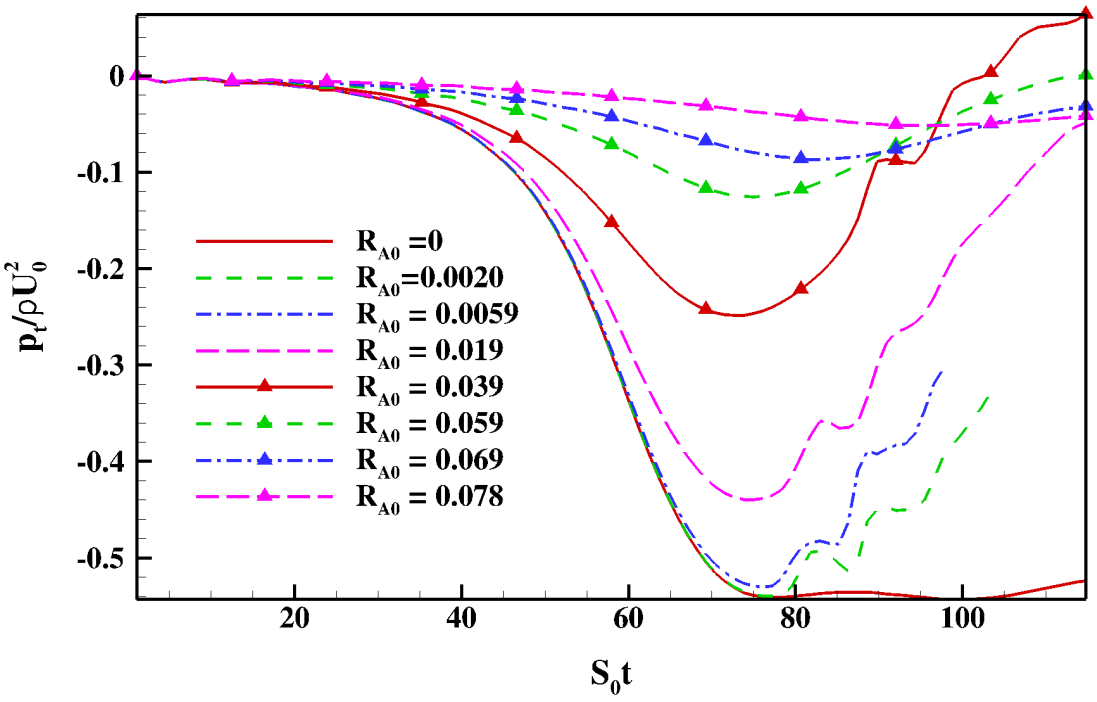

(a)

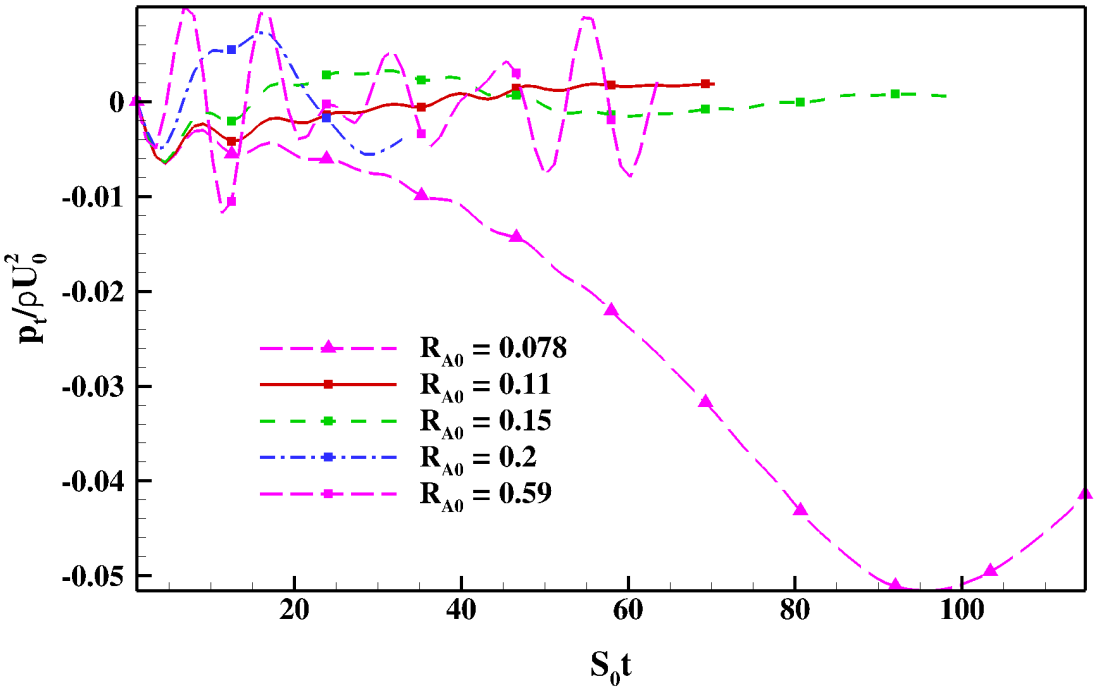

(b)

Figure 5.7: Total pressure at P for (a) $R_{A0} \leq 0.078$, (b) $R_{A0} \geq 0.078$. Perturbations with 1% intensity are plotted here.

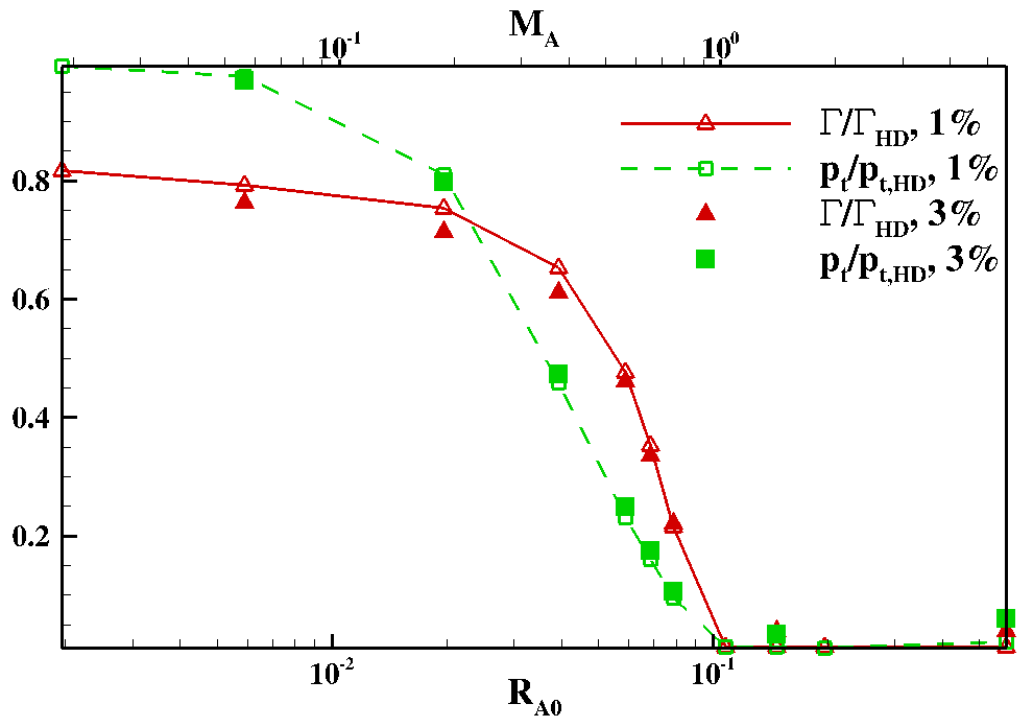

(a)

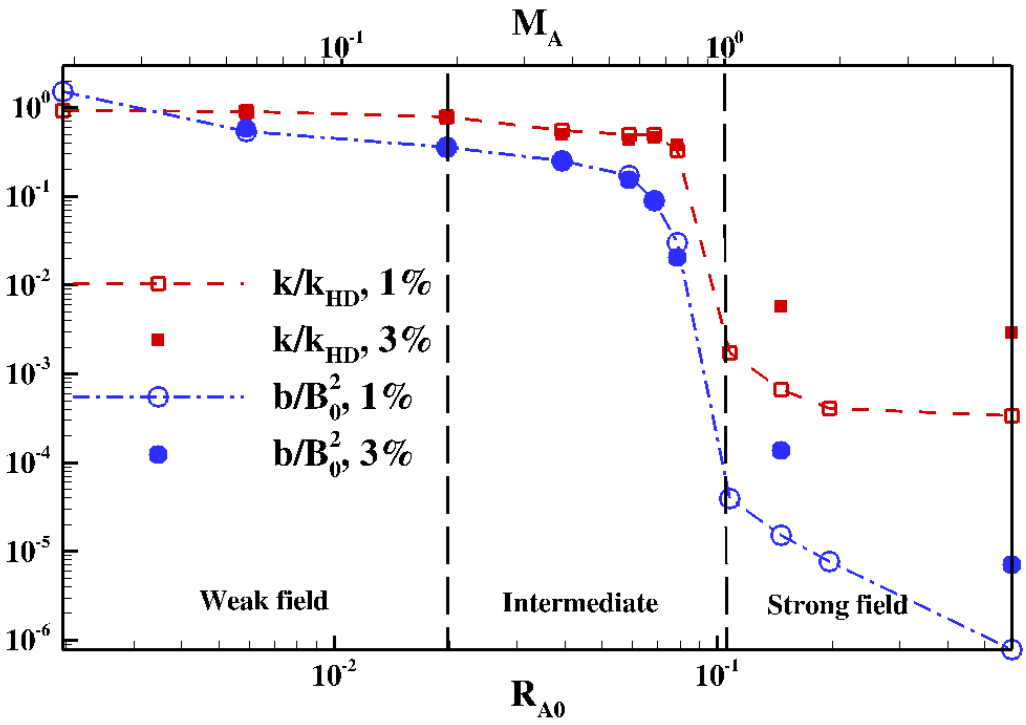

(b)

Figure 5.8: For different magnetic field strengths: (a) Maximum circulation and suction pressure at P, (b) Perturbation kinetic and magnetic energy amplification at maximum circulation.

culation is achieved. Based on figure 5.8(b), magnetic field effects can be categorized into strong, weak and intermediate regimes as follows:

1) *Weak field regime*, $M_A \leq 0.2$ or $R_{A0} \leq 0.019$: The maximum value of volume-averaged kinetic energy is smaller than the baseline hydrodynamic KH instability, but is of the same order. Thus the mixing layer is unstable, but the degree of perturbation amplification is lower than the hydrodynamic case. This is similar to what has been observed in the works of Malagoli *et al.* (1996); Mak *et al.* (2017).

2) *Strong field regime*, $M_A > 1$ or $R_{A0} \geq 0.15$: The volume-averaged kinetic energy remains close to initial value indicating no growth or instability. This result is consistent with the linear analysis performed by Chandrasekhar (1961); Lau & Liu (1980).

3) *Intermediate field regime*, $0.2 < M_A < 1$ or $0.019 < R_{A0} < 0.15$: The volume-averaged kinetic energy grows but the maximum amplification is an order-of-magnitude (or more) smaller than the hydrodynamic case. This is along the lines of Frank *et al.* (1996).

It is important to note that none of the studies in literature have examined the entire range of magnetic field strengths with a single set of simulations. The current study enables us to delineate the ranges of different magnetic field regimes more precisely than previous works.

We now characterize the spatio-temporal evolution of perturbations in weak, intermediate and strong field regimes and contrast it against the hydrodynamic behavior.

5.3.2.1 Strong field regime

We now consider the various stages of perturbation development in the strong field regime for the case of $R_{A0} = 0.59$ or $M_A = 5.5$. Vorticity and pressure contours at two representative times are shown in figure 5.9.

Dominant physics. $R_A(x_2) \gg 1$ at almost all locations in the domain. Therefore, harmonic exchange between velocity and magnetic fields is the dominant process, as seen in linear analysis Section 2.1.2.1. This harmonic exchange results in oscillatory, out-of-phase evolution of $u_2^{'}$ and $B_2^{'}$ about zero at pivot point, P, as seen in figure 5.10(a).

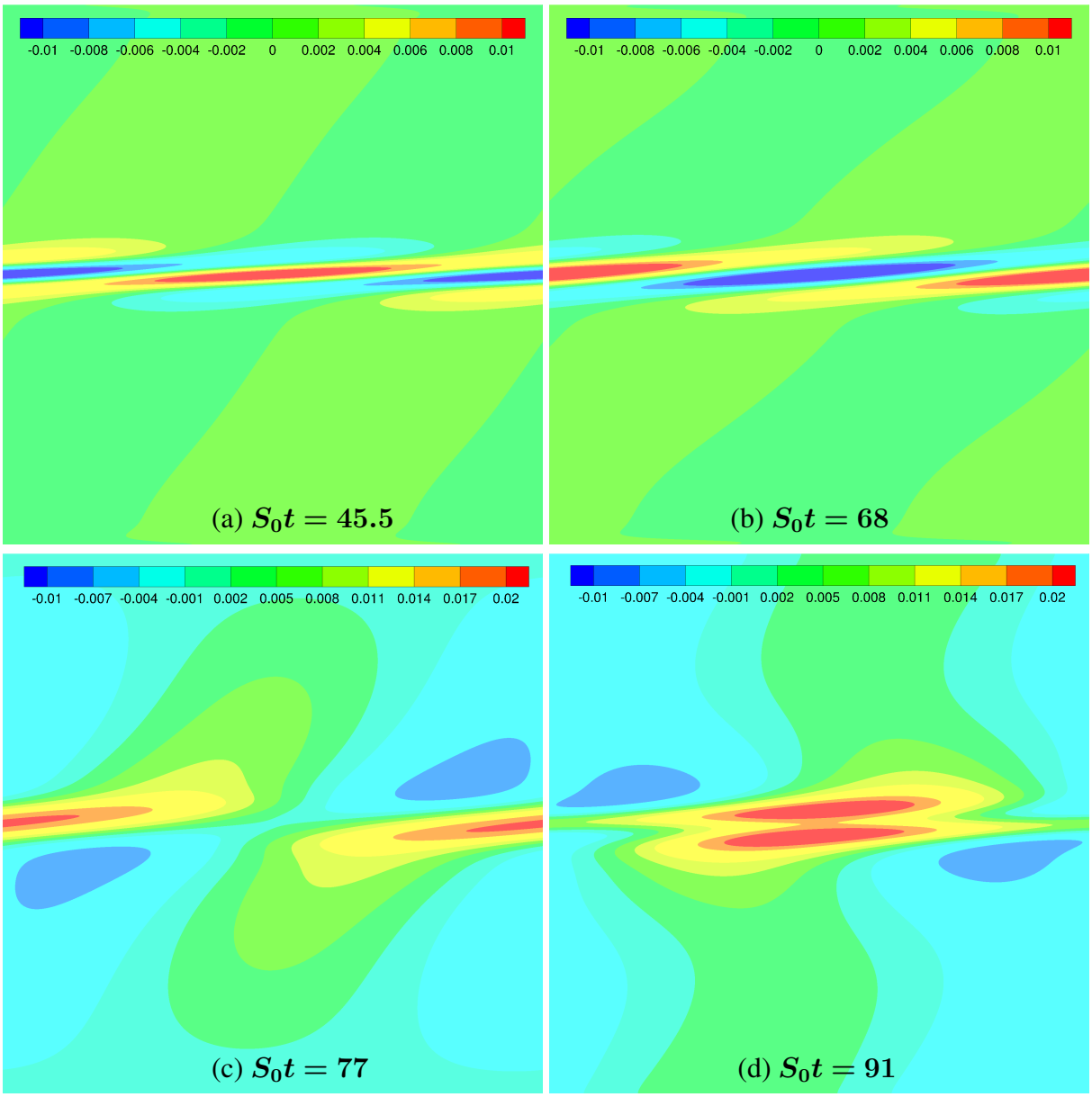

Figure 5.9: *Strong field regime*, $R_{A0} = 0.59$: (a), (b) Spanwise vorticity and (c), (d) fluid gauge pressure.

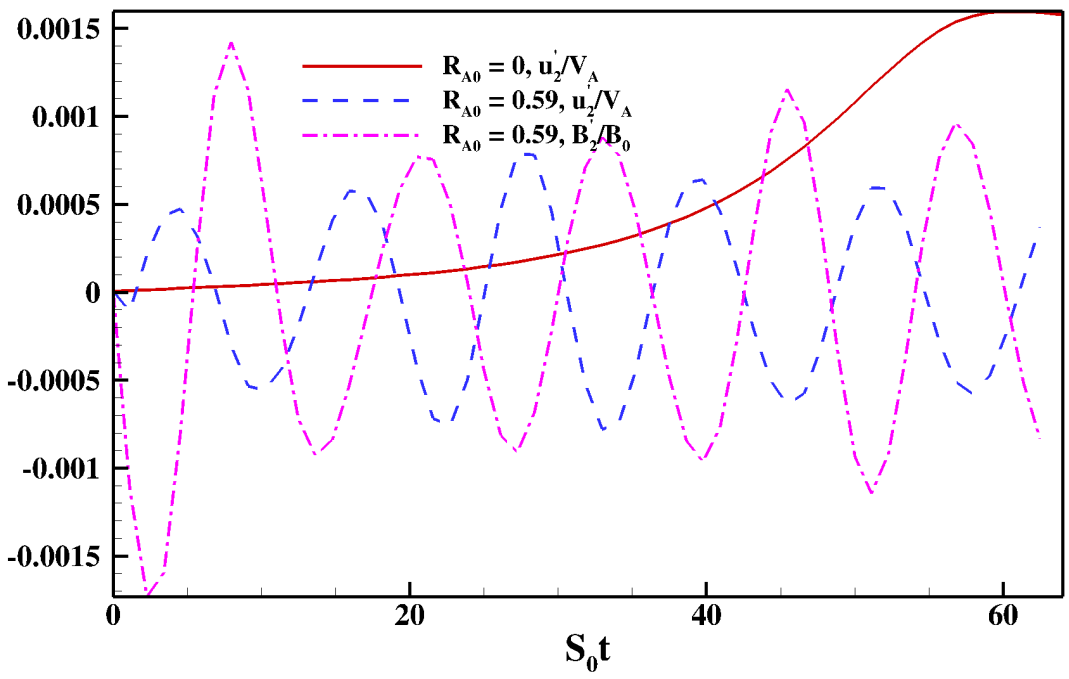

(a)

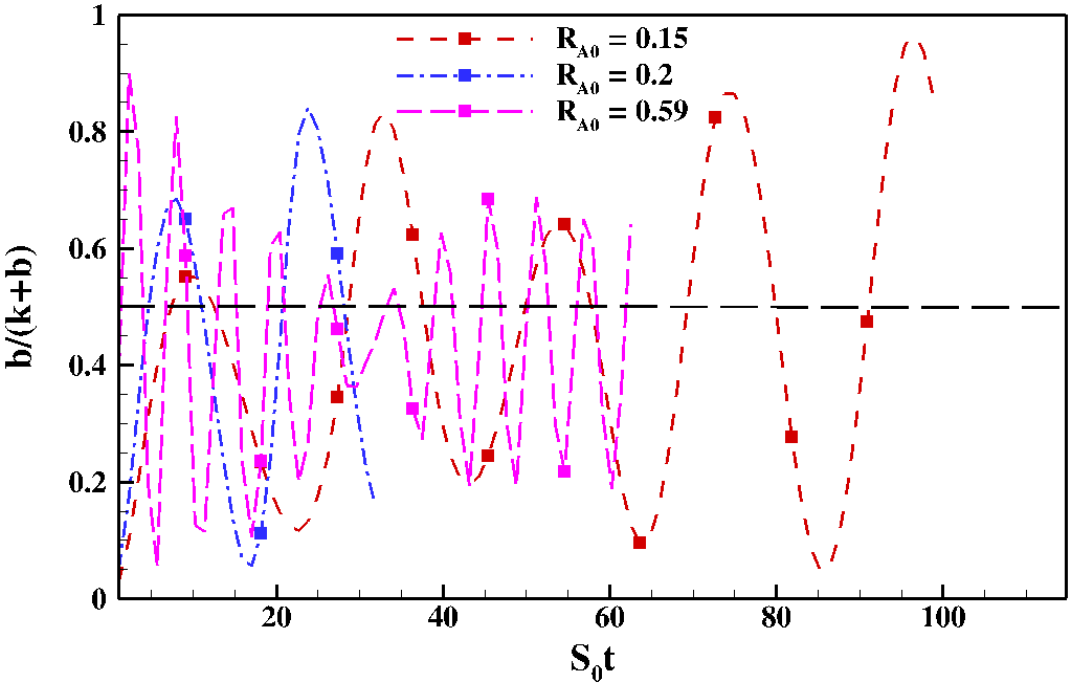

(b)

Figure 5.10: *Strong field regime*: Evolution of (a) $u_2^{'}, B_2^{'}$ at P for $R_{A0} = 0.59$ and (b) Φ_b for $R_{A0} = 0.15 - 0.59$

Flow field evolution. The oscillatory evolution of $u_2^{'}$ leads to reduced accumulation of kinetic energy as production alternates between positive and negative values (equation 2.98). Vorticity production given by, $u_2^{'} d^2U_1/dx_2^2$, is also considerably reduced as seen in figures 5.9(a),(b). Therefore, *linear growth stage*, i.e., the first stage of hydrodynamic KH instability, is entirely eliminated owing to the winding and unwinding nature of precursor vortices. Neither unidirectional rollup of precursor vortices leading to the formation of primary vortex nor the development of low pressure core at P are seen in figures 5.9(b)-(d). As velocity field perturbations do not grow beyond their initial values, KH instability is suppressed.

Magnetic field evolution. As a result of oscillatory evolution of $B_2^{'}$, magnetic stretching production also alternates between positive and negative values leading to low $B_1^{'}$. Magnetic field does not develop high levels of inhomogeneity forestalling the possibility of resistive instability.

Equipartition. Dominance of harmonic exchange results in equipartition between perturbation velocity and magnetic fields as seen from figure 5.10(b). Equipartition is seen in the range of $R_{A0} = 0.15 - 0.59$.

Overall, in this regime, even the early stages of hydrodynamic and MHD development are very different due to the dominance of velocity-magnetic field interactions over hydrodynamic mechanisms.

5.3.2.2 Weak field regime

Here we illustrate the different stages of perturbation evolution in the weak field regime for the case of $R_{A0} = 0.0059$ or $M_A = 0.055$. Figures 5.11, 5.12 and 5.13 depict the contours of perturbation vorticity, fluid gauge pressure and streamwise induced magnetic field at $S_0 t = 45.5, 68, 77$ and 91.

Dominant physics. In this case, $R_A(x_2) < 1$ at most locations in the interior of the domain leading to initial hydrodynamic type behavior. The hydrodynamic processes dominate over $u_i^{'} - B_i^{'}$ interactions (Section 2.1.2.1).

Flow field evolution. $u_2^{'}$ (figure 5.14a for P) experiences monotonic evolution like in hydrodynamic limit, giving rise to sustained production of kinetic energy and vorticity. Contours of

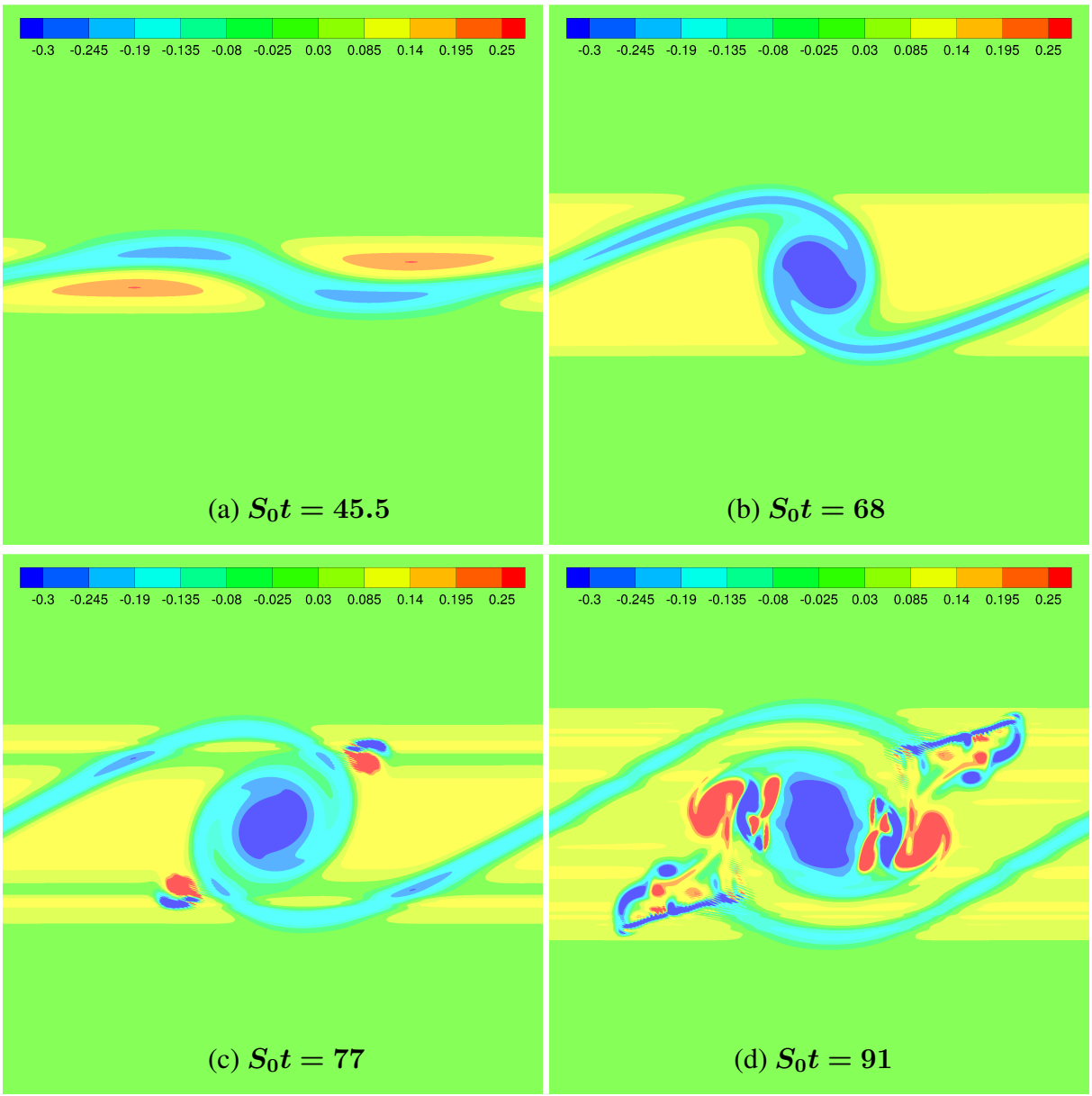

Figure 5.11: *Weak field regime*, ($R_{A0} = 0.0059$): Spanwise vorticity perturbation contours.

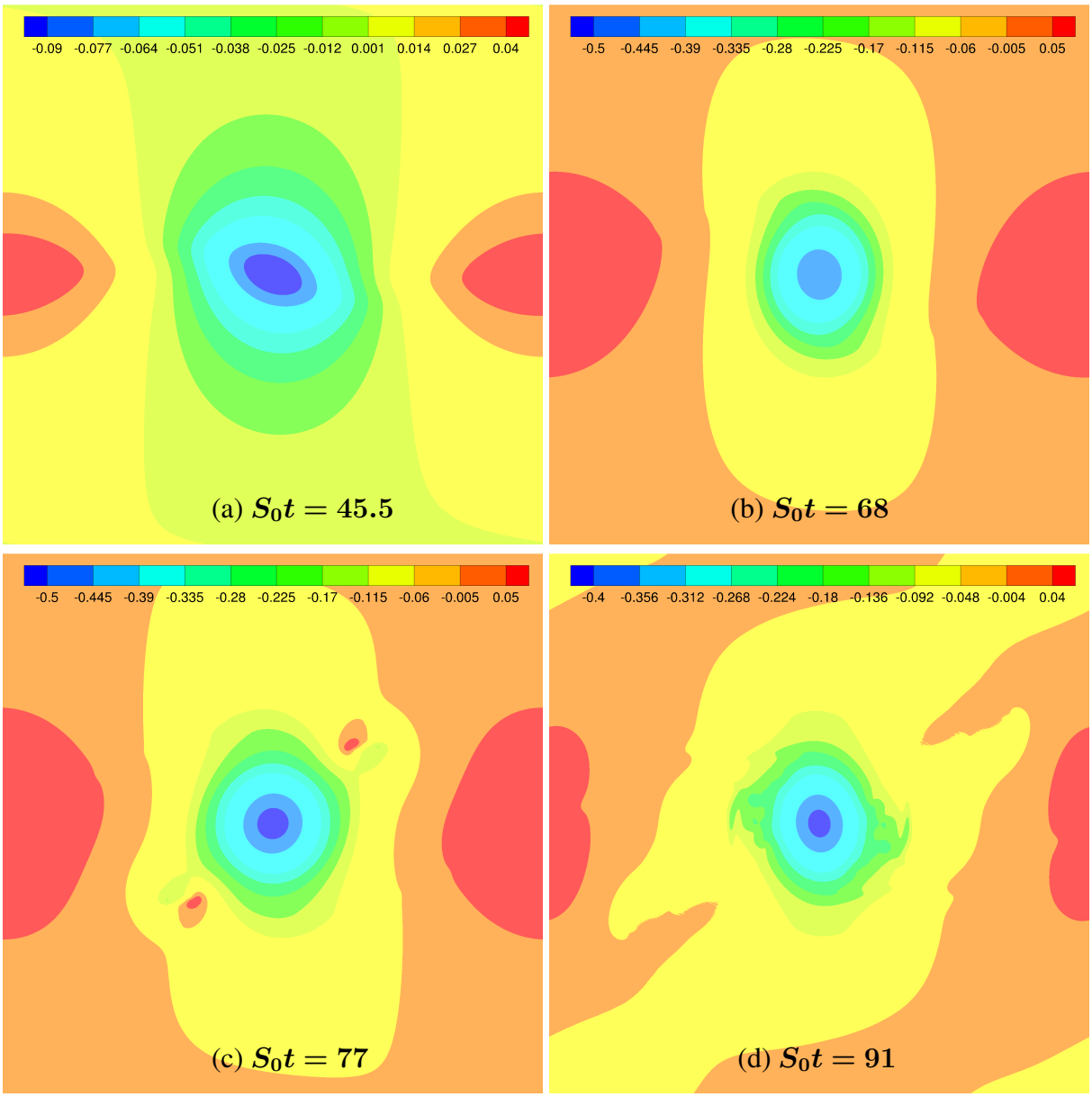

Figure 5.12: *Weak field regime*, ($R_{A0} = 0.0059$): Fluid gauge pressure contours.

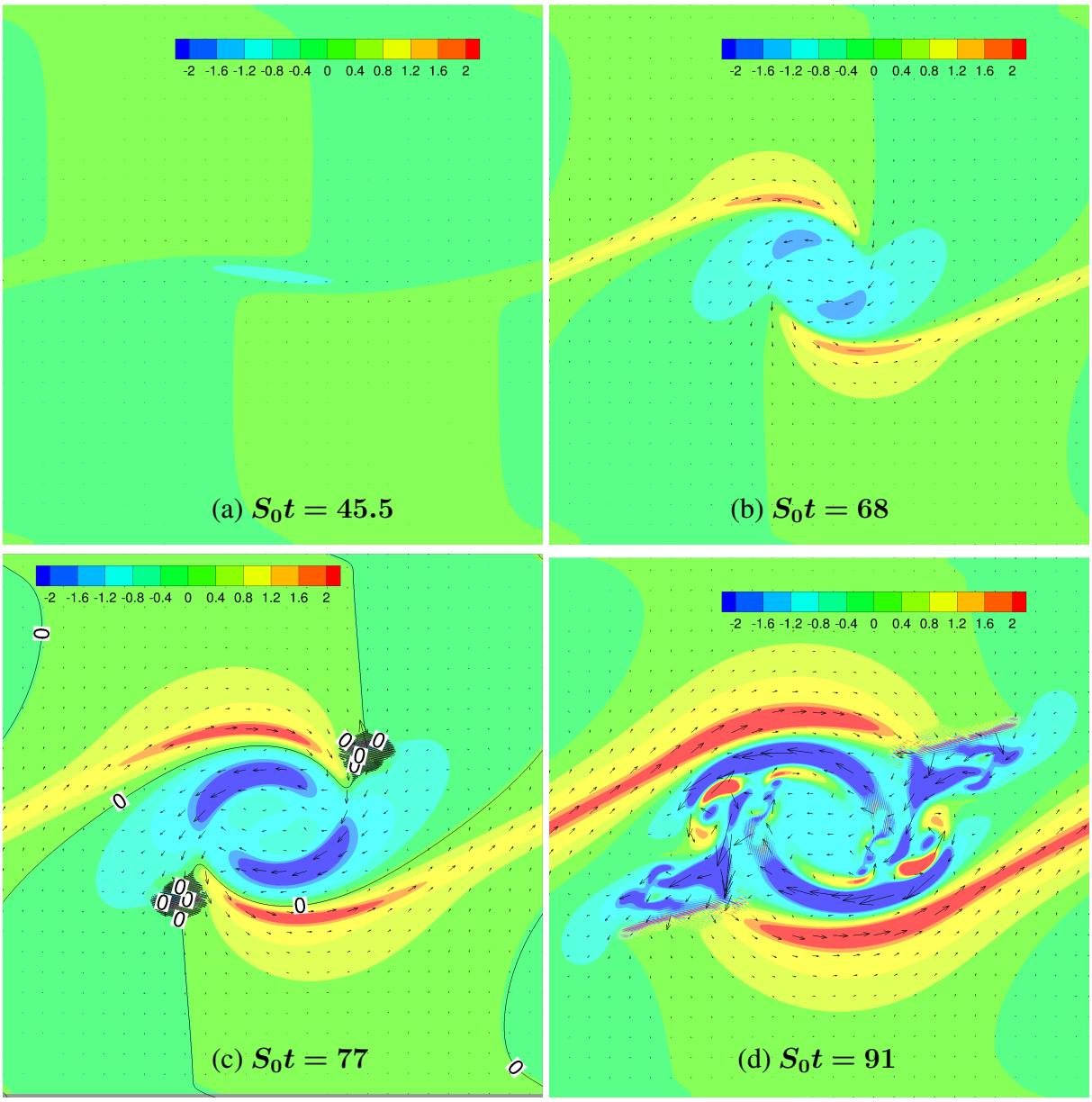

Figure 5.13: *Weak field regime*, ($R_{A0} = 0.0059$): Streamwise induced magnetic field, $B_{I,1}$, overlaid with perturbation magnetic field vectors. The line along which $B_{I,1} = 0$ is also indicated at $S_0t = 77$ (c).

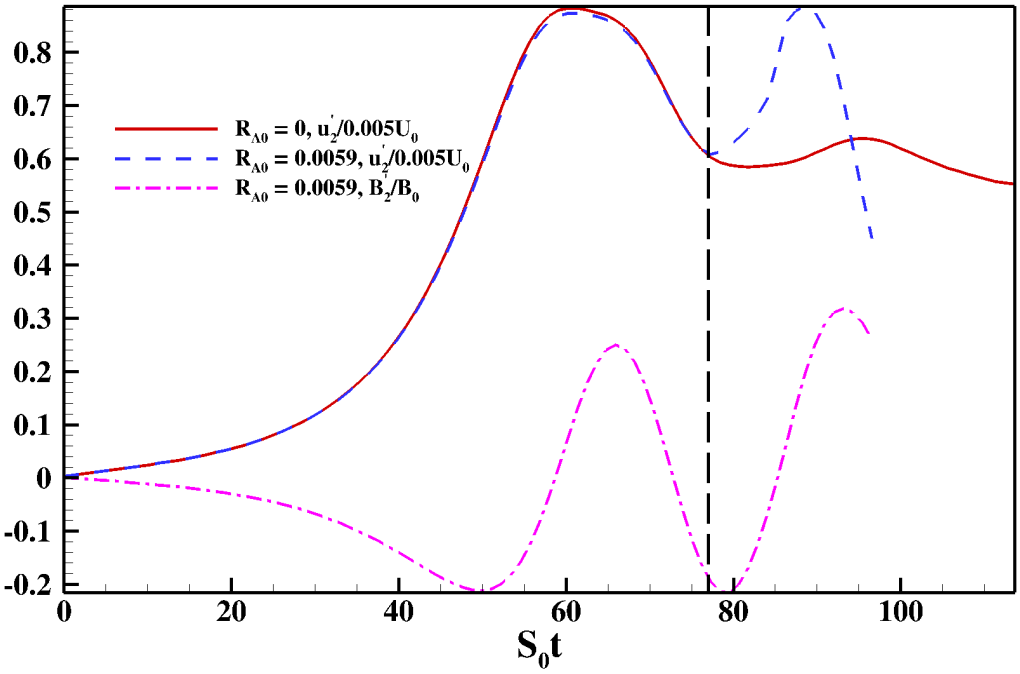

(a)

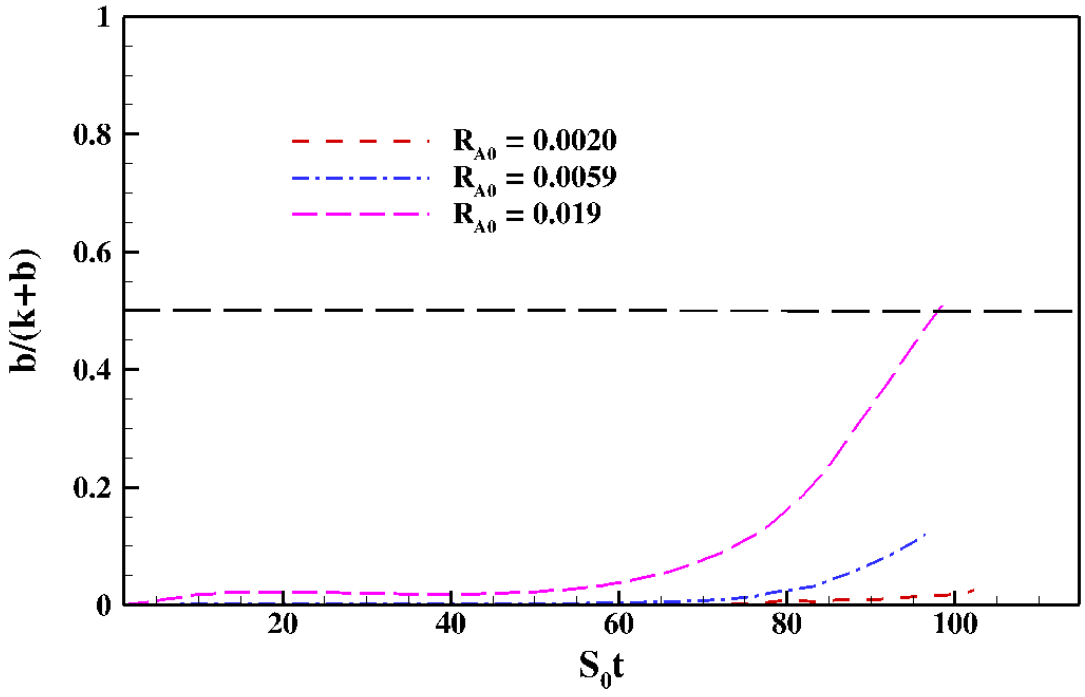

(b)

Figure 5.14: *Weak field regime*: Evolution of (a) $u_2^{'}, B_2^{'}$ at P for $R_{A0} = 0.0059$ and (b) Φ_b for $R_{A0} = 0.002 - 0.019$.

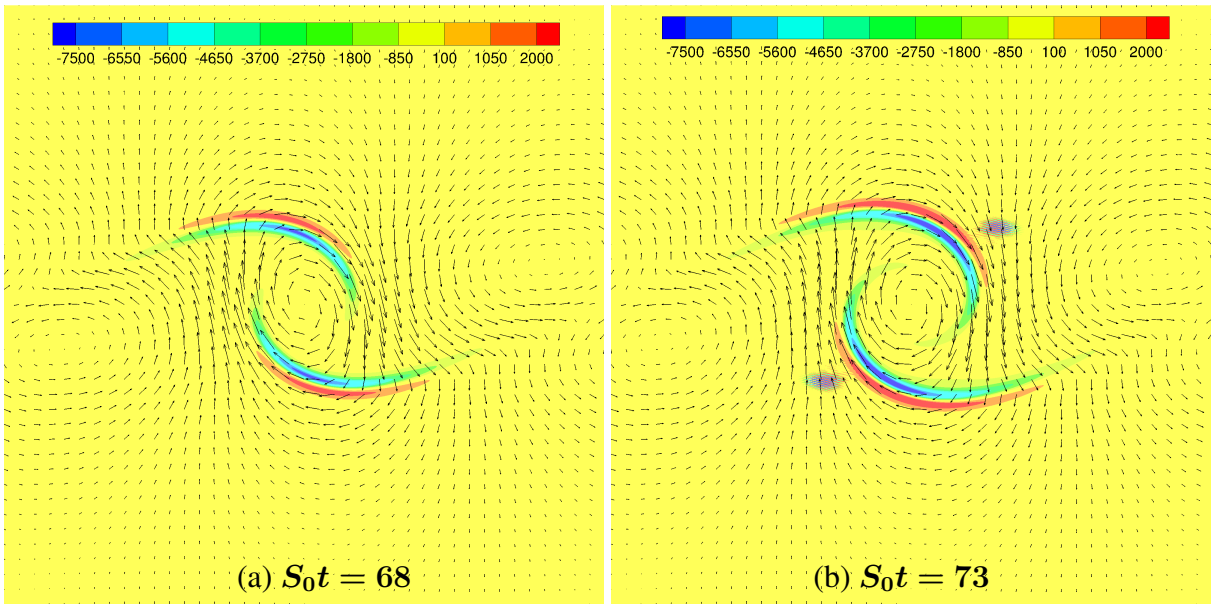

Figure 5.15: *Weak field regime*, $R_{A0} = 0.0059$: Lorentz work contours overlaid with perturbation velocity vectors.

vorticity and fluid pressure in figures 5.11(a),(b) and 5.12(a),(b) at $S_0t = 45.5, 68$ are similar to those seen in *linear growth* and *merger-rollup* stages in the hydrodynamic case. Formation of primary vortex is seen at $S_0t = 68$. Beyond $S_0t \approx 80$, the perturbation growth transitions from linear to nonlinear regime.

Magnetic field evolution. Lorentz work contours computed using equation (5.1) are shown in figures 5.15(a),(b). As primary vortex rolls up, there is a narrow (inner) band in the flow field where work is done by velocity on magnetic field. Consequently, magnetic energy in this narrow inner band increases producing a clear inhomogeneity in magnetic field. However, in another (outer) band adjacent to the inner band, work is done on velocity field by magnetic field (ideal MHD). Due to Lorentz work, during the process of KH evolution, energy is transferred from $u_2^{'}$ to $B_2^{'}$ which results in the monotonic evolution of $B_2^{'}$ (figure 5.14a). This gives rise to magnetic stretching production of $B_1^{'}$ as evidenced from figures 5.13(a),(b). In figures 5.13(c), 5.15(b) resistive instability is onset in the vicinity of the outer band at the locations where there is an inflection point in magnetic field (non-ideal MHD). The evidence of resistive instability can also be seen

from the formation of magnetic islands in figure 5.13(d) (Palotti *et al.*, 2008).

Magnetic field effects. Once the resistive instability is onset in the outer bands, the effects propagate through flow field causing the dynamics to deviate from hydrodynamic behavior. This can be seen in vorticity and pressure contours in figures 5.11(c),(d) and 5.12(c),(d). Secondary vortex bands in figure 5.11(d) are disrupted. The vortex disruption is similar to that seen in Mak *et al.* (2017). The deviation from hydrodynamic-like evolution of $u_2^{'}$ due to resistive instability can be seen in figure 5.14(a). Circulation as shown in figure 5.6(a) is also considerably curtailed.

Equipartition. Since harmonic exchange is not a dominant process in this regime, equipartition between perturbation velocity and magnetic fields can not be expected. Figure 5.14(b) shows Φ_b for various cases in weak field regime. Φ_b for $R_{A0} = 0.002, 0.0059$ cases are far from equipartition even after the onset of resistive instability. However, $R_{A0} = 0.019$ case tends towards equipartition after the onset of resistive instability.

Overall, in this regime, the first two stages of KH instability are similar to that of hydrodynamic KH instability leading the formation of primary vortex and low pressure core around P. However, the third stage of KH growth and secondary vortex bands are disrupted by the magnetic field *via* the onset of resistive instability.

5.3.2.3 Intermediate field regime

The perturbation evolution in the intermediate magnetic field regime for the case of $R_{A0} = 0.078$ or $M_A = 0.74$ is examined in figures 5.16 and 5.17.

Dominant physics. The behavior of perturbations in this regime is intermediate between strong and weak field regimes with production and harmonic exchange being significant in different regions of the mixing layer.

Flow field evolution. $u_2^{'}$ at P shown in figure 5.16(a) is monotonic with reduced amplitude resulting in reduced production of kinetic energy and vorticity. The strength of precursor vortices at $S_0t = 45.5$ in figure 5.17(a) is considerably reduced compared to that seen in the *linear growth* stage of hydrodynamic case. Low pressure region at P is not formed at $S_0t = 45.5, 91$ in figures 5.17(c),(d). Consequently, the negative clockwise precursor vortices in Q2 and Q4

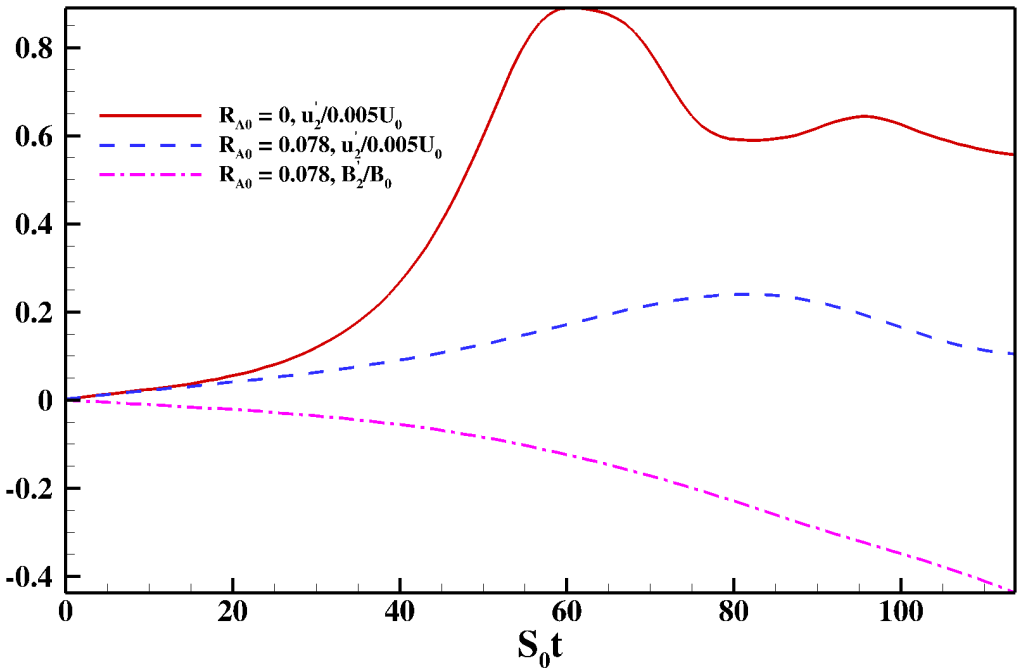

(a)

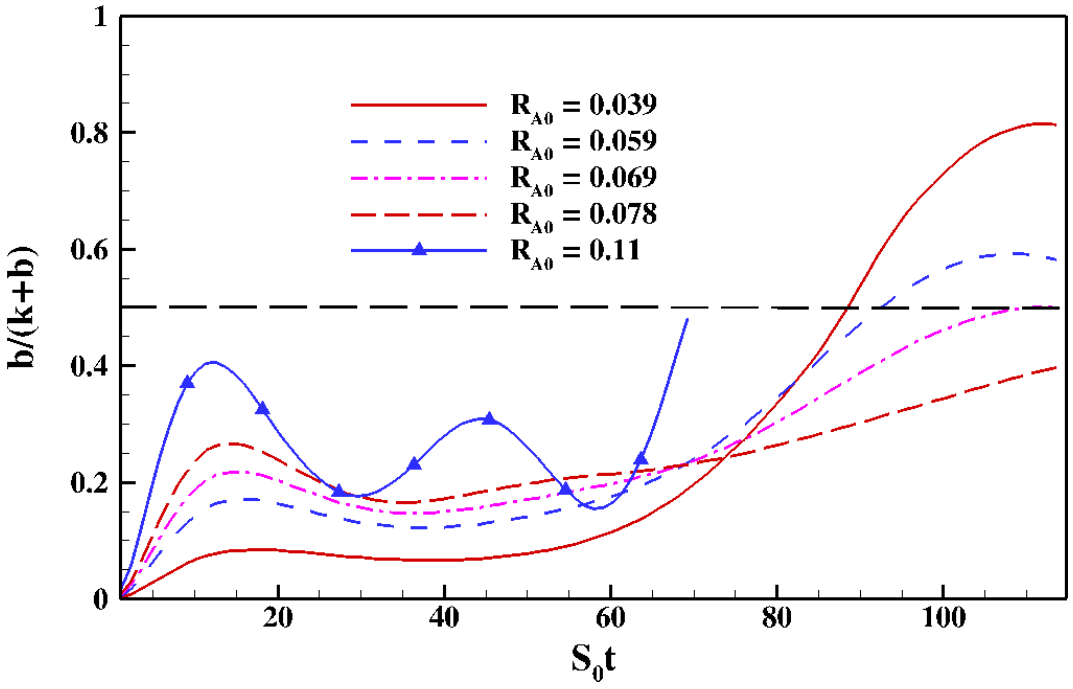

(b)

Figure 5.16: *Intermediate regime*: Evolution of (a) u_2', B_2' at P for $R_{A0} = 0.078$ and (b) Φ_b for $R_{A0} = 0.039 - 0.11$.

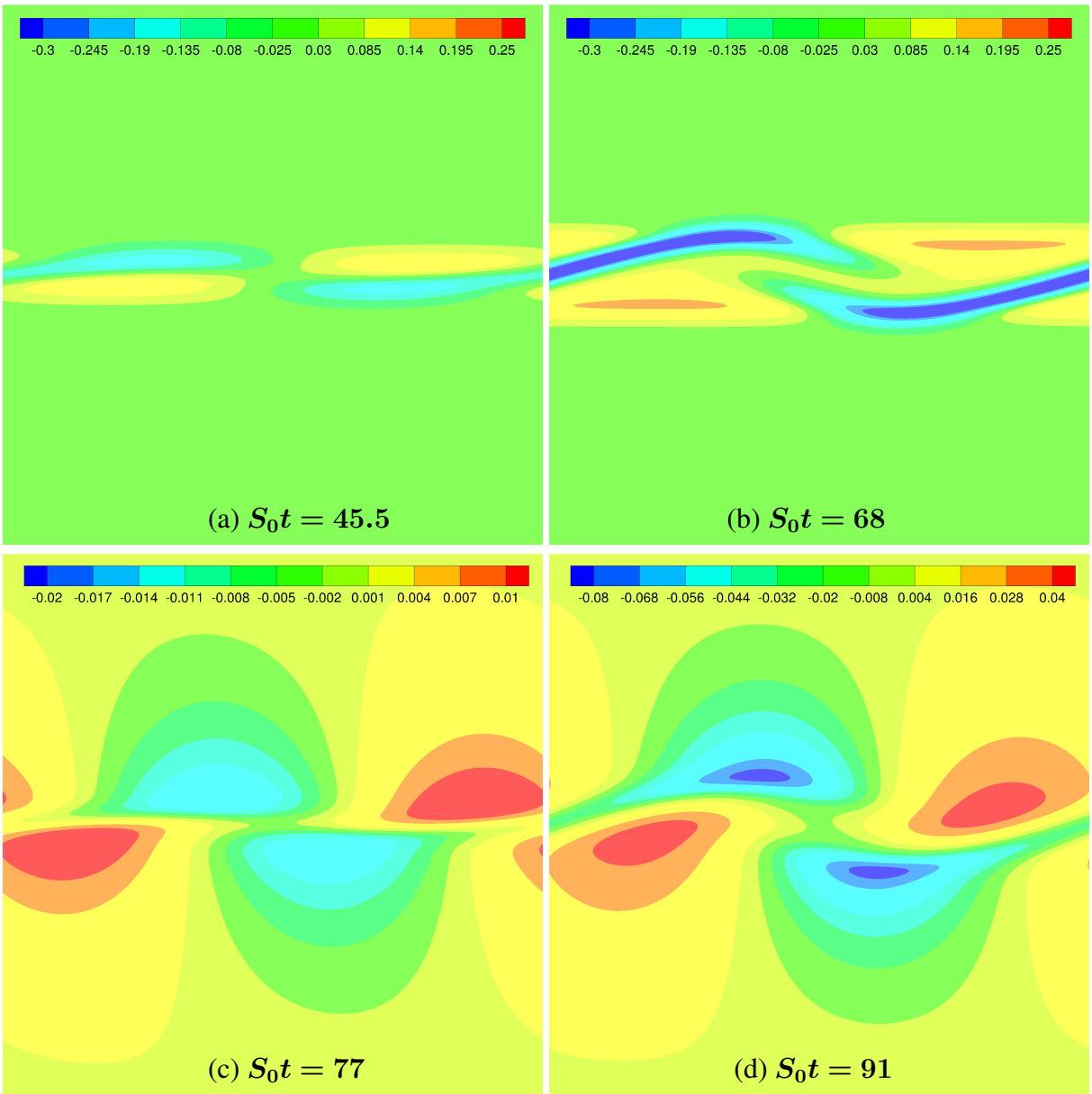

Figure 5.17: *Intermediate regime*, $R_{A0} = 0.078$: (a), (b) Spanwise vorticity and (c), (d) fluid gauge pressure.

rollup without any merger interrupting the formation of primary vortex, as seen in figure 5.17(b) at $S_0 t = 91$.

Magnetic field evolution. $B_2^{'}$ at P increases slowly due to transfer from $u_2^{'}$ (figure 5.16a) giving rise to magnetic stretching production of $B_1^{'}$. The inhomogeneities in magnetic field build up more gradually due to the slow growth of $B_1^{'}, B_2^{'}$. The weak development of inhomogeneities in magnetic field delays the onset of resistive instability.

Equipartition. This regime has reduced perturbation production and increased $u_2^{'} - B_2^{'}$ interaction compared to the weak field regime. Φ_b for various intermediate regime cases with $R_{A0} = 0.039 - 0.11$ plotted in figure 5.16(b) demonstrate a slow trend towards equipartition of velocity and magnetic fields.

Overall, this regime experiences a short-lived initial perturbation growth stage similar to the hydrodynamic case. However, the second stage of vortex merger and primary vortex formation is disrupted by the development of a high pressure region at the pivot point. Thus, the KH instability does not fully develop in this regime of magnetic field.

6. THE EFFECT OF COMPRESSIBILITY ON MAGNETOHYDRODYNAMIC PLANAR JETS

The objective of this chapter is to investigate the effects of compressibility and magnetic field on energy interactions between pressure, velocity and magnetic fields and the consequent outcome on the stability of planar jets. First we present the simulation setup and validation of implementation of MGKM to incompressible turbulent jets. Then the various energy exchange mechanisms amongst perturbation pressure, velocity and magnetic energies are examined at different Mach number and magnetic field regimes.

6.1 Simulation setup

The setup for numerical simulations is shown in figure 6.1. The simulation is initialized with both the background velocity and magnetic fields along the streamwise direction. The mean velocity field is specified using the following tangent hyperbolic function (da Silva & Métais, 2002; da Silva & Pereira, 2008):

$$U_1(x_2) = \frac{U_0}{2}\left(1 + \tanh\left(\frac{b}{a} - \frac{|x_2|}{a}\right)\right), \tag{6.1}$$

where, b, a are the half-width of the jet and thickness of shear layer between jet and the freestream. The magnetic field is imposed at all times and is of uniform strength throughout the domain. The flow is considered to be periodic along streamwise and spanwise directions and zero gradient is applied at the normal boundaries.

6.1.1 Relevant parameters

The parameters of relevance in a compressible MHD planar jet are examined in this section. The strength of applied magnetic field is assessed using Alfvén Mach number, M_A and the ratio of

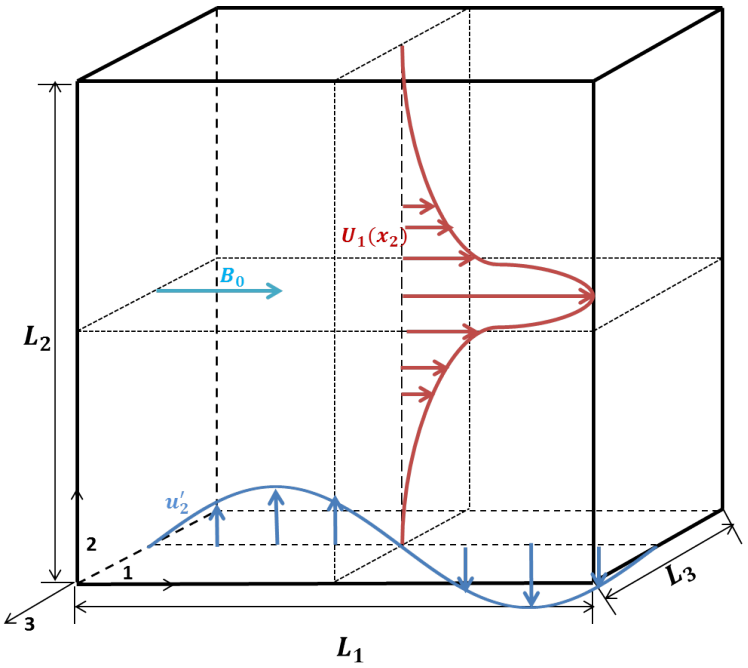

Figure 6.1: Schematic of planar jet.

shear-to-magnetic timescales, $R_{A,min}$, at the maximum shear:

$$M_A = \frac{V_A}{U_0}; \qquad V_A \equiv \frac{B_0}{\sqrt{\rho\mu_0}}; \qquad R_{A,min} \equiv \frac{V_A \kappa}{S_{max}}. \tag{6.2}$$

The subscript 'min' refers to the fact that this is the location of minimum magnetic-to-shear timescale. The effect of compressibility is characterized via convective Mach number defined as:

$$M = \frac{U_0}{c}; \qquad c \equiv \sqrt{\frac{\gamma p}{\rho}}. \tag{6.3}$$

The fluid and magnetic Reynolds numbers, Re and Re_m, for the single-mode studies are defined based on the shear layer thickness of the jet as follows:

$$Re \equiv \frac{\rho_0 U_0 a}{\mu_f}; \qquad Re_m \equiv \sigma\mu_0 U_0 a. \tag{6.4}$$

Here, μ_f is the dynamic viscosity of the fluid. For simulations with random, isotropic initial conditions, mass flow rate of the jet is used to define the Reynolds number as follows:

$$Re_q \equiv \frac{q_0}{\mu_f}; \qquad q_0 \equiv \int_0^{L_2} \rho u_1 dx_2. \tag{6.5}$$

6.1.2 Validation

Validation studies are performed for the case of incompressible hydrodynamic turbulent jets by subjecting the initial velocity field given by equation (6.1) to random, isotropic initial perturbations. The MGKM code is rendered hydrodynamic by initializing all the magnetic field components to zero. This study serves as a validation for the implementation of jet configuration. Compressibility effects have been validated in previous studies of Kumar *et al.* (2014); Karimi & Girimaji (2016), where as, magnetic field implementation has been validated in Araya *et al.* (2015) as well as in Chapter 4.

Two grids, $256^3, 512^2 \times 256$, are employed to simulate planar turbulent jet at a convective Mach number of 0.3. The Reynolds number $Re_q \equiv q_0/\mu_f$ is 5000 for all the simulations. Figure 6.2 presents the self-similar velocity profiles obtained. The streamwise component of mean velocity is normalized with respect to its centerline value and the normal coordinate is normalized using the location where the mean jet velocity is half of its centerline value. Incompressible experimental data of Gutmark & Wygnanski (1976); Ramaprian & Chandrasekhara (1985) and numerical work of Stanley *et al.* (2002) at a low convective Mach number of 0.32 are used to validate the evolution of the mean velocity profiles. It can be seen that the numerical results agree well with literature.

6.1.3 Simulation cases

MHD planar jets subjected to two kinds of perturbations are analyzed: single mode perturbations and random, isotropic initial perturbations corresponding to turbulent jets. The simulation parameters for single mode cases are given in Table 6.1. For these cases, velocity is perturbed

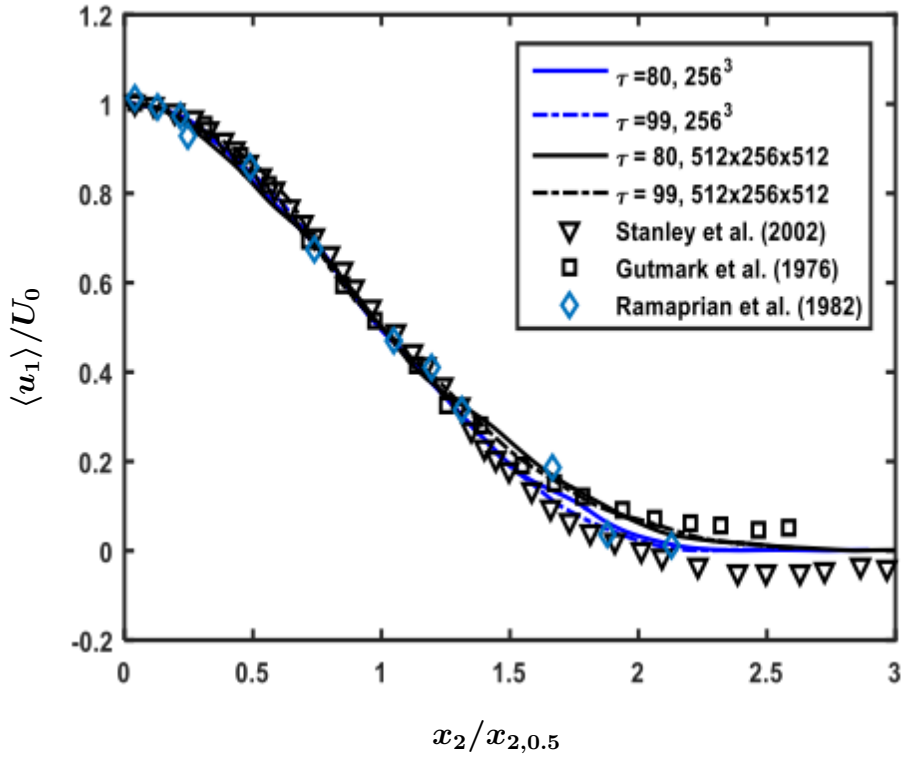

Figure 6.2: Self-similar planar jet profiles compared against experimental and numerical data at $M = 0.3$.

along the normal direction with wavevector oriented along the streamwise direction:

$$u_2^{'}(x_1, x_2, x_3; t) = \{0.01\} \times \frac{U_0}{2} \sin\left(\frac{2\pi x_1}{L_1}\right) \tag{6.6}$$

This chosen configuration for velocity perturbation can instigate the formation of KH rollers. The simulation parameters for random, isotropic initial conditions are given in Table 6.2. The initial Taylor Reynolds number (Re_λ) for these cases is 8. Based on the values of M and M_A, the simulations in Tables 6.1 and 6.2 can be categorized into the following regimes:

1. Subsonic- and sub-Alfvénic-Mach number regime: Cases 1, 2
2. Subsonic- and super-Alfvénic-Mach number regime: Case 3, T-2
3. Supersonic- and sub-Alfvénic-Mach number regime: Case 4, 7, 8, T-4
4. Supersonic- and super-Alfvénic-Mach number regime: Case 5, 6

As the cases T-1 to T-4 are subjected to random, isotropic initial perturbations, the instabilities in the jet amplify the perturbations, eventually leading to a fully turbulent jet. Therefore, two purely hydrodynamic cases, T-1 and T-3, are examined to establish baseline hydrodynamic behavior. The change in the nature of T-1 and T-3 when subjected to super-Alfvénic magnetic field and sub-Alfvénic magnetic field, respectively, will be established using cases T-2 and T-4.

6.2 Results

The results obtained from the simulations at different Mach and Alfvén Mach numbers are categorized into four regimes in the previous section. We first present the results for the single mode perturbations. The turbulent cases are then explicated based on the findings of the single mode simulations.

6.2.1 Single mode cases

For all the four types, we present the evolution of spanwise vorticity perturbation at different regimes, as it demonstrates the growth of KH instability in planar jets. We then present the evo-

Case	$M = U_0/a$	$M_A = V_A/U_0$	$R_{A,min}$	Re_a	$Re_{m,a}$	Grid resolution
1	0.3	0.023	5E-3	250	0.14	$256^2 \times 4$
2	0.3	0.23	5E-2	250	0.14	$256^2 \times 4$
3	0.3	3.926	0.822	250	0.14	$256^2 \times 4, 512^2 \times 4$
4	1.2	0.177	0.037	250	0.14	$256^2 \times 4$
5	1.2	1.08	0.226	250	0.14	$256^2 \times 4$
6	1.2	1.08	0.226	250	14	$256^2 \times 4$
7	2.4	0.029	6E-3	250	0.14	$256^2 \times 4$
8	2.4	0.539	0.113	250	0.14	$256^2 \times 4$

Table 6.1: Simulation parameters for jets subjected to a single streamwise perturbation.

Case	$M = U_0/a$	$M_A = V_A/U_0$	$R_{A,min}$	Re_q	$Re_{m,q}$	Grid resolution
T-1	0.3	0	0	5000	2.8	128^3
T-2	0.3	3.926	0.822	5000	2.8	128^3
T-3	2.4	0	0	5000	2.8	128^3
T-4	2.4	0.539	0.113	5000	2.8	128^3

Table 6.2: Simulation parameters for jets subjected to random, isotropic initial perturbations. $Re_\lambda(t = 0) = 8$ for all the cases.

lution of perturbation kinetic, magnetic and internal energies and highlight the dominant energy exchanges present in each regime.

Notation. For all the results presented in this section, time is normalized using $S \equiv U_0/2a$. Perturbation kinetic, magnetic energies and pressure variance denoted by $\mathcal{K}$, $\mathcal{B}$ and $\mathcal{P}$ are normalized using the initial energy in velocity perturbations, $\mathcal{K}_0$. Perturbation vorticity is normalized using U_0/a.

6.2.1.1 Subsonic- and sub-Alfvénic-Mach number regime

As discussed in the previous section, cases 1 and 2 fall under this regime. We first present the vorticity perturbation contours at $St = 27, 54, 68$ and 81 for cases 1 and 2 in figures 6.3 and 6.4. Then, the evolution of perturbation energies is presented in figures 6.5, 6.6.

Spanwise Vorticity. In figures 6.3(a),6.4(a) at $St = 27$, the formation of precursor vortices is

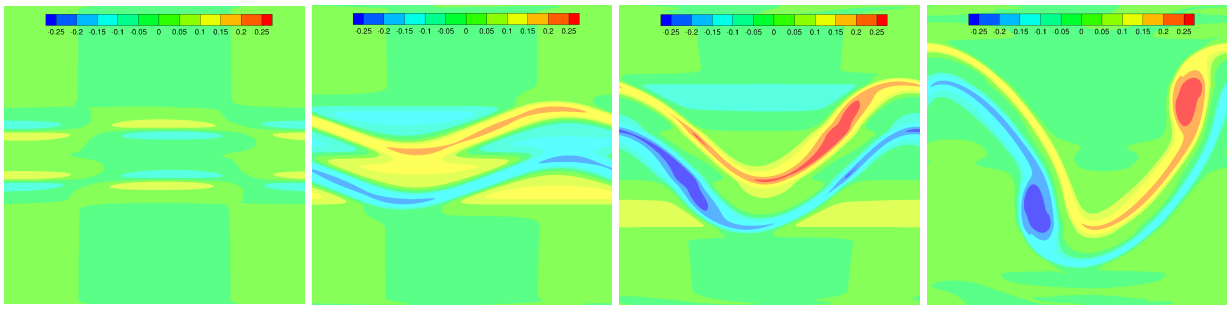

(a) $St = 27$ (b) $St = 54$ (c) $St = 68$ (d) $St = 81$

Figure 6.3: Case 1 - $M = 0.3$, $R_{A,min} = 5E-3$: Spanwise vorticity perturbation.

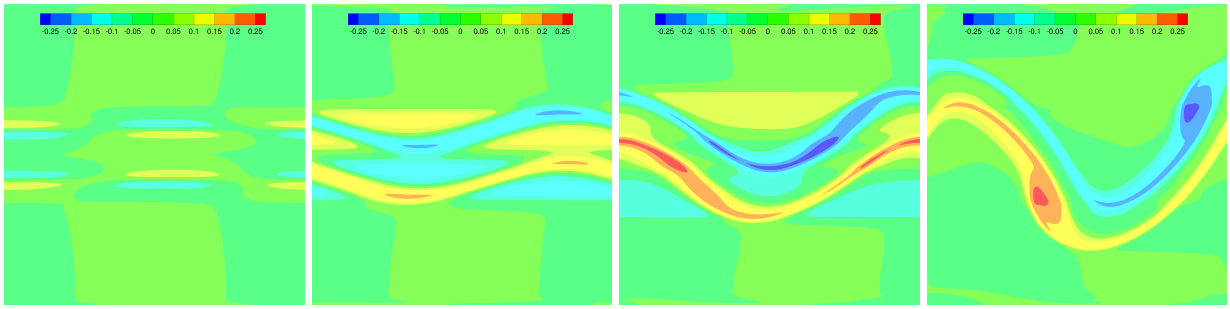

(a) $St = 27$ (b) $St = 54$ (c) $St = 68$ (d) $St = 81$

Figure 6.4: Case 2 - $M = 0.3$, $R_{A,min} = 5E-2$: Spanwise vorticity perturbation.

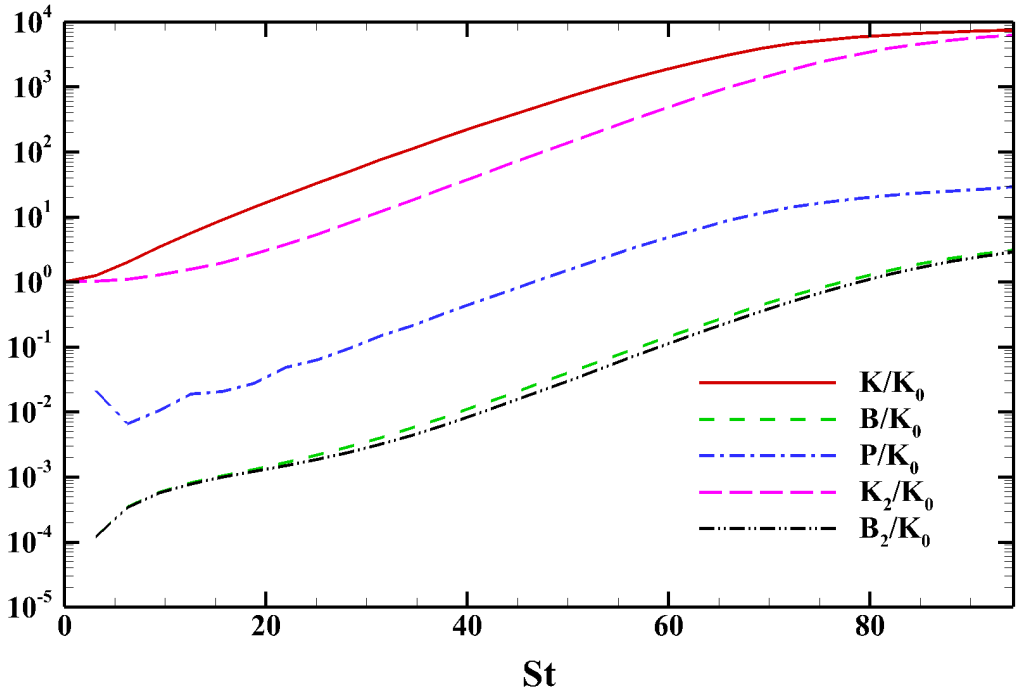

Figure 6.5: Case 1 - $M = 0.3$, $R_{A,min} = 5E-3$: Perturbation energy evolution.

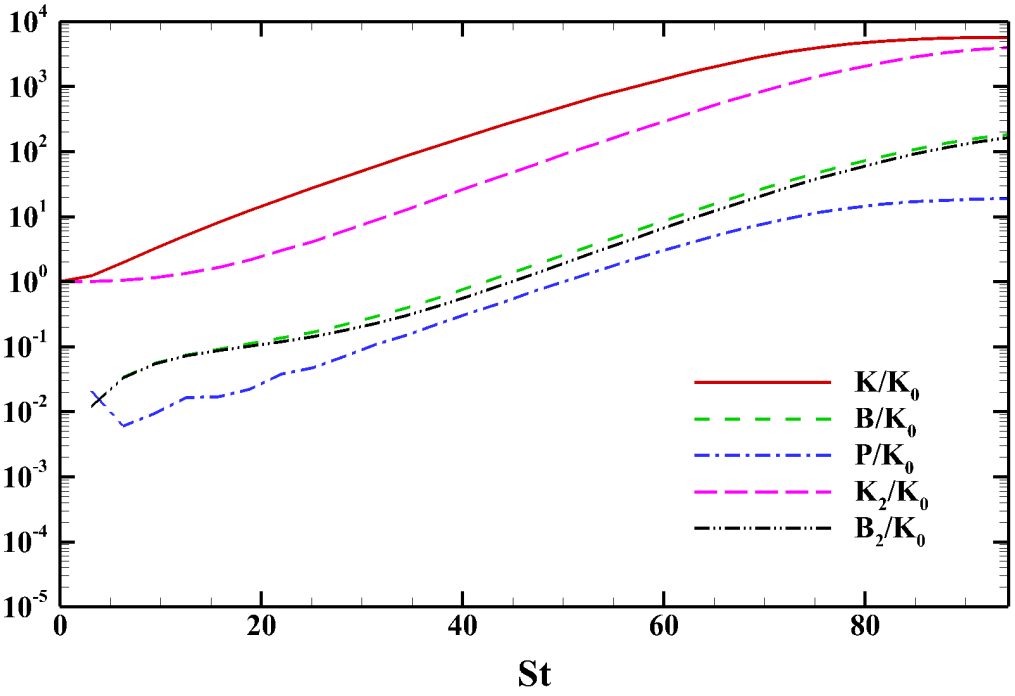

Figure 6.6: Case 2 - $M = 0.3, R_{A,min} = 5E-2$: Perturbation energy evolution.

seen at both bottom and top shear layers (jet-ambient fluid interface). At $St = 54$ (figures 6.3,6.4 b), the precursor vortices merge, leading to accelerated spreading of the jet as seen in figures 6.3,6.4 (c),(d). This accelerated spreading is due to the intensification of high and low pressure regions in the top and bottom shear layers leading to a net force in the negative normal direction. In case 2, the presence of a slightly higher magnetic field compared to case 1 results in a slightly reduced spreading of the jet.

Energy interactions. In case 1, as significant stabilizing influences due to magnetic field and compressibility are absent, due to flow instabilities the perturbation kinetic energy grows to three orders of magnitude larger than the initial value before saturating (at $St \approx 70$). Due to the presence of a weak imposed magnetic field, the exchange between perturbation kinetic and magnetic energies is slow leading to lower magnetic energy levels. Internal energy, owing to moderate levels of compressibility, is two orders of magnitude lower than kinetic energy. For case 2, kinetic energy is slightly reduced compared to case 1, due to the presence of higher magnetic

field. Magnetic perturbation energy also grows to values that are comparable to that of the internal energy. The evolution of internal energy remains relatively unchanged compared to case 1.

Overall, in this regime, the jet is susceptible to KH instability and kinetic energy grows to values that are three orders of magnitude higher than that of the initial value before saturation. Significant energy interactions between pressure, velocity and magnetic fields are absent.

6.2.1.2 Subsonic- and super-Alfvénic-Mach number regime

Case 3 with $M = 0.3, M_A = 3.926$ falls under this regime. The evolution of spanwise vorticity perturbation at $St = 5.4, 11, 14$ and 19 is shown in figure 6.7. The evolution of perturbation kinetic, magnetic and internal energies are shown in figure 6.8.

Spanwise vorticity. The formation of precursor vortices is seen in figure 6.7(a) at $St = 5.4$, similar to that seen in the *Subsonic- and sub-Alfvénic-Mach number* regime. However, the sign of vorticity in the precursor vortices changes without any merger at $St = 11, 14$. At $St = 19$, the precursor vortices dissipate as the perturbation kinetic energy exchanged with magnetic field is dissipated in Joule heat. Therefore, KH instability in this regime is suppressed and perturbations are dissipated.

Energy interactions. Due to the presence of a strong magnetic field, the harmonic exchange between perturbation kinetic and magnetic energies is quick. This results in equipartition of kinetic and magnetic energies at initial times as seen in figure 6.8. Perturbation internal energy does not grow to the same intensities as the previous regime and decays as kinetic energy is decaying.

Overall, in this regime, KH instability is eliminated owing to rapid harmonic exchange between perturbation kinetic and magnetic energies. As magnetic Reynolds number is low, the energy transferred from kinetic to magnetic energy is dissipated as Joule heat. This results in the decay of internal energy as well.

6.2.1.3 Supersonic- and sub-Alfvénic-Mach number regime

We now present the results for cases 4, 7 and 8 with $M = 1.2, M_A = 0.177$; $M = 2.4, M_A = 0.029$ and $M = 2.4, M_A = 0.539$. Spanwise vorticity perturbation contours for case 4 at $St =$

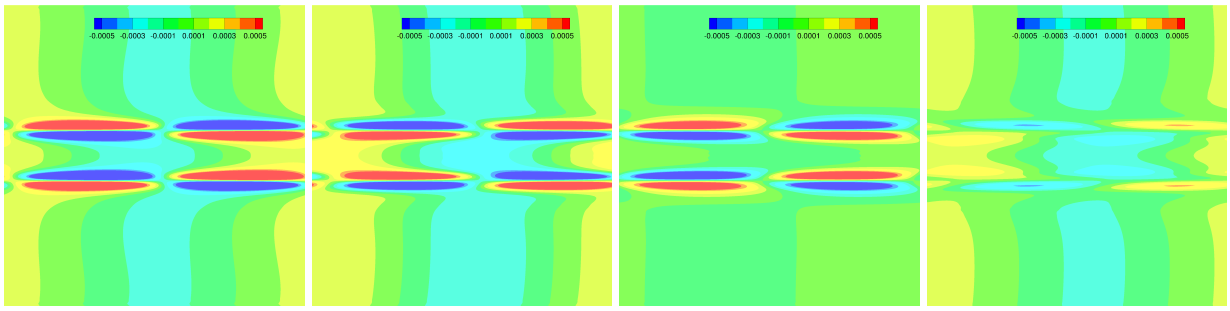

(a) $St = 5.4$ (b) $St = 11$ (c) $St = 14$ (d) $St = 19$

Figure 6.7: Case3 - $M = 0.3$; $R_{A,min} = 3.926$: Spanwise vorticity perturbation.

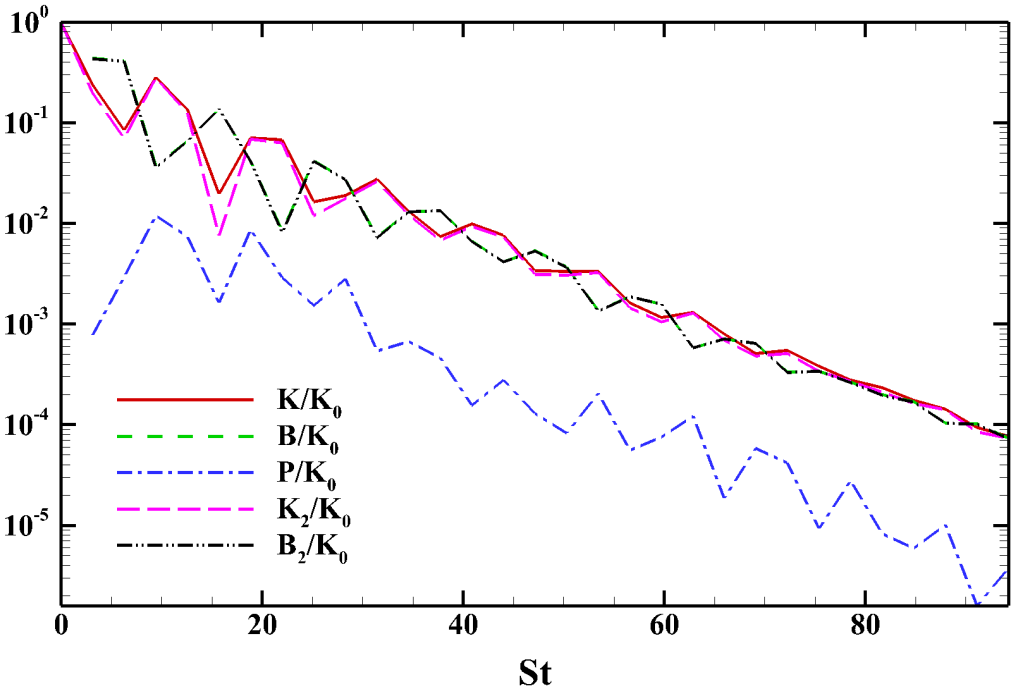

Figure 6.8: Case3 - $M = 0.3$; $R_{A,min} = 3.926$: Perturbation energy evolution.

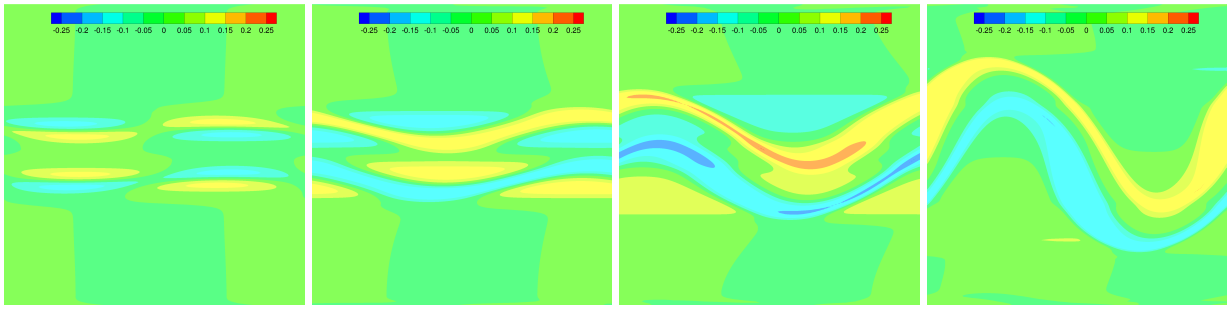

(a) $St = 41$ (b) $St = 57$ (c) $St = 73$ (d) $St = 89$

Figure 6.9: Case4 - $M = 1.2$; $R_{A,min} = 0.037$: Spanwise vorticity perturbation.

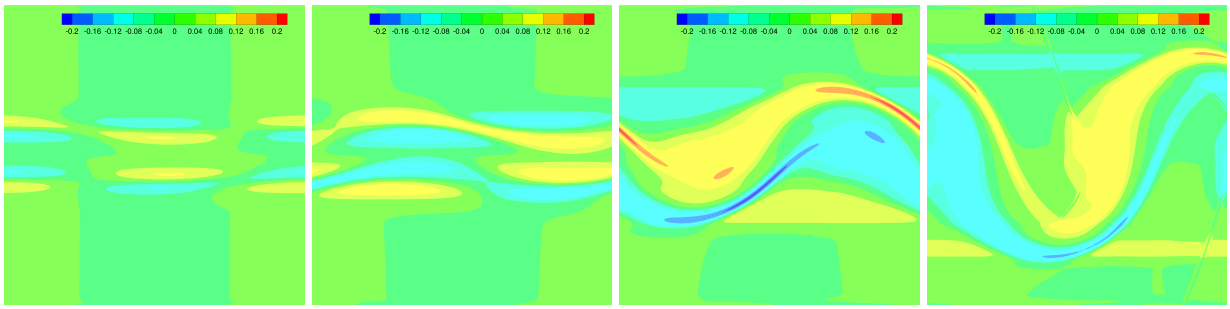

(a) $St = 54$ (b) $St = 75$ (c) $St = 108$ (d) $St = 130$

Figure 6.10: Case 7 - $M = 2.4$; $R_{A,min} = 6E - 3$: Spanwise vorticity perturbation.

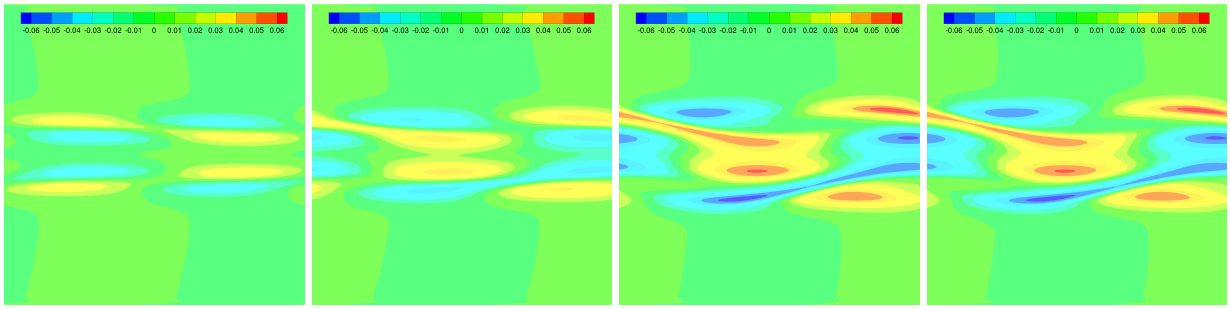

(a) $St = 54$ (b) $St = 75$ (c) $St = 109$ (d) $St = 217$

Figure 6.11: Case 8 - $M = 2.4$; $R_{A,min} = 0.113$: Spanwise vorticity perturbation.

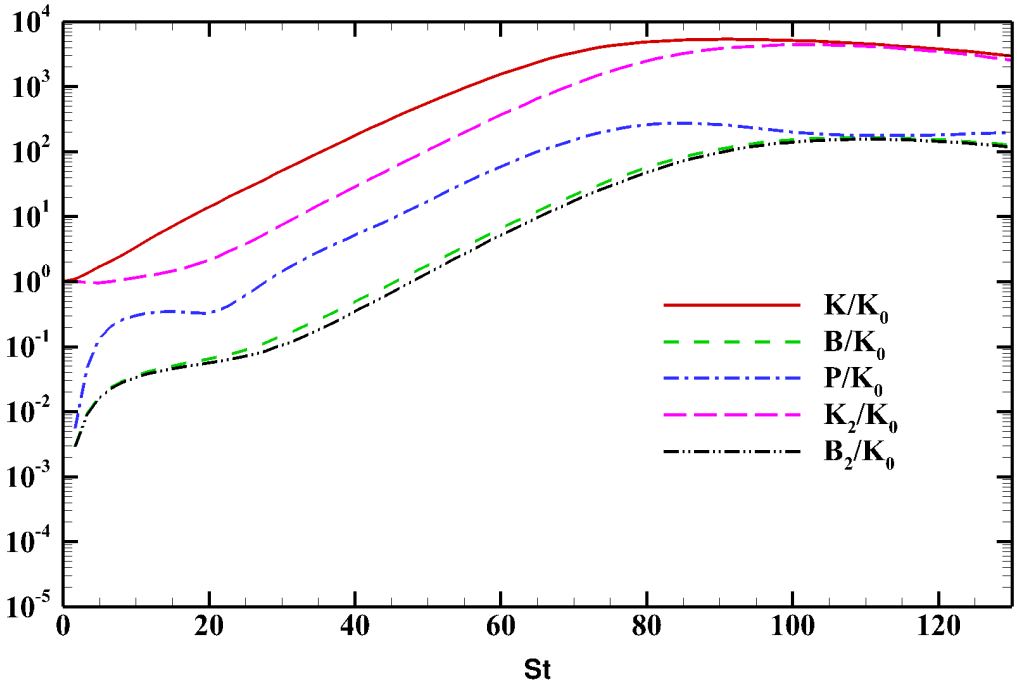

Figure 6.12: Case4 - $M = 1.2$; $R_{A,min} = 0.037$: Perturbation energy evolution.

$41, 57, 73$ and 89 are presented in figure 6.9. Spanwise vorticity contours at $St = 54, 76, 108$ and 130 for case 7 are given in figure 6.10. For case 8, the evolution of spanwise vorticity is presented in figure 6.11 at $St = 76, 108, 130$ and 217. The evolution of perturbation energies are given in figures 6.12, 6.13 and 6.14.

Vorticity evolution. At $St = 41$ in figure 6.9(a) for case 4, the formation of precursor vortices can be seen. In figures 6.9b- 6.9d, these precursor vortices merge and spread along the normal direction similar to that seen in the previous regime. However, the spreading rate and intensity of spanwise vorticity is reduced compared to the *subsonic-, sub-Alfvénic Mach number* regime. This is owing to the increase in the sonic Mach and Alfvénic Mach number resulting in a reduction in the production of perturbations. For cases 7 and 8 in figures 6.10 and 6.11, the precursor vortex merger is considerably delayed compared all the previous cases of 1-4, i.e., vortex merger does not occur until $St = 75$. The intensity of vorticity perturbation and spreading rate are also considerably reduced.

Energy interactions. In case 4, perturbation kinetic energy saturates at values that are slightly lower than those of cases 1 and 2. However, internal and magnetic energies assume values that are an order of magnitude higher. Similar evolution of kinetic and internal energies are seen even for case 7 in figure 6.13. However, magnetic energy in this case ($R_{A,min} = 5E-3$) is comparable to that of case 1 ($R_{A,min} = 6E-3$), implying that the transfer between velocity and magnetic fields is dependent on the parameter, R_A. In case 8 shown in figure 6.14, the growth of kinetic energy is considerably reduced, almost equipartition is evident between kinetic energy in the normal component and internal energies. However, the energies seem to grow monotonically at a reduced growth rate compared to all the previous cases.

Overall, the instability in this regime is not fully eliminated. Internal energies in this regime grow to values that are almost comparable to that of kinetic energy. The growth of magnetic energy seems to be dependent on the value of $R_{A,min}$.

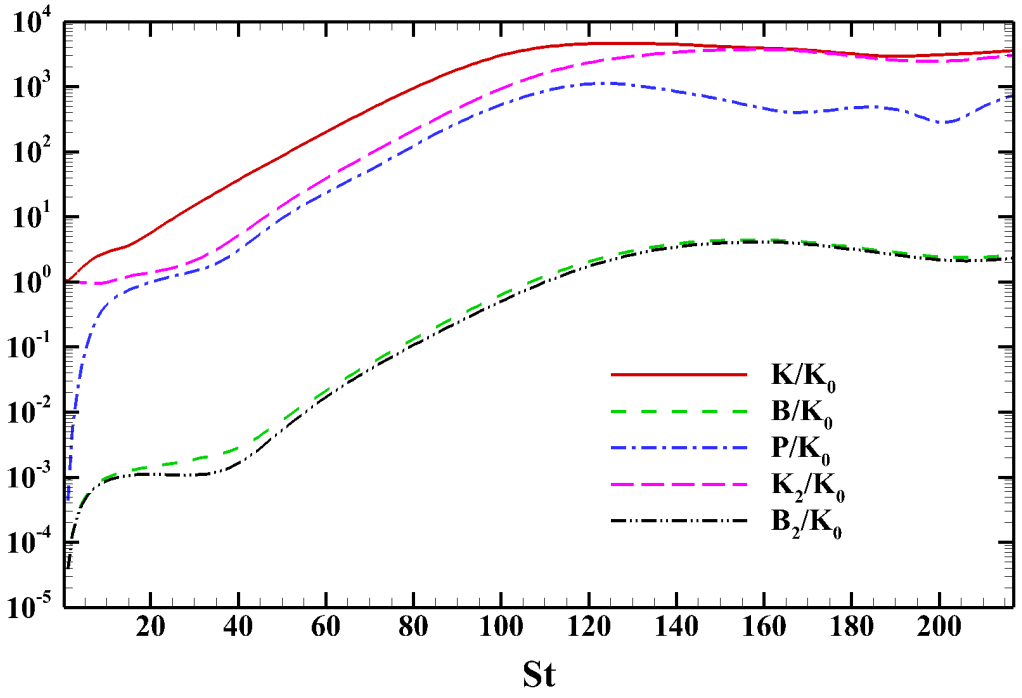

Figure 6.13: Case7 - $M = 2.4$; $R_{A,min} = 6E - 3$: Perturbation energy evolution.

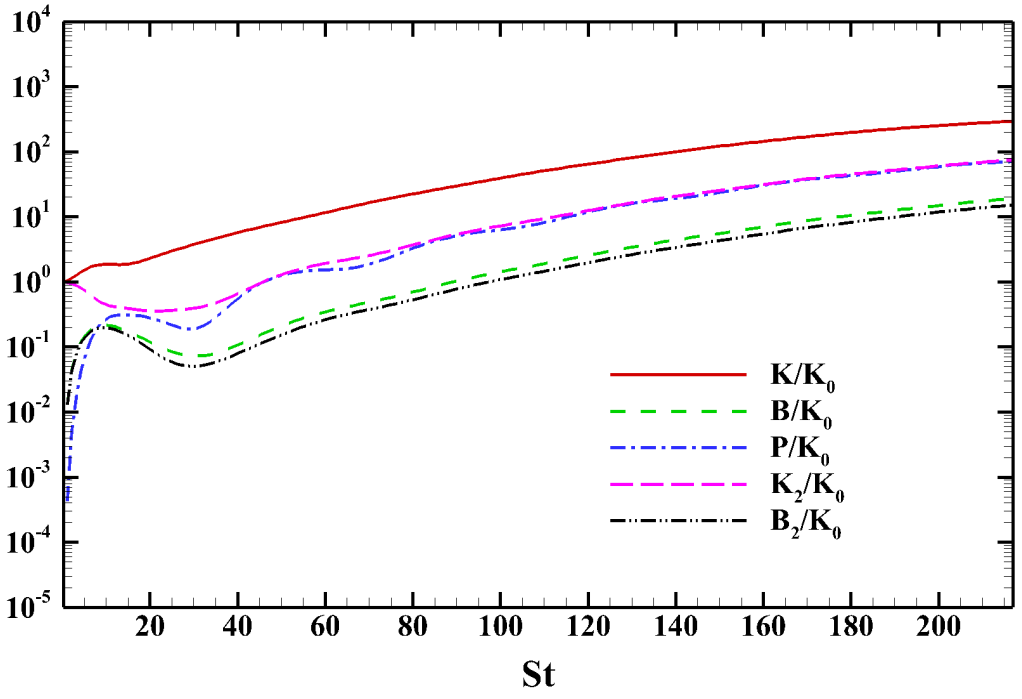

Figure 6.14: Case 8 - $M = 2.4$; $R_{A,min} = 0.113$: Perturbation energy evolution.

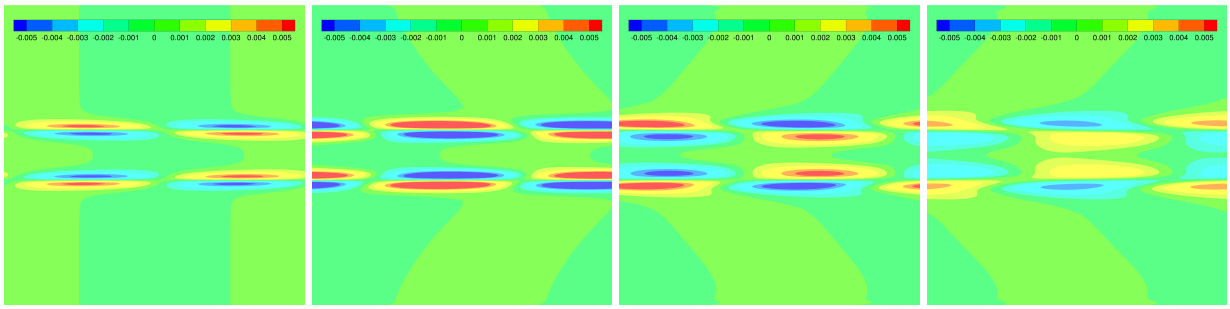

(a) $St = 1.6$ (b) $St = 16.2$ (c) $St = 65$ (d) $St = 130$

Figure 6.15: Case 5 - $M = 1.2$; $R_{A,min} = 0.226$; $Re_m = 0.14$: Spanwise vorticity perturbation.

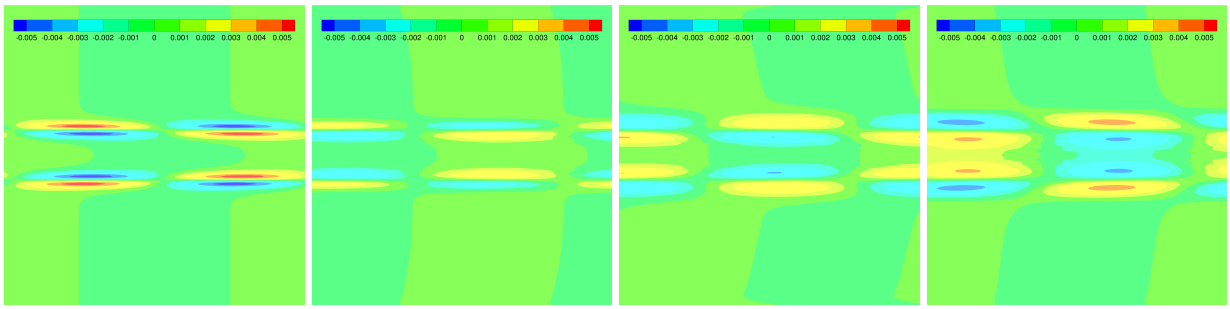

(a) $St = 1.6$ (b) $St = 16.2$ (c) $St = 65$ (d) $St = 130$

Figure 6.16: Case 6 - $M = 1.2$; $R_{A,min} = 0.226$; $Re_m = 14$: Spanwise vorticity perturbation.

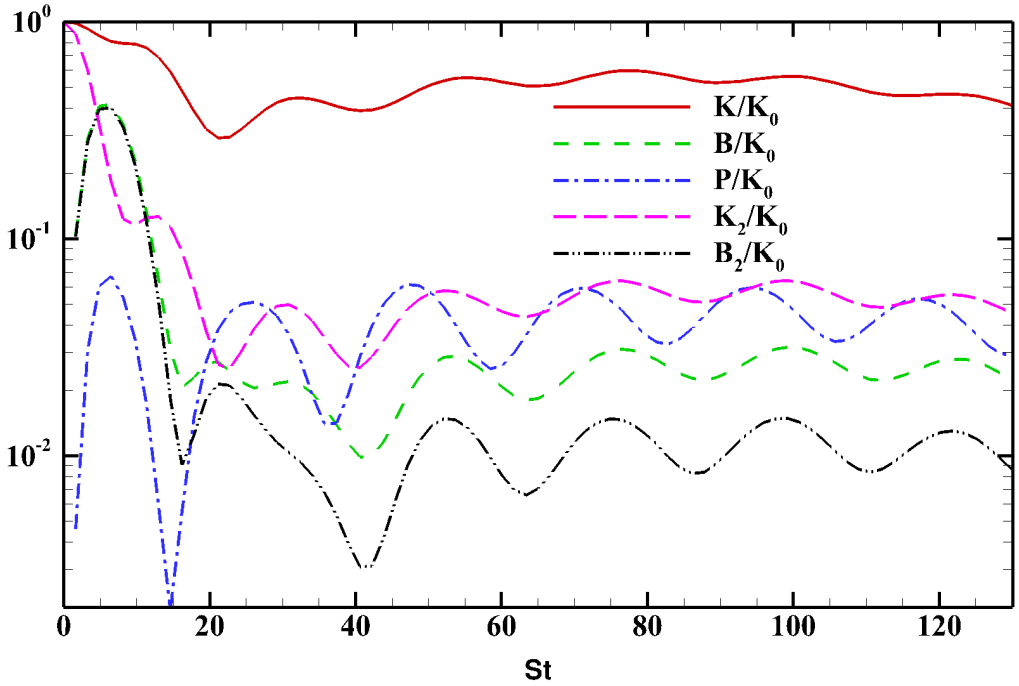

Figure 6.17: Case 5 - $M = 1.2$; $R_{A,min} = 0.226$; $Re_m = 0.14$: Perturbation energy evolution.

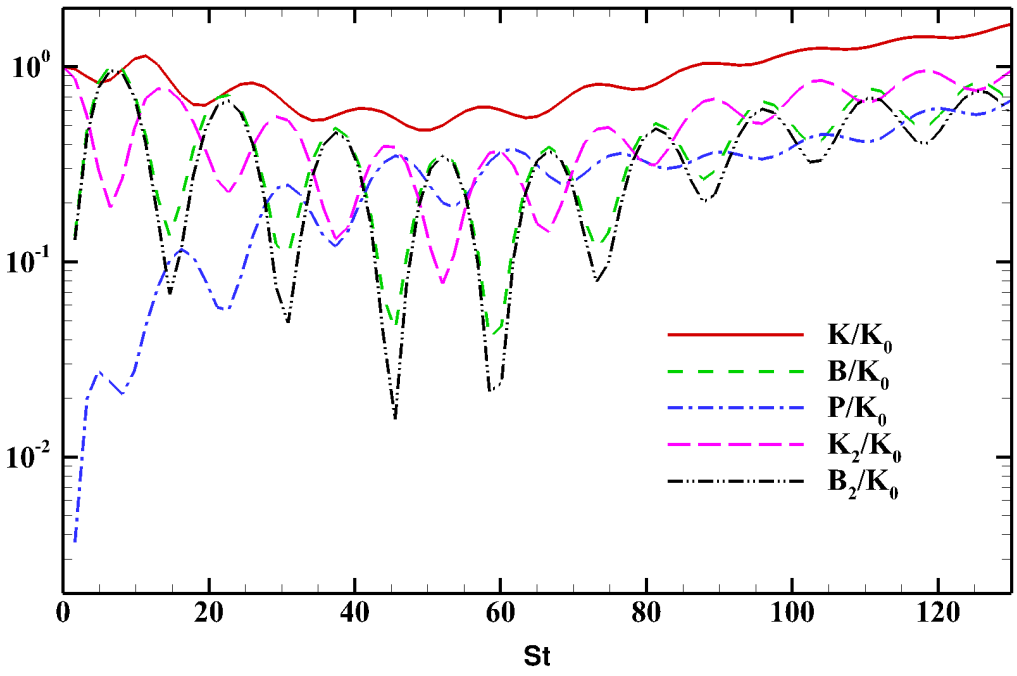

Figure 6.18: Case 6 - $M = 1.2$; $R_{A,min} = 0.226$; $Re_m = 14$: Perturbation energy evolution.

6.2.1.4 Supersonic- and super-Alfvénic-Mach number regime

Vorticity contours at $St = 1.6, 16, 65$ and 130 for $M = 1.2, M_A = 1.08$ at $Re_m = 0.14, 14$ are shown in figures 6.15 and 6.16. The evolution of various energies for these cases are given in figures 6.17 and 6.18.

Spanwise vorticity. Similar to case 3, precursor vortices form but never merge in this regime, as seen in figures 6.15,6.16 (a)-(d). Due to the action of resistivity, the magnitude of vorticity in case 5 with $Re_m = 0.14$ is reduced with time. However for case 6 with $Re_m = 14$, even though the vorticity is reduced at $St = 16.2, 65$, it grows again at $St = 130$.

Energy interactions. In case 5, the rapid harmonic exchange between kinetic and magnetic energies results in the eventual decay of kinetic and magnetic energies. As the Mach number in this case is high, internal energy also builds up to similar energy levels as that of kinetic energy in the normal component. At late times, all the energies seem to have saturated at values lower

than the initial value of perturbation kinetic energy. In case 6 with $Re_m = 14$, the magnetic energy does not decay as much and maintains similar energy levels as those of internal energy and kinetic energy in the normal component.

Overall in this regime, KH instability is eliminated due to the presence of a strong magnetic field.

6.2.1.5 Equipartition

Linear analysis performed in Section 2.2.2.1 indicates that if the magnetic stretching production of B_1' is minimal, the normal component of kinetic energy should equipartition with the sum of magnetic and internal energies. The validity of this inference is investigated for cases 5 and 6 where the magnetic field is strong enough to eliminate magnetic stretching production. Figure 6.19 shows the evolution of kinetic energy in the normal component compared against the sum of magnetic and internal energies for case 5 with $Re_m = 0.14$. Equipartition between the two energies is clearly exhibited. As Re_m is increased to 14 in figure 6.20, there is an evidence of clear equipartition at early times. At late times, the energies seem to be out-of-phase with each other. However, the sum of magnetic and internal energies is greater in magnitude compared to the kinetic energy owing to magnetic production. Evidence of equipartition at early times is also seen for case 8 with $M = 2.4, M = 0.5$ in figure 6.21. However, as seen in figure 6.11, the flow is not fully stable and this is evident from the continuous growth of kinetic, internal and magnetic energies. At late times, as seen in case 6, the sum of magnetic and internal energies slightly overshoots kinetic energy in the normal component owing to magnetic stretching production.

6.2.2 Random isotropic initial conditions

The simulation parameters for various random isotropic initial perturbation simulations are shown in Table 6.2. Results for each of these cases are presented below. The vortex flow structure computed by taking the curl of the full velocity field is presented first. Then, volume averaged fluctuating kinetic energy, $\mathcal{K}/\mathcal{K}_0$, magnetic energy, $\mathcal{B}/\mathcal{K}_0$, and pressure variance, $\mathcal{P}/\mathcal{K}_0$, are shown.

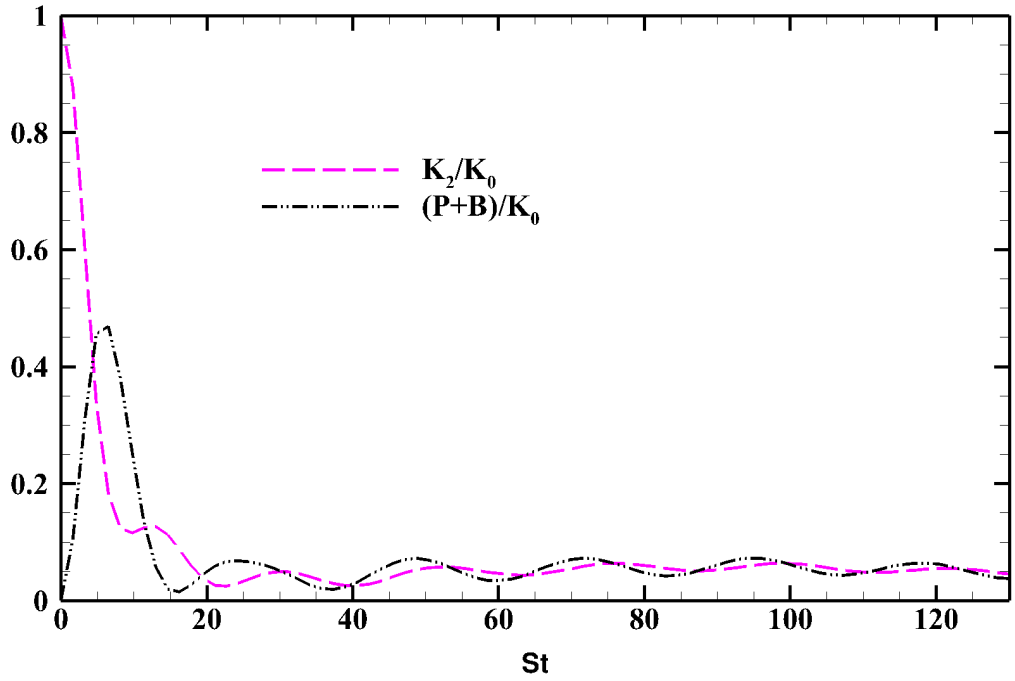

Figure 6.19: Case 5 - $M = 1.2; R_{A,min} = 0.226; Re_m = 0.14$: Evolution of $\mathcal{K}_2$ compared against $\mathcal{P} + \mathcal{B}$.

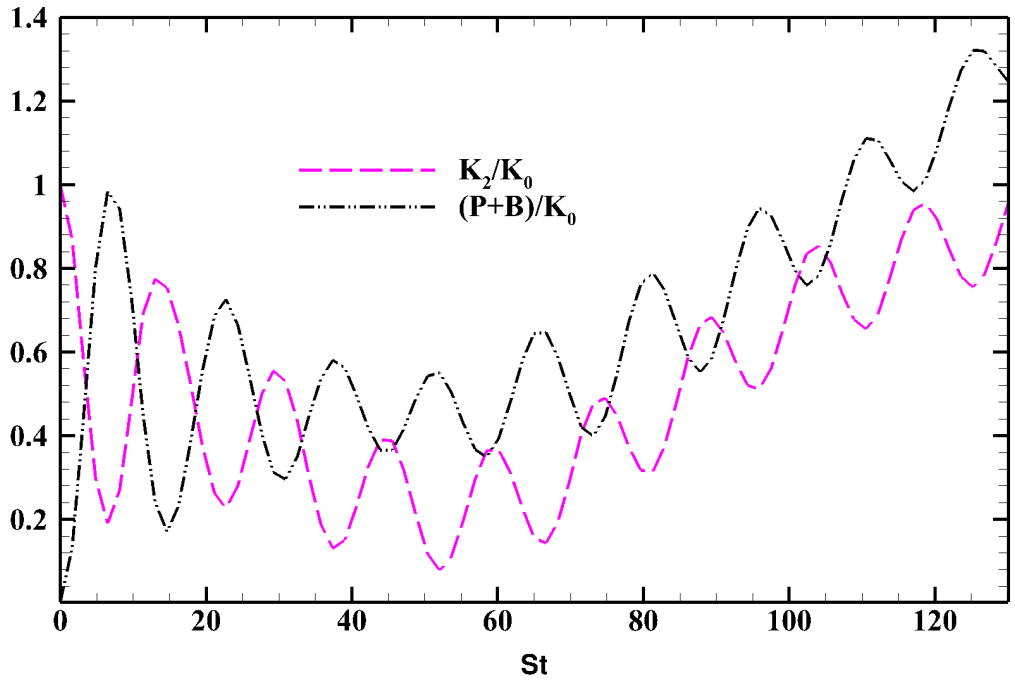

Figure 6.20: Case 6 - $M = 1.2; R_{A,min} = 0.226; Re_m = 14$: Evolution of $\mathcal{K}_2$ compared against $\mathcal{P} + \mathcal{B}$.

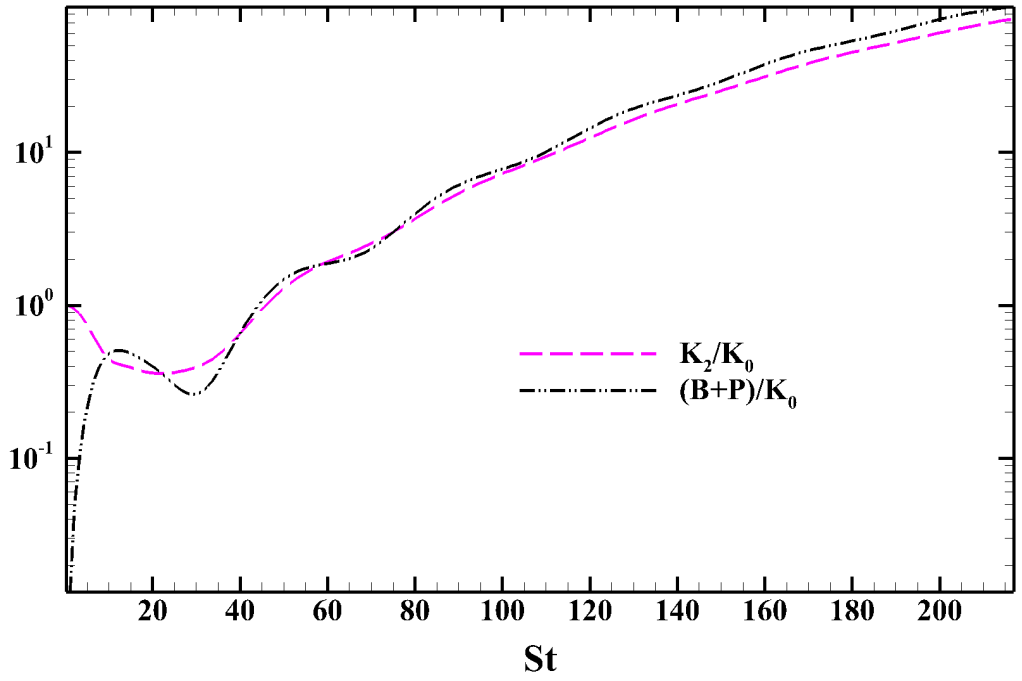

Figure 6.21: Case 8 - $M = 2.4$; $R_{A,min} = 0.113$: Evolution of $\mathcal{K}_2$ compared against $\mathcal{P} + \mathcal{B}$.

6.2.2.1 Subsonic hydrodynamic jet

The contours of spanwise vorticity for the case T-1 are presented in figure 6.22. The evolution of $\mathcal{K}$, $\mathcal{P}$ and $\mathcal{K}_2$ are presented in figure 6.23. The formation of typical KH spanwise rollers can be seen in figure 6.22a at $St = 50$. During this stage, the turbulent kinetic energy grew exponentially as seen in figure 6.23. Pressure variance is three orders of magnitude smaller than the turbulent kinetic energy as the Mach number is low. Beyond, $St = 60$, the growth in $\mathcal{K}$ and $\mathcal{K}_2$ is saturated and the flow breaks down to turbulence as seen from figures 6.22(b)-(d).

6.2.2.2 Subsonic MHD jet in strong magnetic field

The initial mean and perturbation velocity field configuration in this case is similar to that of the previous case. The jet is now subjected to a strong magnetic field. KH instability rollers are completely eliminated by the action of magnetic field as seen from the spanwise vorticity contours presented in figure 6.24. The fluctuating energy evolution in figure 6.25 shows a dip in kinetic

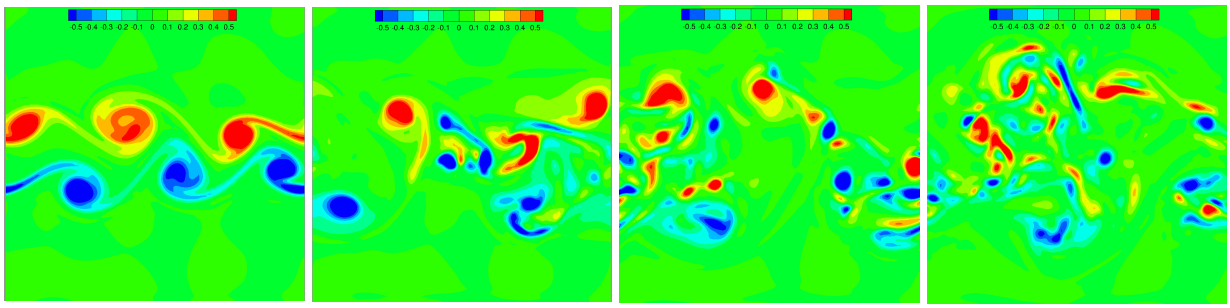

(a) $St = 50$ (b) $St = 87$ (c) $St = 106$ (d) $St = 124$

Figure 6.22: Case T1 - $M = 0.3, R_{A,min} = 0$: Spanwise vorticity.

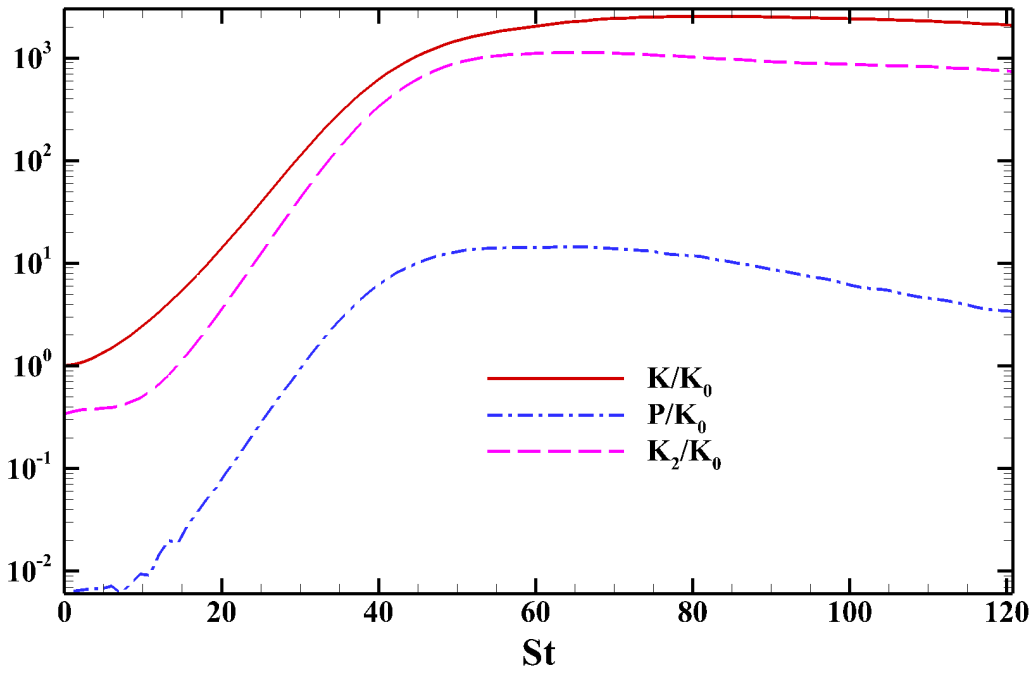

Figure 6.23: Case T1 - $M = 0.3, R_{A,min} = 0$: Fluctuation energy evolution.

energy around $St = 5$. This is due to the transfer of energy from velocity fluctuations to magnetic fluctuations. As seen in Chapter 4, the rate of transfer is maximum for streamwise wavevectors and decreases as β is increased. For spanwise wavevectors, velocity and magnetic fluctuations are decoupled. As βs in this scenario are randomly distributed, only a portion of $\mathcal{K}$ is transferred to $\mathcal{B}$. Due to a small magnetic Reynolds number, the reverse transfer from $\mathcal{B}$ to $\mathcal{K}$ is negligible and $\mathcal{B}$ is dissipated as Joule heat. The only energetic wavevectors are the ones oriented in the spanwise direction. This can be verified from the fact that $\mathcal{K}_2$ remains a constant at late times (Section 2.1.1.1). u_1' grows linearly due to production for spanwise wavevectors, leading to growth of $\mathcal{K}$ at late times. However, this growth is not manifest in figure 6.24 as the total velocity field has decayed in time via magnetic field due to Joule heating.

6.2.2.3 Supersonic hydrodynamic jet

The spanwise vortices for the case of supersonic hydrodynamic jet with $M = 2.4$ are shown in figure 6.26. The fluctuating energies are shown in figure 6.27. The intensity of perturbations considered in this case is the same as cases T-1 and T-2. It can be seen from figure 6.26 that the spanwise vorticity does not evolve into KH-like rollers. Instead, the structures are elongated forming λ-shaped vortices, which quickly breakdown to turbulence. The fluctuating kinetic energy, $\mathcal{K}$, in figure 6.27 shows that growth rate of the perturbations is considerably reduced compared to

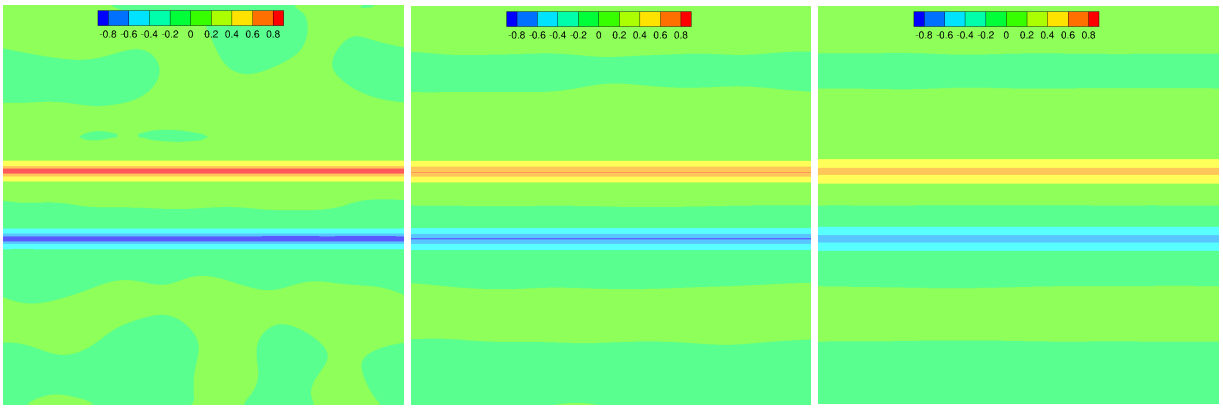

(a) $St = 1$ (b) $St = 12$ (c) $St = 50$

Figure 6.24: Case T2 - $M = 0.3, R_{A,min} = 0.822$: Spanwise vorticity.

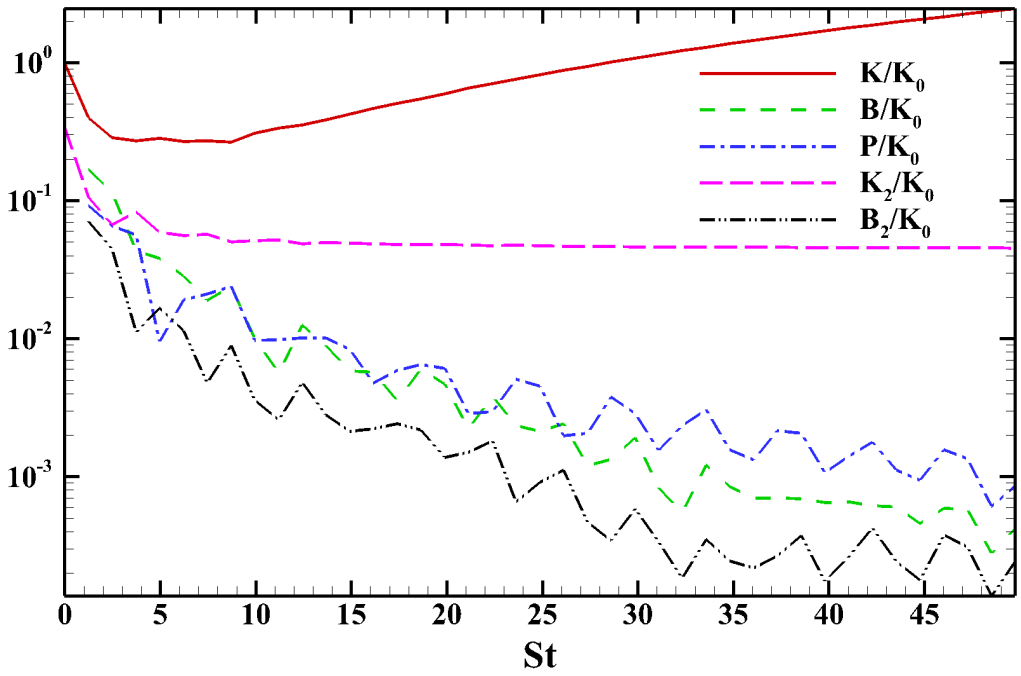

Figure 6.25: Case T2 - $M = 0.3, R_{A,min} = 0.822$: Fluctuation energy evolution.

the case T-1. However, $\mathcal{K}/\mathcal{K}_0$ asymptotes to similar values as that of T-1. Pressure variance, P, is considerably larger than that of case T-1, as anticipated and the values are closer to $\mathcal{K}_2$. However, true equipartition between $\mathcal{P}$ and $\mathcal{K}_2$ is not achieved. This is due to the presence of spanwise wavevectors that exhibit pressure-released behavior and do not exchange any energy with $\mathcal{P}$.

6.2.2.4 Supersonic MHD jet in the presence of a moderate magnetic field

The initial velocity field in this case is the same as that of the case, T-3. A moderate magnetic field with $R_{A,min} = 0.113$ is applied on the jet, which results in a more organized flow (figure 6.28) than T-3. Compared to the previous case, the fluctuating kinetic energy, $\mathcal{K}$, in figure 6.29 is reduced by two orders of magnitude. $\mathcal{K}_2$ and $\mathcal{P}$ are comparable, similar to T-3. However, when the evolutions of $\mathcal{K}_2$ and $\mathcal{P} + \mathcal{B}$ are compared, equipartition between them is not evident even at early time, unlike its singe mode counterpart, case 8. This is due to fact that some of the energy in $\mathcal{K}_2$ is resident in its spanwise wavevectors.

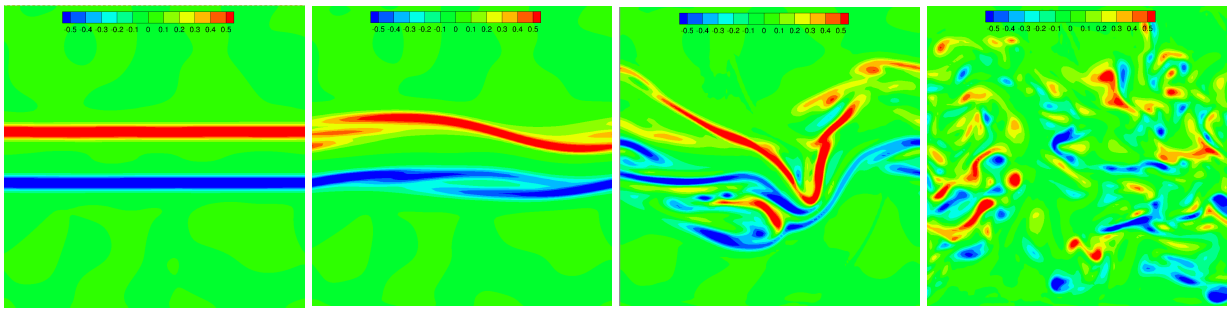

(a) $St = 5$ (b) $St = 100$ (c) $St = 150$ (d) $St = 198$

Figure 6.26: Case T3 - $M = 2.4$, $R_{A,min} = 0$: Spanwise vorticity.

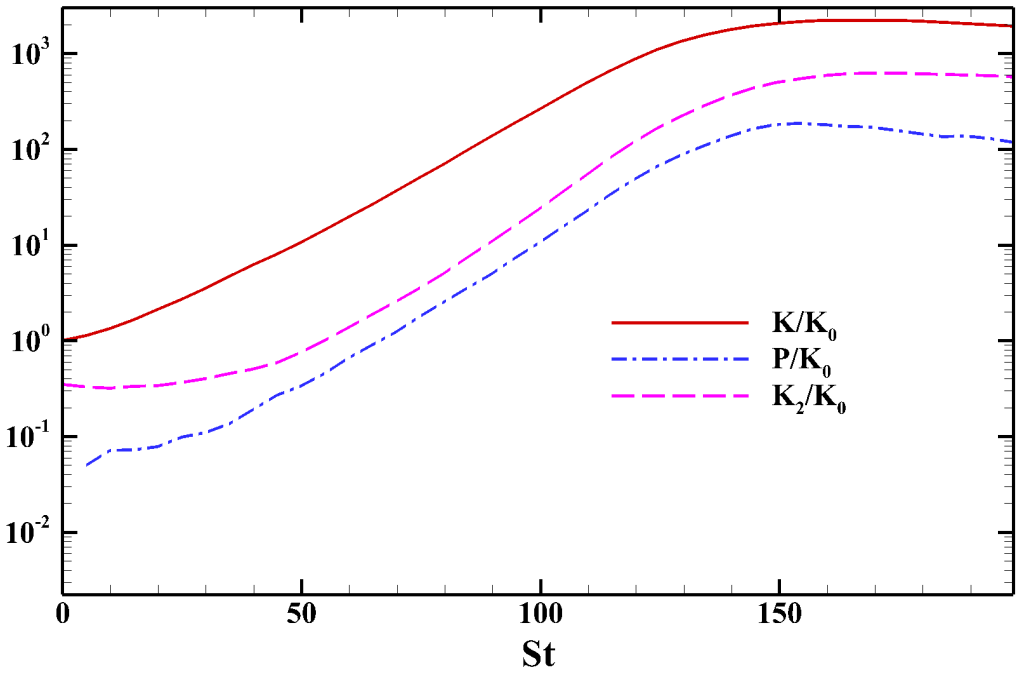

Figure 6.27: Case T3 - $M = 2.4$, $R_{A,min} = 0$: Fluctuation energy evolution.

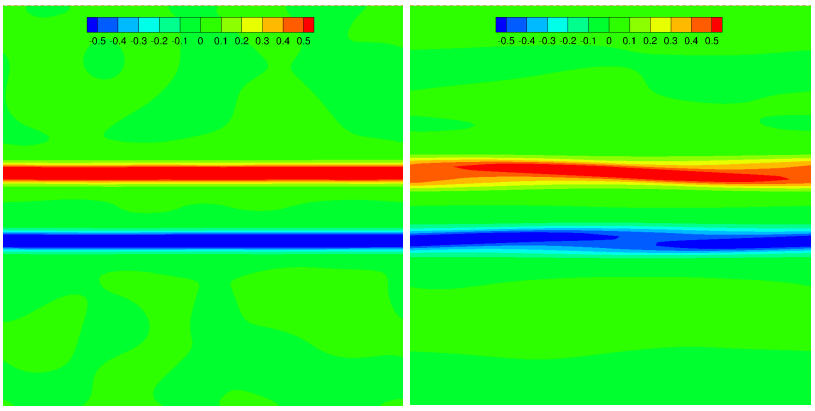

(a) $St = 5$ (b) $St = 100$

Figure 6.28: Case T4 - $M = 2.4$, $R_{A,min} = 0.113$: Spanwise vorticity.

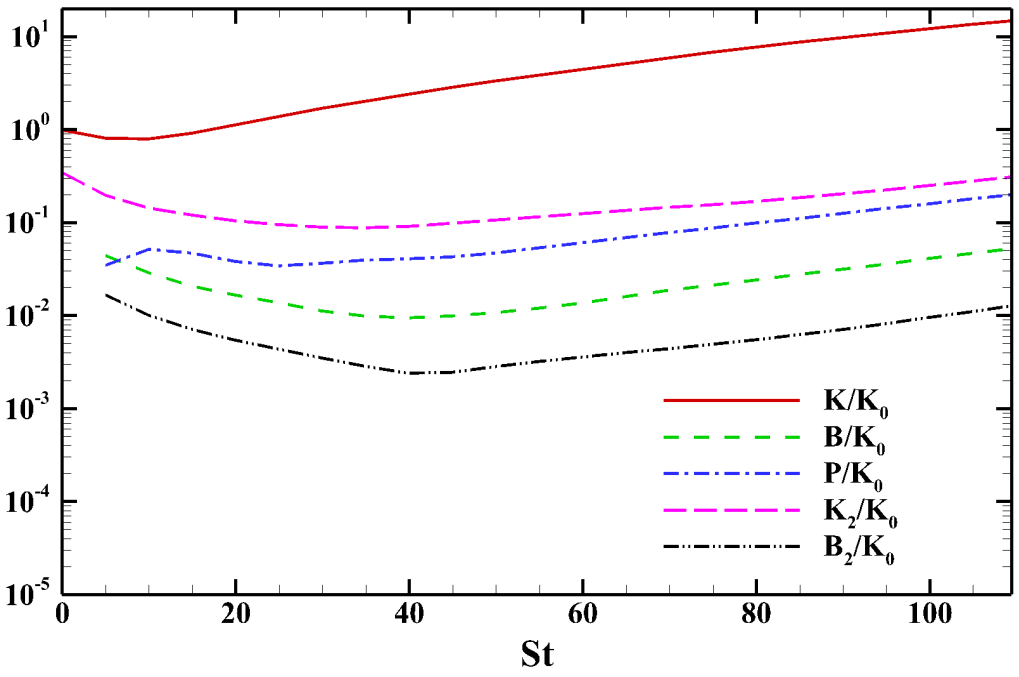

Figure 6.29: Case T4 - $M = 2.4$, $R_{A,min} = 0.113$: Fluctuation energy evolution.

7. SUMMARY AND CONCLUSIONS

While the stabilizing influences of compressibility and magnetic field have long been known, the underlying stabilizing mechanisms are not clearly established. The goal of this dissertation is to understand the stabilization mechanisms of background magnetic field on perturbation growth in incompressible and compressible planar free shear flows. Toward that end, three planar shear flows are chosen: homogeneous shear, mixing layer and planar jets. In incompressible homogeneous shear, flow is subject to algebraic instability, where as, mixing layers and planar jets are susceptible to exponential growth of perturbations. In MHD studies, each of the flows is subject to a uniform background magnetic field that is applied at all times along the flow direction to study its influence on perturbations. The applied magnetic field affects the fluid momentum by means of the Lorentz force. This is a simplified case of what is encountered in plasma propulsion applications.

For all the planar shear flows, the production of velocity and magnetic field perturbations is largely dependent on the nature of evolution of perturbations normal to the mean flow direction. As a result, these are the main drivers of the instability. If the perturbations in the normal component experience monotonic evolution, then the production is dominant. However, if the normal components are oscillatory about zero, then the perturbation production could be almost negligible. Since we are mainly interested in the behavior of velocity field, in all of the three studies only normal velocity perturbation components are initialized.

7.1 Incompressible regime - MHD Homogeneous shear

For the case of homogeneously sheared flows, the evolution of perturbations is determined by the interplay between the processes of pressure-redistribution, kinetic energy production, magnetic stretching production and harmonic-kinetic-magnetic exchange. Rapid distortion analysis reveals that the evolution of the normal velocity and magnetic field perturbations is solely determined by the parameter, $R_A \equiv V_A\kappa_0/S$ in the scaled time, $\tau^* \equiv St\cos\beta$. R_A signifies the ratio of shear-to-Alfvén frequency. Therefore, when $R_A \gg 1$, the evolution of perturbations is decided

by the Alfvén wave. This results in oscillatory evolution of normal velocity and magnetic field components and curtailed production. However, when $R_A \ll 1$, the fluid processes dominate and could result in significant growth of velocity perturbations, depending on the value of β. However at late times, as the homogeneously sheared mean flow does not result in vorticity production and a large scale instability, production and pressure redistribution eventually die out and only harmonic exchange dominates. The following is a brief summary of perturbation evolution at different R_A regimes for $\beta \in [0°, 90°)$ (when only normal velocity component is initialized):

When $\boldsymbol{R_A \ll 1}$, a three-stage evolution of perturbations is seen. As the normal velocity component evolves monotonically due to negligible harmonic exchange, positive/negative production is dominant depending on the value of β. Almost immediately, pressure redistribution also becomes active in order to satisfy incompressibility condition. During this stage, only a small amount of energy is transferred to magnetic field, resulting in a seemingly hydrodynamic behavior. This seed transfer initiates the second stage of perturbation development, where in the streamwise component of magnetic field is amplified. The amplification of magnetic perturbations goes on until the time when Alfvén-wave processes dominate which eventually result in oscillatory evolution of the normal components. As a result, in the third stage only harmonic exchange dominates and equipartition of perturbation velocity and magnetic fields is seen. Overall, the perturbation energies equipartition about a value that is greater than the initial value.

When $\boldsymbol{R_A \sim \mathcal{O}(1)}$, the first two stages of hydrodynamic processes and magnetic production occur almost simultaneously. This is followed by the final stage where only harmonic exchange dominates and equipartition between perturbation kinetic and magnetic energies is seen. Due to a two-stage behavior and curtailed monotonic growth stage, the amplification of perturbations is significantly reduced compared to the $R_A \ll 1$ regime.

When $\boldsymbol{R_A \gg 1}$, the Alfvén processes dominate from the beginning. As a result, harmonic exchange dominates over all other processes and no amplification of perturbations is seen. Equipartition of kinetic and magnetic energies is prevalent from the beginning.

For **spanwise wavevectors**, the velocity and magnetic fields are decoupled. As a result, there

is no stabilization of shear instability due to magnetic field and kinetic energy grows algebraically.

7.2 Incompressible regime - Inhomogeneously sheared MHD mixing layers

For the case of mixing layers, the ratio of shear-to-Alfvén frequency varies along the normal direction, i.e., $R_A \equiv R_A(x_2)$. Since the value of shear is maximum at the center, $R_A(x_2 = 0)$ assumes the minimum value. At normal locations, $x_2 \geq (4-5)\delta_\omega$, the mean velocity is almost uniform and $R_A(x_2) \gg 1$. If different normal locations were to evolve independently (negligible transport), stabilization due to applied magnetic field is maximum at locations far from the center, where shear is maximum. However, as the location of maximum shear is also an inflection point leading to large scale Kelvin-Helmholtz instability and transport in inhomogeneous shear flows is not negligible, the dynamics of the perturbation/instability are decided by the value of $R_{A0} \equiv R_A(x_2 = 0)$. This also eliminates the possibility of similar analytical treatment as the previous study. Therefore, we utilize direct numerical simulation of mixing layers with streamwise magnetic field to characterize perturbation evolution at different R_{A0} regimes. Instability measures such as maximum circulation and perturbation amplification with respect to hydrodynamic case are utilized to demarcate the parameter space of R_{A0} into strong-, intermediate- and weak-field regimes. In each of the regimes, the pressure-vorticity dynamics are explicated and evolution of normal velocity and magnetic fields is investigated.

In the **hydrodynamic regime**, owing to vorticity production - $u_2' d^2U_1/dx_2^2$, the precursor vortices with positive and negative vorticity form around the pivot point, i.e., the stagnation point at the center of the streamwise-normal plane. Due to positive feedback from negative pressure, vortices with negative magnitude merge and rollup, entraining the surrounding fluid. The negative pressure and vorticity mutually intensify each other until nonlinear asymptotic stage sets in and secondary vortex bands form.

In the **weak field regime**, $R_{A0} \leq 0.02$, the behavior is similar to that seen in the hydrodynamic regime and similar merger and rollup of vortices is seen. However, the formation of secondary vortex bands is disrupted by the onset of 'resistive' instability. This results in reduced circulation,

suction pressure compared to the hydrodynamic case. However, unlike $R_A \ll 1$ regime in homogeneous shear, equipartition of perturbation kinetic and magnetic energies is not seen at late times.

In the **strong field regime**, $R_{A0} \geq 0.1$, implying that at most normal locations, $R_A(x_2) \gg 1$. As seen for the case of homogeneous shear this results in oscillatory evolution of normal velocity and magnetic field components leading to negligible kinetic, magnetic and vorticity production. As u_2' changes sign, the precursor vortices simply wind and unwind and do not intensify. The instability is eliminated and equipartition between perturbation kinetic and magnetic energies is seen. This behavior is similar to the one-stage evolution of perturbations seen for $R_A \gg 1$ for the case of homogeneous shear.

In the **intermediate field regime**, the precursor vortices form similar to the hydrodynamic regime but are of much reduced intensity. Due to uni-directional transfer from kinetic to magnetic energy at initial times, normal velocity component grows monotonically but with reduced intensity. As a result, suction at pivot point is not generated and precursor vortices rollup without merger. The instability is not fully manifest and the conditions for the onset of resistive instability are delayed.

7.3 Compressible regime - Inhomogeneously sheared MHD planar jets

Due to the inhomogeneity in shear in planar jets, $R_A \equiv R_A(x_2)$, similar to mixing layers. However, in the compressible regime, there is another parameter, $M_g(x_2) \equiv S(x_2)/\kappa a$, which accounts for the frequency of the pressure wave. M_g attains maximum values at the locations of maximum shear and as a consequence, pressure wave stabilization is maximum at the location of the instability, i.e., inflection point. In a compressible regime, the coupled velocity and magnetic field terms are different from those in the incompressible regime. The normal component of velocity perturbation is now coupled with both streamwise and normal components of magnetic field, in addition to pressure. As a consequence, harmonic exchange leading to equipartition cannot be anticipated between individual components of velocity and magnetic fields. Equations for perturbation energies now indicate equipartition between $\mathcal{K}_2$ and $\mathcal{B} + \mathcal{P}$, if transport and production are

negligible.

The evolution of single streamwise modes in the low Mach number regime indicate similar behavior as that seen in the case of incompressible mixing layers and $\mathcal{P}$ is negligible. As M is increased, $\mathcal{P}$ increases substantially attaining values close to that of $\mathcal{K}_2$ due to exchange via pressure-dilatation. The exponential growth of instability is not eliminated, only growth rate is substantially reduced. As M_A or $R_{A,min}$ is increased, the growth rate is further reduced. For supersonic cases with $R_{A,min} \sim \mathcal{O}(0.1)$, the exchanges of $\mathcal{K}_2$ with $\mathcal{P} + \mathcal{B}$ become harmonic leading to equipartition. For low Re_m, equipartition is seen at all times. As Re_m is increased, equipartition is seen at early times and $\mathcal{P} + \mathcal{B}$ grows due to magnetic stretching production.

For random, isotropic initial conditions, due to the presence of spanwise wavevectors not stabilized by compressibility and magnetic field, the fluctuations do not cease to grow even at high magnetic field strengths. But the overall instability is highly suppressed.

REFERENCES

ARAYA, D. B., EBERSOHN, F. H., ANDERSON, S. E. & GIRIMAJI, S. S. 2015 Magneto-gas kinetic method for nonideal magnetohydrodynamic flows: Verification protocol and plasma jet simulations. *Journal of Fluids Engineering* **137** (8), 081302–081302–11.

BARON, F. 1982 Macro-simulation tridimensionnelle d'ecoulements turbulents cisailles. PhD thesis, Universite Pierre at Marie Curie, Paris.

BATCHELOR, G. K. & PROUDMAN, I. 1954 The effect of rapid distortion of a fluid in turbulent motion. *Quarterly Journal of Mechanics and Applied Mathematics* **7** (1), 83–103.

BATY, H & KEPPENS, RONY 2002 Interplay between Kelvin-Helmholtz and current-driven instabilities in jets. *The Astrophysical Journal* **580** (2), 800.

BATY, H. & KEPPENS, R. 2006 Kelvin-Helmholtz disruptions in extended magnetized jet flows. *Astronomy and Astrophysics* **447** (1), 9–22.

BELLE-HAMER, A. L. LA, OTTO, A. & LEE, L. C. 1994 Magnetic reconnection in the presence of sheared plasma flow: Intermediate shock formation. *Physics of Plasmas* **1** (3), 706–713.

BERTSCH, REBECCA L, SUMAN, SAWAN & GIRIMAJI, SHARATH S 2012 Rapid distortion analysis of high Mach number homogeneous shear flows: Characterization of flow-thermodynamics interaction regimes. *Physics of Fluids* **24** (12), 125106.

BHATNAGAR, PRABHU LAL, GROSS, EUGENE P & KROOK, MAX 1954 A model for collision processes in gases. i. small amplitude processes in charged and neutral one-component systems. *Physical review* **94** (3), 511.

BLANDFORD, RD & PAYNE, DG 1982 Hydromagnetic flows from accretion discs and the production of radio jets. *Monthly Notices of the Royal Astronomical Society* **199** (4), 883–903.

BLUMEN, W., DRAZIN, P. G. & BILLINGS, D. F. 1975 Shear layer instability of an inviscid compressible fluid. part 2. *Journal of Fluid Mechanics* **75** (2), 305 – 316.

CAMBON, C., COLEMAN, G. N. & MANSOUR, N. N. 1993 Rapid distortion analysis and direct simulation of compressible homogeneous turbulence at finite Mach number. *Journal of Fluid Mechanics* **257**, 641–665.

CHAGELISHVILI, G. D., HRISTOV, T. S., CHANISHVILI, R. G. & LOMINADZE, J. G. 1993 Mechanism of energy transformations in shear magnetohydrodynamic flows. *Physical Review E* **47** (1), 366–374.

CHANDRASEKHAR, S. 1961 *Hydrodynamic and Hydromagnetic Instabilities*. Oxford University Press.

CHEN, FRANCIS F. 1994 *Introduction to Plasma Physics and Controlled Fusion: I. Plasma Physics*, 2nd edn. Plenum, New York: Springer Science+Business Media.

CORKE, THOMAS C, ENLOE, C LON & WILKINSON, STEPHEN P 2010 Dielectric barrier discharge plasma actuators for flow control. *Annual review of fluid mechanics* **42**, 505–529.

DAVIDSON, PETER ALAN 2002 An introduction to magnetohydrodynamics .

DIAZ, F. R. C. 2000 The VASIMR rocket. *Scientific American* **283** (5), 90–97.

DIMITROV, Z. D., MANEVA, Y. G., HRISTOV, T. S. & MISHONOV, T. M. 2011 Over-reflection of slow magnetosonic waves by homogeneous shear flow: Analytical solution. *Physics of Plasmas* **18** (8), 082110–1–3.

DOELEMAN, SHEPERD S, FISH, VINCENT L, SCHENCK, DAVID E, BEAUDOIN, CHRISTOPHER, BLUNDELL, RAY, BOWER, GEOFFREY C, BRODERICK, AVERY E, CHAMBERLIN, RICHARD, FREUND, ROBERT, FRIBERG, PER *et al.* 2012 Jet-launching structure resolved near the supermassive black hole in M87. *Science* **338** (6105), 355–358.

DRAZIN, P. G. & REID, W. H. 1981 *Hydrodynamic stability*. Cambridge university press.

FAGANELLO, M., CALIFANO, F. & PEGORARO, F. 2008 Time window for magnetic reconnection in plasma configurations with velocity shear. *Physical Review Letters* **101** (17), 175003–1–4.

FRANK, A., JONES, T. W., RYU, D. & GAALAAS, J. B. 1996 The MHD Kelvin-Helmholtz instability: A two-dimensional numerical study. *The Astrophysical Journal* **460**, 777 – 793.

FURTH, H. P., KILLEEN, J. & ROSENBLUTH, M. N. 1963 Finite-resistivity instabilities of a sheet pinch. *Physics of Fluids* **6** (4), 459–484.

GOLDSTON, R. J. & RUTHERFORD, P. H. 1995 *Introduction to plasma physics*. CRC Press.

GOOSSENS, MARCEL 2012 An introduction to plasma astrophysics and magnetohydrodynamics **294**.

GUTMARK, E & WYGNANSKI, I 1976 The planar turbulent jet. *Journal of Fluid Mechanics* **73** (3), 465–495.

HELMHOLTZ, PROFESSOR 1868 XLIII. On discontinuous movements of fluids. *The London, Edinburgh, and Dublin Philosophical Magazine and Journal of Science* **36** (244), 337–346.

HERAULT, J., RINCON, F., COSSU, C., LESUR, G., OGILVIE, G. I. & LONGARETTI, P. Y. 2011 Periodic magnetorotational dynamo action as a prototype of nonlinear magnetic-field generation in shear flows. *Physical Review E* **84** (3), 036321–1–9.

KARIMI, M. & GIRIMAJI, S. S. 2016 Suppression mechanism of Kelvin-Helmholtz instability in compressible fluid flows. *Physical Review E* **93** (4), 041102.

KARIMI, M. & GIRIMAJI, S. S. 2017 Influence of orientation on the evolution of small perturbations in compressible shear layers with inflection points. *Physical Review E* **95** (3), 033112.

KEPPENS, RONY & TÓTH, G 1999 Nonlinear dynamics of Kelvin–Helmholtz unstable magnetized jets: Three-dimensional effects. *Physics of Plasmas* **6** (5), 1461–1469.

KERIMO, JOHANNES & GIRIMAJI, SHARATH S 2007 Boltzmann–BGK approach to simulating weakly compressible 3D turbulence: Comparison between lattice Boltzmann and gas kinetic methods. *Journal of Turbulence* (8), N46.

KIRILLOV, O. N., STEFANI, F. & FUKUMOTO, Y. 2014 Local instabilities in magnetized rotational flows: A short-wavelength approach. *Journal of Fluid Mechanics* **760**, 591–633.

KOVASZNAY, L. S. G. 1953 Turbulence in supersonic flow. *Journal of the Aeronautical Sciences* **20** (10), 657–674.

KULSRUD, RUSSEL M. 2005 *Plasma Physics for Astrophysics*. Princeton, New Jersey 08540: Princeton University Press.

KUMAR, G., BERTSCH, REBECCA L. & GIRIMAJI, SHARATH S. 2014 Stabilizing action of pressure in homogeneous compressible shear flows: Effect of Mach number and perturbation obliqueness. *Journal of Fluid Mechanics* **760**, 540–566.

KUMAR, G, GIRIMAJI, SHARATH S & KERIMO, J 2013 WENO-enhanced gas-kinetic scheme for direct simulations of compressible transition and turbulence. *Journal of Computational Physics* **234**, 499–523.

LANDAHL, MT 1980 A note on an algebraic instability of inviscid parallel shear flows. *Journal of Fluid Mechanics* **98** (2), 243–251.

LAU, Y. Y. & LIU, L. S. 1980 Stability of shear flow in a magnetized plasma. *Physics of Fluids* **23** (5), 939–941.

LERNER, J. & KNOBLOCH, E. 1985 The stability of dissipative magnetohydrodynamic shear flow in a parallel magnetic field. *Geophysical & Astrophysical Fluid Dynamics* **33** (1-4), 295–314.

LIAO, WEI, PENG, YAN, LUO, LI-SHI & XU, KUN 2008 Modified gas-kinetic scheme for shock structures in argon. *Progress in Computational Fluid Dynamics, an International Journal* **8** (1-4), 97–108.

MAK, J., GRIFFITHS, S. D. & HUGHES, D. W. 2017 Vortex disruption by magnetohydrodynamic feedback. *Physical Review Fluids* **2** (11), 113701.

MALAGOLI, A., BODO, G. & ROSNER, R. 1996 On the nonlinear evolution of magnetohydrodynamic Kelvin-Helmholtz instabilities. *The Astrophysical Journal* **456**, 708.

MCWILLIAMS, JAMES C 2012 The elemental shear dynamo. *Journal of Fluid Mechanics* **699**, 414–452.

MICHALKE, A. 1964 On the inviscid instability of the hyperbolic tangent velocity profile. *Journal of Fluid Mechanics* **19** (4), 543–556.

MIKELLIDES, PAVLOS G, TURCHI, PETER J & RODERICK, NORMAN F 2000 Applied-field magnetoplasmadynamic thrusters, part 1: Numerical simulations using the MACH2 code. *Journal of Propulsion and Power* **16** (5), 887–893.

MIN, KYOUNGWOOK 1997 Simulation of the Kelvin-Helmholtz instability in the magnetized slab jet. *The Astrophysical Journal* **482** (2), 733.

NYKYRI, K. & OTTO, A. 2001 Plasma transport at the magnetospheric boundary due to reconnection in Kelvin-Helmholtz vortices. *Geophys. Res. Lett.* **28** (18), 3565–3568.

OBERGAULINGER, M, ALOY, MA & MÜLLER, E 2010 Local simulations of the magnetized Kelvin-Helmholtz instability in neutron-star mergers. *Astronomy & Astrophysics* **515**, A30.

OLSEN, CHRISTOPHER S, BALLENGER, MAXWELL G, CARTER, MARK D, DÍAZ, FRANKLIN R CHANG, GIAMBUSSO, MATTHEW, GLOVER, TIMOTHY W, ILIN, ANDREW V, SQUIRE, JARED P, LONGMIER, BENJAMIN W & CLOUTIER11, PAUL A 2013 An experimental study of plasma detachment from a magnetic nozzle in the plume of the vasimr® engine. In *Proceedings of the 33rd International Electric Propulsion Conference*.

ONG, R. S. B. & RODERICK, N. 1972 On the Kelvin-Helmholtz instability of the Earth's magnetopause. *Planetary Space Science* **20** (1), 1–10.

PALOTTI, M. L., HEITSCH, F., ZWEIBEL, E. G. & HUANG, Y.-M. 2008 Evolution of unmagnetized and magnetized shear layers. *The Astrophysical Journal* **678** (1), 234.

POPE, STEPHEN B. 2001 *Turbulent Flows*. Cambridge University Press.

PRATURI, D., COLLARD, D. & GIRIMAJI, S. S. in production The effect of magnetic field on perturbation evolution in homogeneously sheared flows. *Journal of Fluid Mechanics*.

PRENDERGAST, KEVIN H & XU, KUN 1993 Numerical hydrodynamics from gas-kinetic theory. *Journal of Computational Physics* **109** (1), 53–66.

PRICE, DANIEL J & ROSSWOG, STEPHAN 2006 Producing ultrastrong magnetic fields in neutron star mergers. *Science* **312** (5774), 719–722.

RAMAPRIAN, BR & CHANDRASEKHARA, MS 1985 LDA measurements in plane turbulent jets. *Journal of Fluids Engineering* **107** (2), 264–271.

RAYLEIGH, LORD 1879 On the stability, or instability, of certain fluid motions. *Proceedings of the London Mathematical Society* **1** (1), 57–72.

ROGALLO, ROBERT SUGDEN 1981 Numerical experiments in homogeneous turbulence. *NASA Technical Memorandum* **81315**.

ROTH, J, SHERMAN, DANIEL & WILKINSON, STEPHEN 1998 Boundary layer flow control with a one atmosphere uniform glow discharge surface plasma. In *36th AIAA Aerospace Sciences Meeting and Exhibit*, p. 328.

SANDHAM, N. D. & REYNOLDS, W. C. 1991 Three-dimensional simulations of large eddies in the compressible mixing layer. *Journal of Fluid Mechanics* **224**, 133–158.

SARKAR, S 1995 The stabilizing effect of compressibility in turbulent shear flow. *Journal of Fluid Mechanics* **282**, 163–186.

SARKAR, S., ERLEBACHER, G., HUSSAINI, M. Y. & KREISS, H. O. 1991 The analysis and modelling of dilatational terms in compressible turbulence. *Journal of Fluid Mechanics* **227**, 473–493.

SEN, AMIYA K 1964 Effect of compressibility on Kelvin-Helmholtz instability in a plasma. *The Physics of Fluids* **7** (8), 1293–1298.

SHATROV, V & GERBETH, G 2007 Magnetohydrodynamic drag reduction and its efficiency. *Physics of Fluids* **19** (3), 035109.

DA SILVA, CARLOS B & MÉTAIS, OLIVIER 2002 Vortex control of bifurcating jets: A numerical study. *Physics of Fluids* **14** (11), 3798–3819.

DA SILVA, CARLOS B & PEREIRA, JOSÉ CF 2008 Invariants of the velocity-gradient, rate-of-strain, and rate-of-rotation tensors across the turbulent/nonturbulent interface in jets. *Physics of Fluids* **20** (5), 055101.

SIMONE, A, COLEMAN, G & CAMBON, C 1997 The effect of compressibility on turbulent shear flow: A rapid distortion-theory and direct numerical-simulation study. *Journal of Fluid Mechanics* **330**, 307–338.

STANLEY, SA, SARKAR, S & MELLADO, JP 2002 A study of the flow-field evolution and mixing in a planar turbulent jet using direct numerical simulation. *Journal of Fluid Mechanics* **450**, 377–407.

TAYLOR, G. I. & BATCHELOR, G. K. 1949 The effect of wire gauze on small disturbances in a uniform stream. *Quarterly Journal of Mechanics and Applied Mathematics* **2** (1), 1–29.

THOMAS, FLINT O, KOZLOV, ALEXEY & CORKE, THOMAS C 2008 Plasma actuators for cylinder flow control and noise reduction. *AIAA journal* **46** (8), 1921–1931.

THOMSON, WILLIAM 1871 XLVI. hydrokinetic solutions and observations. *The London, Edinburgh, and Dublin Philosophical Magazine and Journal of Science* **42** (281), 362–377.

TREFETHEN, LLOYD N., TREFETHEN, ANNE E., REDDY, SATISH C. & DRISCOLL, TOBIN A. 1993 Hydrodynamic stability without eigenvalues. *Science* **261** (5121), 578–584.

XIE, ZHIMIN, KARIMI, MONA & GIRIMAJI, SHARATH S 2017 Small perturbation evolution in compressible Poiseuille flow: Pressure–velocity interactions and obliqueness effects. *Journal of Fluid Mechanics* **814**, 249–276.

XU, KUN 2001 A gas-kinetic BGK scheme for the Navier-Stokes equations and its connection with artificial dissipation and Godunov method. *Journal of Computational Physics* **171** (1), 289–335.

ZAQARASHVILI, TEIMURAZ V. 1997 On a possible generation mechanism of a solar cycle. *The Astrophysical Journal* **487** (2), 930–935.